# SENSOR-BASED NONLINEAR AND NONSTATIONARY DYNAIMC ANALYSIS OF ONLINE STRUCTURAL HEALTH MONITORING

By

MAHMOUD ZEIDAN MISTARIHI

Bachelor of Science in Mathematics
Mutah University
Al-karak, Jordan
1995

Master of Science in Mathematics
Mutah University
Al-karak, Jordan
2003

Submitted to the Faculty of the
Graduate College of the
Oklahoma State University
in partial fulfillment of
the requirements for
the Degree of
DOCTOR OF PHILOSOPHY
December, 2013

# SENSOR-BASED NONLINEAR AND NONSTATIONARY DYNAMIC ANALYSIS OF ONLINE STRUCTURAL HEALTH MONITORING

Dissertation Approved:

Dr. Zhenyu (James) Kong
Dissertation Adviser

Dr. Satish T. S. Bukkapatnam
Dissertation Co-Adviser

Dr. Tieming Liu

Dr. Tyler Ley
External member

# ACKNOWLEDGEMENTS

I would like to extend my sincerest gratitude to my academic adviser, Dr. Zhenyu (James) Kong, for his continuous encouragement, inspirations and financial support through my Ph.D. study. His guidance and professionalism will remain with me as I continue my academic career. Whatever I say! Really I could not repay him. Sincere thanks are also due to my dissertation co-adviser, Dr. Satish T. S. Bukkapatnam who introduced me to the study of nonlinear time series analysis. His help and technical advice are unforgettable. I am deeply indebted to my outside member on my dissertation committee, Dr. Tyler Ley, for teaching me strength of materials and for his thoughtful comments and valuable suggestions to improve this dissertation. I would also like to acknowledge my dissertation committee member, Dr. Tieming Liu for his help, inputs and suggestions.

Thanks go to my colleagues and friends for their great help and support throughout my Ph.D. study. Special mention goes to Omer Beyca and Kaveh Bastani.

Great thanks to my wife, Wafa, who highly supported me, stood by me and compelled me not to give up. I thank my sisters, brothers and my five kids for being an inspiration to me. Finally, I would like to express my warm thanks to my beloved parents who have always encouraged me to be who I am. I dedicate my dissertation to the loving memory of my (late) mother.

Name: MAHMOUD Z. MISTARIHI

Date of Degree: DECEMBER, 2013

Title of Study: **SENSOR-BASED NONLINEAR AND NONSTATIONARY DYNAMIC ANALYSIS OF ONLINE STRUCTURAL HEALTH MONITORING**

Major Field: INDUSTRIAL ENGINEERING AND MANAGEMENT

Abstract: This dissertation focuses on robust online Structural Health Monitoring (SHM) framework for civil engineering structures. The proposed framework improves the diagnostic and prognostic schemes for damage-state awareness and structural life prediction in civil engineering structures. The underlying research achieves three main objectives, namely, (1) sensor placement optimization using partial differential equation modeling and Fisher information matrix, (2) structural damage detection using quasi-recursive correlation dimension (QRCD), and (3) structural damage prediction using online empirical mode decomposition (EMD).

The research methodology includes three research tasks: Firstly, to formulate the optimal criteria for the sensor placement optimization damage detection problem based upon a partial differential equation (PDE) analytical model. The PDE model is derived and then validated through experimental results using correlation analysis. Secondly, to develop a novel quasi-recursive correlation dimension method for structural damage detection. The QRCD algorithm is integrated with an attractor analysis and overlapping windowing technique. Thirdly, to design an online structural damage prediction method based on empirical mode decomposition. The proposed SHM prediction scheme consists of two steps: prediction based change point detection using Hilbert instantaneous phase, and damage severity prediction using the energy index of the most representative intrinsic mode function (IMF).

Study results show that; (1) the proposed optimal sensor placement method leads to an optimal spatial location for a collection of sensors, which are sensitive to structural damage, (2) the proposed damage detection algorithm can significantly alleviate the complexity of computation for correlation dimension to approximate O(N), making the online monitoring of nonlinear/nonstationary processes more applicable and efficient; and (3) the proposed empirical mode decomposition method for online damage prediction overcomes the boundary effects of the sifting process, and it has significant prediction accuracy improvement (greater than 30%) over other commonly used prediction techniques.

# TABLE OF CONTENTS

Chapter Page

I. INTRODUCTION

I. INTRODUCTION ........................................ 1

1.1 Research motivations ........................................ 1
1.2 Research objectives ........................................ 2
1.3 Major contributions ........................................ 3
1.4 Organization of the dissertation ........................................ 4
References ........................................ 6

II. BACKGROUND AND LITERATURE REVIEW ........................................ 7

2.1 Structural health monitoring (SHM) overview ........................................ 7
    2.1.1 Types of damage ........................................ 8
    2.1.2 Levels of damage identification in structural health monitoring ........................................ 9
2.2 Damage detection techniques in structural health monitoring ........................................ 9
2.3 Signal processing methods in structural health monitoring ........................................ 11
    2.3.1 Fourier analysis ........................................ 11
    2.3.2 Wavelet analysis ........................................ 13
    2.3.3 Hilbert Huang transform ........................................ 14
    2.3.4 Standard G-P correlation dimension analysis ........................................ 16
2.4 Sensor placement in structural health monitoring ........................................ 18
    2.4.1 Sensing structural response ........................................ 18
    2.4.2 Summary of optimal sensor placement in SHM ........................................ 21
2.5 Research gap and challenges ........................................ 21
References ........................................ 23

III. RESEARCH METHODOLOGY ........................................ 29

3.1 Sensor placement optimization in structural health monitoring ........................................ 29
3.2 Damage detection for online structural health monitoring applications ........................................ 30

Chapter Page

3.3 Damage prediction for online structural health monitoring ..... 31
References ..... 33

IV. OPTIMAL SENSOR PLACEMENT FOR SHM UDER UNCERTAINTY ..... 34

4.1 Introduction and motivation ..... 34
4.2 Review of related research in sensor placement optimization ..... 35
    4.2.1 Sensor placement optimization methods ..... 35
    4.2.2 Sensor placement optimization criteria ..... 37
    4.2.3 Sensor placement optimization main research areas ..... 38
4.3 Dynamic response for multistory buildings using PDE modeling ..... 40
4.4 The differential equation modeling of the ASCE benchmark structure ..... 41
4.5 Validation of the proposed differential equation model ..... 50
4.6 A dynamical system formulation of the sensor placement problem ..... 52
4.7 Application to ASCE benchmark problem ..... 53
    4.7.1 Optimization of the sensor configuration ..... 54
    4.7.2 Optimization results and discussion ..... 54
    4.7.3 Capability of damage detection for the ASCE benchmark structure ..... 57
4.8 Summary ..... 58
References ..... 60

V. DAMAGE DETECTION BASED ON QUASI-RECURSIVE CORRELATION DIMENSION ANALYSIS ..... 67

5.1 Introduction and motivation ..... 67
5.2 Review of related research in correlation dimension ..... 69
    5.2.1 Related research in application of correlation dimension ..... 69
    5.2.2 Related research in algorithms for computing correlation dimension ..... 70
5.3 State space reconstruction for time series sensor signal ..... 72
5.4 Proposed quasi-recursive correlation dimension analysis ..... 74
5.5 Case studies ..... 82
    5.5.1 Computational accuracy of the correlation dimension ..... 83
    5.5.2 Detection of process changes simulated using ARMA models ..... 84
    5.5.3 Damage detection for the ASCE benchmark structure ..... 90
    5.5.4 Correlation dimension and stiffness of the benchmark structure ..... 93
5.6 Summary ..... 94
References ..... 96

Chapter Page

VI. DAMAGE PREDICTION USING EMPIRICAL MODE DECOMPOSITION BASED ANALYSIS..........104

6.1 Introduction and motivation..........104
6.2 Review of related research in Hilbert Huang transform..........105
    6.2.1 Related research in boundary processing techniques for EMD..........105
    6.2.2 Related research in interpolation for EMD..........108
6.3 Empirical mode decomposition..........110
6.4 Hilbert spectral analysis..........112
6.5 The proposed methodology for online damage prediction..........114
    6.5.1 Piecewise cubic Hermite interpolation..........114
    6.5.2 Online empirical mode decomposition..........115
    6.5.3 Selection of intrinsic mode functions..........120
    6.5.4 Prediction using visual recurrence analysis..........122
    6.5.5 Hilbert instantaneous phase for the predicted damage point detection.124
6.6 Case studies..........125
    6.6.1 The performance of the proposed boundary method..........126
    6.6.2 Detecting process changes using the proposed method..........132
    6.6.3 Structural damage prediction using Hilbert instantaneous phase..........137
6.7 Summary..........144
References..........145

VII. CONCLUSIONS AND FUTURE WORK..........152
7.1 Conclusions..........152
7.2 Future work..........153

APPENDICES..........154

# LIST OF TABLES

Table Page

Table 2.1 Main structure damage identification schemes...........................................10

Table 2.2 Limitations of EMD boundary processing techniques ................................15

Table 2.3 Limitations of EMD interpolation techniques ............................................16

Table 2.4 Limitations of correlation dimension algorithms.........................................18

Table 2.5 Summary of displacement sensors..............................................................19

Table 2.6 Summary of Acceleration sensors ...............................................................20

Table 2.7 Summary of strain sensors...........................................................................20

Table 2.8 Summary of optimal sensor placement main research areas for SHM........21

Table 4.1 Classification of research in optimal sensor placement in SHM.................35

Table 4.2 Properties of the benchmark structural members .......................................42

Table 4.3 Damage patterns of the ASCE benchmark structure ...................................43

Table 4.4 MAC values of the undamaged acceleration random field for experimental and initial PDE models ..........................................................................51

Table 4.5 Optimal sensor coordinates based on the Figure of Merit...........................56

Table 4.6 $ARL_1$ results for the sensor configuration of the benchmark structure using Hotelling $T^2$ control charts for all six different damage patterns .......................57

Table 4.7 Percent loss in stiffness associated to different damage patterns for the benchmark structure.....................................................................................................58

Table 5.1 Comparison of algorithms for computing the correlation dimension .........72

Table Page

Table 5.2 Computational results of quasi-recursive correlation dimension and standard correlation dimension algorithms for well-known test attractors..................83

Table 5.3 ARMA (2, 1) models with different parameters..........................................85

Table 5.4 Damage patterns of the ASCE benchmark structure (12 DOF shear building)........................................................................................................................92

Table 5.5 Comparison results between QRCD and Morlet wavelet based EWMA control charts for the data with low level noise (NSR of 5%) for all six different damage patterns ..........................................................................................................92

Table 5.6 Comparison results between QRCD and Morlet wavelet based EWMA control charts for the data with high level noise (NSR of 20%) for all six different damage patterns ..........................................................................................................92

Table 5.7 Comparison between the proposed relative change indicator and percent loss in stiffness of 12 degrees of freedom shear-building models ...............................94

Table 6.1 Comparison of main boundary processing techniques ..............................108

Table 6.2 Comparison of main EMD interpolation techniques ................................110

Table 6.3 Parameters for constructing the synthetic test signal................................126

Table 6.4 Mean absolute error of the synthetic test signal .......................................129

Table 6.5 Kurtosis of intrinsic mode functions.........................................................130

Table 6.6 The calculated normalized energy for each selected IMF of the synthetic signal..........................................................................................................130

Table 6.7 ARMA (2, 1) models with different parameters.......................................133

Table 6.8 Six damage patterns generated from the ASCE benchmark structure.......138

Table 6.9 The calculated normalized energy for each selected IMF .........................140

Table 6.10 Prediction comparison for the first windowed signal over twenty forecasting steps ahead ...........................................................................................141

Table 6.11 Comparison results between HHT and Morlet wavelet for the data with low level noise (NSR of 5%) for all six different damage patterns...................142

Table Page

Table 6.12 Comparison results between HHT and Morlet wavelet for the data with high level noise (NSR of 20%) for all six different damage patterns................143

Table 6.13 Comparison between the proposed relative energy damage index and percent loss in stiffness of 12 degree of freedom shear-building models..................143

# LIST OF FIGURES

Figure Page

Figure 3.1 Schematic of the research methodology....................................................30

Figure 4.1 The overall optimal sensor placement methodology.................................40

Figure 4.2 Simplified continuous model to estimate the horizontal dynamic response for multistory buildings..................................................................................40

Figure 4.3 Benchmark structure.....................................................................................42

Figure 4.4 Six damage patterns generated from the benchmark model.......................44

Figure 4.5 Illustration of displacements in the *x*, *y*, and *z* directions...........................48

Figure 4.6 The overall procedure of approximating the acceleration..........................49

Figure 4.7 Performance comparison of the FOM for different optimization algorithms ........................................................................................................53

Figure 4.8 Existing placement of sensors on the ASCE benchmark structure ............55

Figure 4.9 3D graphic random field for the fourth floor of the benchmark structure..55

Figure 4.10 Figure of Merit using simulated annealing algorithm ..............................56

Figure 4.11 Optimal sensor locations for the four floors of the benchmark structure .56

Figure 5.1 Reference trajectories of the Lorenz attractor. 3D trajectory (left) along with 1 D time series for the same signal (right)..........................................................73

Figure 5.2 The correlation sum as a function of measuring radius..............................75

Figure 5.3 Relationship between correlation dimension and embedding dimension ..76

Figure 5.4 The computational complexity of the proposed QRCD ............................77

Figure Page

Figure 5.5 Overlapping segmentation method.........................................................79

Figure 5.6 Logarithm of the correlation sum (log C(r,m)) versus logarithm of the measuring radios (log(r)) ...........................................................................81

Figure 5.7 Comparison of CPU time between the two versions of the correlation dimension for Lorenz Attractor ......................................................................84

Figure 5.8 Process model structure...............................................................85

Figure 5.9 $\text{ARL}_1$ comparisons of CD-EWMA, W-EWMA and S-EWMA for detecting mean shift of the process noise for the three models mentioned in Table 3: (a) data generated by model 1, (b) data generated by model 2, (c) data generated by model 3..............................................................................87

Figure 5.10 $\text{ARL}_1$ comparison of CD-CUSUM, W-CUSUM and S-CUSUM in detecting variance change of the process noise with $N(0,1)$ for the three models mentioned in Table 3: data generated by model 1, (b) data generated by model 2, (c) data generated by model 3.........................................................................88

Figure 5.11 $\text{ARL}_1$ comparison of CD-CUSUM, W-CUSUM and S-CUSUM in detecting variance change of the process noise with $N(0,1.5^2)$ for the three models mentioned in Table 3: (a) data generated by model 1, (b) data generated by model 2, (c) data generated by model 3...............................................................89

Figure 5.12 ARL1 comparisons of CD-CUSUM, W-CUSUM and S-CUSUM in detecting variance change of measurement errors for the three models mentioned in Table: (a) data generated by model 1, (b) data generated by model 2, (c) data generated by model 3..............................................................................90

Figure 5.13 Benchmark structure: steel-frame structure (left) along with diagram of the analytical model (right).........................................................................91

Figure 6.1 Example of Intrinsic mode function........................................................111

Figure 6.2 The EMD sifting process.........................................................................111

Figure 6.3 The overall damage prediction methodology..........................................113

Figure 6.4 (a) Cubic spline interpolation, (b) Hermite spline interpolation, (c) the new cubic spline after adding new extreme, (d) the new Hermite spline after adding new extreme ...........................................................................................115

Figure 6.5 Signal localization using overlapping windowing method ......................116

Figure Page

Figure 6.6 The synthetic test signal (up) along with its spectrum (down).................127

Figure 6.7 The synthetic signal, its IMFs, and their FFTs, respectively ...................127

Figure 6.8 Hilbert spectrums for each IMF of the synthetic signal ...........................128

Figure 6.9 Comparison of CPU time between different boundary distortion processing methods of EMD..........................................................................129

Figure 6.10 Hilbert spectrum for the second IMF using the combined extended-cosine window method ...............................................................................131

Figure 6.11 Hilbert spectrum for the second IMF using the proposed boundary processing method ..................................................................................131

Figure 6.12 The block diagram of the process structures .........................................132

Figure 6.13 $\mathrm{ARL}_1$ / $\tau$ comparison of HIPH-CPD, W-EWMA and S-EWMA for detecting mean shift of the process noise for the three models mentioned in Table 3. (a) Data generated by model 1. (b) Data generated by model 2. (c) Data generated by model 3 ..........................................................................134

Figure 6.14 $\mathrm{ARL}_1$ / $\tau$ comparison of HIPH-CPD, W-CUSUM and S-CUSUM in detecting variance change of the process noise with $N(0,1)$ for the three models mentioned in Table 3. (a) Data generated by model 1. (b) Data generated by model 2. (c) Data generated by model ......................................................136

Figure 6.15 $\mathrm{ARL}_1$ / $\tau$ comparison of HIPH-CPD, W-CUSUM and S-CUSUM in detecting variance change of measurement errors for the three models mentioned in Table 3. (a) Data generated by model 1. (b) Data generated by model 2. (c) Data generated by model 3 ..........................................................................136

Figure 6.16 Benchmark structure: (a) steel-frame structure and (b) Diagram of the analytical model...........................................................................................138

Figure 6.17 The selected IMFs of the simulated signal representing damage pattern number three .............................................................................. `139

Figure 6.18 Hilbert instantaneous phase for the fourth IMF including the predicted damage point..............................................................................................141

Figure 6.19 Zooming window of Hilbert instantaneous phase for the fourth intrinsic mode function ...........................................................................142

# CHAPTER I

# INTRODUCTION

In this chapter, the motivation for choosing this research topic is presented in section 1.1. Research objectives and the scope of the research are discussed in section 1.2. Major contributions of the proposed research are provided in section 1.3. Finally, in section 1.4 the organization of this dissertation is introduced.

## 1.1 Research motivations

Many aerospace, civil and mechanical engineering systems, which provide the means for modern society to function, undergo aging and may suffer from the associated potential of damage accumulation [1]. According to a survey in the Federal Highway Administration (FHWA) reports of 2007, *approximately 25% of the bridges in the U.S. are rated as deficient* [2]. *It is estimated that an investment of 7 billion dollars per year for the next two decades will be require to rebuild or replace the bridge infrastructure of the U.S.* [3].

Structural Health Monitoring (SHM) is defined as the process of implementing a damage detection strategy for aerospace, civil, and mechanical engineering infrastructure [1]. Thus, there is significant socioeconomic value for the diagnosis and prognosis of SHM. The importance of SHM stems from the great monetary and human loss that may be incurred in the event of a collapse, either directly or indirectly due to loss of access and rerouting [4]. Therefore, it is imperative to effectively monitor and predict the health conditions of civil infrastructures.

Components that are critical to the performance of the structure must be inspected and monitored periodically. Currently, the most common method of inspection is the labor intensive and costly visual evaluation of the condition of structures. Even for experienced inspectors, the visual detection of corrosion and crack development inside structural elements is challenging, and it is near impossible to realize the resulting changes in deflections of the structure due to local changes in stiffness. Model-based methods are another technique of damage detection which also has some drawbacks [4] such as being insensitive to very small local damage [5]. It is also influenced by operational and environmental noise [6]. A third technique, traditional data analysis methods for nonstationary and nonlinear process gives less comprehensive analysis of structural health [7]. As a result of these limitations, a nonlinear and nonstationary dynamic analysis of online SHM is necessary to provide comprehensive understanding of structural integrity which is presented in this dissertation.

The proposed methodology depends on optimum sensor placement coupled with accurate estimation and prediction analysis. It offers a framework to develop an efficient SHM scheme which is expected to extend the useful life of structures by providing advanced forecast of failures and allows for preventive maintenance and more effective repair.

## 1.2 Research objectives

A successful SHM depends primly on optimum sensor placement as well as accurate analysis for sensor signal. According to Worden et al. [7], intelligent signal processing along with optimal sensor placement is the key element for effective SHM. In fact, an efficient signal processing technique of the sensor signal leads to an accurate interpretation of the structural integrity. The primary objective of this research is to develop an integrated nonlinear and nonstationary dynamic methodology for online SHM to effectively monitor and predict the health condition of civil infrastructures to avoid catastrophic incidents. The main research goal can be summarized as to improve the effectiveness and efficiency of the online SHM procedures in order to detect damage with high accuracy and reliability before it becomes critical. The specific objectives in this research are summarized as follows:

1) **Research objective 1 (Sensor placement optimization):** Develop an optimal sensor placement (OSP) approach under uncertainty for SHM systems to determine the spatial location and number for a collection of sensors, by which the sensitivity of sensors is maximized.
2) **Research objective 2 (Damage detection):** Integrate attractor analysis and dynamical nonlinear invariant measures to identify incipient damage and continuously trace its development for online SHM applications.
3) **Research objective 3 (Damage prediction):** Develop an online prediction model for structural health assessment based on an integrated advanced empirical mode decomposition (EMD) method with visual recurrence analysis (VRA).

## 1.3 Major contributions

This research work contributes to the development of estimation and prediction modeling based on optimal sensor placement under uncertainty in the area of SHM. The main contributions of the proposed methodology are summarized as follows:

1) A sensor placement technique to optimally determining the number and location of sensors based on partial differential equation modeling of the underlying structure was developed. The proposed optimal sensor placement method leads to improved estimates of the quantity and location of damage as well as successfully determines the spatial location for a collection of sensors.
2) A novel quasi-recursive correlation dimension algorithm (QRCD) for online detection of structural damages is created. The algorithm can significantly alleviate the complexity of computation for correlation dimension to approximate O(N), making the online monitoring of nonlinear/nonstationary processes using correlation dimension much more applicable and efficient.

3) An effective online prediction method for analyzing the nonlinear and nonstationary signals based on local empirical mode decomposition was derived. The proposed empirical mode decomposition method for online damage prediction overcomes the boundary effects, making the online monitoring and prediction of the underlying process much more accurate. Also, it has significant prediction accuracy improvement (greater than 30%) over other commonly used prediction techniques.

## 1.4 Organization of the dissertation

The rest of the dissertation is organized as follows:

**Chapter II: Background and literature review:** An overview of the SHM is described, followed by damage detection techniques, signal processing methods and sensor placement optimization. Finally, research gaps and technical challenges in SHM are identified.

**Chapter III: Research methodology:** The overall research methodology proposed in this research study is outlined in this chapter. It consists of three related components: the optimal sensor placement based on partial differential equation modeling, correlation dimension analysis for damage detection, and online empirical mode decomposition and visual recurrence analysis for damage prediction.

**Chapter IV: Optimal sensor placement for SHM under uncertainty:** A sensor placement optimization (SPO) approach under uncertainty for damage detection in structures is developed. This method is validated for the American Society of Civil Engineering (ASCE) benchmark structure.

**Chapter V: Damage detection based on quasi-recursive correlation dimension:** A novel quasi-recursive correlation dimension algorithm (QRCD) for online detection of structural damages is established. In addition, a quantitative damage index based on the relative change of the correlation dimension of the underlying process is developed. Mathematical and implementation details, validation, results, and conclusions are provided.

**Chapter VI: Damage prediction using empirical mode decomposition based analysis:** An effective online prediction scheme for analyzing the nonlinear and nonstationary signals based on local empirical mode decomposition is developed in this chapter. The Hilbert instantaneous phase is used as monitoring statistics for change point detection. The energy of the predicted Intrinsic Mode functions is then used for the prediction of damage quantification. The validation of this proposed method is provided.

**Chapter VI: Conclusions and future work:** This chapter presents a summary of the significant results and conclusions as well as recommendations for future work.

# REFERENCES

1. Sohn, H., et al., *Structural health monitoring using statistical pattern recognition techniques.* Journal of dynamic systems, measurement, and control, 2001. 123: p. 706.
2. AASHTO, *Bridge design specifications*, in *american association of state highway and transportation officials*. 2007: Washington, DC.
3. Jiang, J.C., *The application of correlation dimension in gearbox condition monitoring.* Journal of Sound and Vibration, 1999. 23: p. 529–542.
4. Montalvao, D., N. Maia, and A. Ribeiro, *A review of vibration-based structural health monitoring with special emphasis on composite materials.* Shock and Vibration Digest, 2006. 38(4): p. 295-326.
5. Kim, J.T., et al., *Damage identification in beam-type structures: frequency-based method vs mode-shape-based method.* Engineering structures, 2003. 25(1): p. 57-67.
6. Farrar, C.R. and D.A. Jauregui, *Comparative study of damage identification algorithms applied to a bridge: I. Experiment.* Smart Materials and Structures, 1998. 7: p. 704.
7. Worden, K.S., WJ, Tomlinson, GR. *Smart systems- The role of signal processing*. in *Proceedings of CEAS, International Forum on Aeroelasticity and Structural Dynamics*. 1997. Rome, Italy.

# CHAPTER II

# BACKGROUND AND LITERATURE REVIEW

This chapter provides an overview of the background of Structural Health Monitoring (SHM). It is followed by a review of related research in the SHM domain. In section 2.2, damage detection techniques in SHM are introduced, followed by review of signal processing methods in SHM in section 2.3. Sensing structural response and sensor placement optimization for SHM applications are summarized in section 2.4. Finally, in section 2.5, research gap and technical challenges in SHM are identified. More detailed literature review of each research objective will be presented in the subsequent chapters.

## 2.1 Structural Health Monitoring overview

This section describes the commonly used terms in SHM. It also presents types of damage as well as levels of damage identification in SHM. The definitions of the commonly used terms in SHM are summarized below [1].

1) Structural health monitoring: The process of implementing a damage detection strategy for aerospace, civil, and mechanical engineering infrastructure.
2) Damage identification: The process of detecting, localizing and characterizing damage in structural and mechanical systems.

3) Damage detection: The process of identifying damage in structural materials and systems.
4) Damage prognosis: The process of predicting the future probable capability of a structural material or system in an online manner, taking into account the effects of damage accumulation.
5) Sensor placement optimization: The process of determining the minimum spatial locations for a collection of sensors, in which the accuracy in parameter identification is maximized [2].

### 2.1.1 Types of damage

According to Sohn et al. [3], damage can be defined as changes introduced into the material and/or geometric properties of structural and mechanical systems, which adversely affect the performance of these systems. Under appropriate loading scenarios, damage begins at the material level then progresses to system's components at various rates. Moreover, damage can accumulate incrementally over long periods of time and can also result from scheduled discrete events (such as aircraft landings) as well as unscheduled discrete events (such as an earthquake) [3].

Damage in a structure can be classified into two types: linear and nonlinear damage. Linear damage is a situation when the initial linear–elastic structure remains the same after damage [3]. In this case, after introducing damage (usually sudden damage of lower intensity), the model parameters change but the structure still exhibits linear motion. Under the linear damage type, equations of motion are derived based on a linear structural properties assumption. Nonlinear damage occurs when the initially linear-elastic structure exhibits nonlinear behavior after damage incurred. An example of nonlinear damage is a fatigue crack which opens and closes during every cycle [1].

### 2.1.2 Levels of damage identification in SHM

The SHM process involves monitoring a system over time using sensors embedded or mounted externally to the system, and the extraction of damage-sensitive features from the sensor measurements as well as the analysis of these extracted features to identify the current state of the system's heath [4]. The purpose of implementing SHM schemes is to periodically update information regarding the capability of the structure to perform its intended function under aging and degradation [3]. Moreover, in the short term, SHM aims to provide reliable information regarding the integrity of the structure for rapid condition screening, especially after an earthquake or blast loading [3]. According to Rytter [5], SHM consists of four levels of damage identification as follows:

Level 1: Determining the existence of damage in the structure.

Level 2: Determination of the geometric location of the damage in the structure.

Level 3: Quantifying the severity of the damage.

Level 4: Predicting the remaining useful life of the structure.

The above levels of damage identification describe the damage state of the structure. Moreover, the effectiveness of global damage identification techniques can be evaluated by increasing knowledge of the damage state. Structural-dynamics techniques can be used for level one and level two of damage identification in either supervised or unsupervised learning mode. On the other hand, analytical models are usually used for level three and level four in a supervised learning mode [3].

## 2.2 Damage detection techniques in SHM

Components that are critical to the performance of the civil structure must be inspected or monitored periodically. Currently, the most common method of inspection is the labor intensive and costly visual evaluation of the condition of the structure. Inspectors periodically visit each structure to assess its condition, relying heavily on their own individual experience. Even for experienced inspectors, the visual detection of corrosion and crack development inside structural elements is challenging, and it is nearly impossible to realize the resulting changes in deflections of the structure due to local changes in stiffness [6]. Due to the fact that the existence of damage changes the physical parameters (mass, stiffness and damping) of the structure, model-based methods which depend on the model parameters (natural frequency, mode shape and modal damping), are widely used for damage detection [7]. For large structures such as bridges, damage may cause very small changes in natural frequency which may go undetected [8]. According to Ref. [9], changes in the mode shapes of any structure can replace the natural frequency as a more sensitive model parameter of local damage. However, extracted mode shapes are influenced by operational and environmental noise. One more drawback of using mode shapes with sensor real data is that the accuracy of the damage detection technique will be affected by the total number of sensors and the choice of sensor coordinates [7].

**Table 2.1** Main structure damage identification schemes

| **Detection scheme** | **Limitations** |
|---|---|
| Visual detection<br>(Balageas et al., 2010) | • Costly and labor intensive.<br>• Not feasible for very complicated bridge structures.<br>• The damage is usually not clear cut. |
| Non-destructive evaluation techniques<br>(Nichols, 2002) | • Requires that the location of the damage be known a priori. |
| Vibration-based approach<br>(Montalvao et al., 2006)<br>(Kim et al., 2003) | • *Natural frequency*: Not sensitive enough for large structures like bridges.<br>• *Mode shape*:<br>- Influenced by operational and environmental noise.<br>- Accuracy is affected by the total number of sensors and the choice of sensor coordinates<br>• *Model curvature*: less reliable when used for damage detection in structures with multiple sites of damage. |

Pandey [10] suggests using model curvature which is the second spatial derivative of the mode shape as a feature extraction for damage detection. However, mode shape curvatures are less reliable when used as damage detection in structures with multiple sites of damage [11].

Moreover, the traditional data analysis methods for nonstationary and nonlinearity give less accurate and less comprehensive results [12]. Table 2.1 shows some limitations of the main structure damage detection schemes.

## 2.3 Signal processing methods in SHM

A successful SHM scheme depends mainly on sensor technology as well as the associated signal analysis. According to Worden et al. [13], intelligent signal processing is the key element for effective SHM. In fact, an efficient signal processing technique of the sensor signal leads to an accurate interpretation of the structural integrity. Signal processing consists of extracting important features from sensor measurements with the aim of accurately identifying damage. Various signal processing methods for damage detection have been described in the literature. Some representative ones are reviewed in this dissertation. In particular, spectral analysis [14, 15] such as Fourier analysis, presented in section 2.3.1, Wavelet transforms [16-19], presented in section 2.3.2; and the Hilbert Huang transform [13, 20-22] discussed in section 2.3.3. Each one of these techniques utilizes a different method of processing the sensor signal. Also, all these methods have advantages over one another regarding applicability for analyzing specific data types.

### 2.3.1 Fourier analysis

The history of time-frequency analysis started with the introduction of Fourier transform in 1807, defined as:

$$X(w) = \int_{-\infty}^{+\infty} x(t)\, e^{2\pi i w t} dt \tag{2.1}$$

Fourier spectral analysis gives a good indicator about the energy content of the analyzed signal [23]. Moreover, due to its capability to identify the frequency content and intensity of the frequency component of the sensor signal, many SHM vibration-based approaches such as natural frequency, mode shapes and damping can be extracted from the Fourier transform of the underlying structural response [24]. Additionally, Fourier transform has many useful applications. According to Melhem et al. [25], the progression of impact damage in a beam can be detected using the Fourier transform. Nag et al. [26] developed a spectral finite element model based on the fast Fourier transform in order to simulate a composite beam with a delamination.

Fourier transform represents the signal in frequency domain, allowing useful information regarding the frequency content in the signal to be extracted. But Fourier transform is not suitable for the analysis of the nonstationary signal due to the fact that, by definition, the Fourier transform of a signal integrates the product of the signal with a harmonic of infinite length. Thus, the time information of the frequency change within the analyzed signal may be lost or become implicit.

To overcome the limitation in Fourier analysis dealing with nonstationary signals, a Short Time Fourier Transform (STFT) was developed, which is also called the windowed Fourier transform. In order to retain the time information in the signal, a sinusoidal window of fixed width is used to analyze the signal. The STFT is defined as

$$X(w,\tau) = \int x(t) * f(t-\tau)\, e^{2\pi iwt} dt \tag{2.2}$$

where $f(t-\tau)$ represents the window function.

Equation (2.2) incorporates both time and frequency localization characteristics, which is of great importance in signal processing [27]. The STFT is very useful in many applications such as damage detection using individual mode [28] and the location of flaws in aluminum plate specimens [29].

Even though the STFT employs a time-frequency representation, it suffers from time-frequency resolution. That is, the time-frequency resolution remains fixed over the whole time-frequency plane and having good time resolution along with good frequency resolution is challenging to achieve. The need to accurately analyze nonstationary data and the poor time-frequency resolution of the STFT moved researchers to develop a new method called Wavelet Analysis, which will be discussed in the following section.

### 2.3.2 Wavelet analysis

In 1982, Jean Morlet, a French geophysical engineer, introduced the idea of wavelet as a family of functions constructed from translations and dilatations of a single function called the “mother wavelet”. This new signal processing technique has been further developed to be an effective method in the SHM domain.

*Continuous wavelet transform*

The continuous wavelet transform of a signal *X(t)* is $W_x(a, b)$, which is defined as,

$$W_x(a,b) = \frac{1}{\sqrt{a}} \int_{-\infty}^{+\infty} x(t) * \overline{\psi} \left(\frac{t-b}{a}\right) dt \tag{2.3}$$

Here, $\overline{\psi}$ is the conjugate of the mother wavelet function $\psi$, *a* is termed the dilation parameter (also called scaling parameter) and *b* is termed the translation parameter (also termed shifting parameter). Worthy of mention is that both parameters are real and the dilation parameter must be positive.

The importance of the continuous wavelet transform comes from the fact that it maps the underlying sensor signal on a time scale plane, that is, by varying the value of the dilation parameter *a*, the data portion in the neighborhood of the shifting parameter can be examined in different resolution so that the time varying frequency content of the signal can be clearly revealed. More information about the continuous wavelet transform can be found in Refs. [30-32].

*Discrete wavelet transform*

A signal *X(t)* is decomposed using the discrete wavelet transform as follows:

$$X(t) = \sum_{i=1}^{i=j} D_i(t) + A_j(t) \tag{2.4}$$

where $D_i(t)$ represents the wavelet detail and $A_j(t)$ denotes the wavelet approximation at the *jth* level. The discrete wavelet transform reduces the computational cost of performing the continuous wavelet transform. In fact, it functions as a dyadic filter, in which the frequency band of the filter depends on the level of decomposition and the local examination of the signal becomes possible by shifting the frequency band in the time domain.

Wavelet analysis has been extensively used in SHM. According to Paget et al. [16], the amplitude change of the wavelet coefficients is successfully used to characterize the interactions of the Lamb waves with damage in a plate. Salehian et al. [4] used the arrival times of the reflected waves from the wavelet coefficients plots to infer the distance of the delamination from the sensor in an isotropic aluminum plate. Moreover, wavelet analysis is used to determine the wave speed that is affected by corrosion in the material [33]. More applications of the wavelet transform for SHM can be found in Refs. [34, 35]. Due to the preselected mother wavelet, in which the signal is correlated with different dilated and scaled versions, the wavelet analysis is suitable for analyzing a piecewise linear data. Thus an adaptive data analysis technique is needed.

### 2.3.3 Hilbert Huang Transform (HHT)

According to Refs. [20, 36], the Hilbert transform of a real valued function *x(t)* is defined as follows:

$$y(t) = \frac{P}{\pi}\int_{-\infty}^{+\infty}\frac{x(\tau)}{t-\tau}\,d\tau \tag{2.5}$$

where P is the Cauchy principle value.

From Equation (2.5), properties of the signal x(t) can be locally emphasized using convolution of x(t) with 1/t. Moreover, the function x(t) and its Hilbert transform y(t) form an analytic signal Z(t) given by,

$$z(t) = x(t) + iy(t) = a(t)e^{i\theta(t)} \tag{2.6}$$

where $a(t) = [x^2(t) + y^2(t)]^{1/2}$ represents the instantaneous amplitude of *x(t)*, and

$\theta(t) = arctan\left(\frac{y(t)}{x(t)}\right)$ refers to the instantaneous phase of *x(t)*.

If the signal *x(t)* is monocomponent, then the time derivative of the instantaneous phase $\theta(t)$ will be the instantaneous frequency *w(t)* given by,

$$w(t) = \frac{d\theta(t)}{dt} \tag{2.7}$$

In order to compute the instantaneous frequencies and amplitudes, the Hilbert transform *H(t)* is applied to each of the IMFs, which can be expressed as,

$$H(t) = \sum_{j=1}^{n} a_j\,(t) e^{i\int w_j(t)dt} \tag{2.8}$$

where $a_j(t)$ is the instantaneous amplitude associated with *j*th IMF.

**Table 2.2** Limitations of EMD boundary processing techniques

| **Boundary Processing Technique** | **Limitations** |
|---|---|
| Cosine window<br>(Deng et al., 2001) | • Not suitable for short data sets.<br>• Suitable for only a particular frequency band depending on the size of the Cosine window. |
| Mirrorisation<br>(Rilling et al., 2003) | • Does not fully overcome the sharp discontinuities, which highly corrupts the calculation of the next IMF.<br>• Does not guarantee the lining up of envelopes for subsequent blocks. |
| Characteristic wave extension<br>(Wang et al., 2010) | • The signal has to be periodic.<br>• Based on the weak assumption that the data outside of the data span must be evenly symmetrical or oddly symmetrical to those inside. |
| Neural network extension<br>(Lee et al., 2010) | • Choosing the appropriate neural network varies with different data sets.<br>• The amount of work per sliding window is increased, resulting in a performance penalty. |

The HHT has been recognized as one of the most important adaptive data analysis techniques [37]. It can be used for damage detection and system identification [5, 38, 39]. In particular, Tua et al. [40], used the energy peaks in the Hilbert spectrum associated to crack-reflected waves to determine accurate flight times as well as to estimate the orientation of the crack. Additionally, Yang et al. [13] demonstrates that the empirical mode decomposition (EMD) can be used to extract damage spikes caused by a sudden change. However, the EMD based on the entire signal record can have undesirable consequences such as the expensive calculation of the IMFs using cubic spline interpolation and the "end effects". This will cause the decomposed signal to be distorted leading to an inaccurate damage prediction scheme. Tables 2.2 and 2.3 summarize some limitations of the EMD with respect to boundary processing techniques and interpolation methods, respectively.

**Table 2.3** Limitations of EMD interpolation techniques

| **EMD interpolation technique** | **Limitations** |
|---|---|
| Linear piecewise interpolation<br>(De Boor, 1978) | • The envelope mean of the upper and lower envelopes can be too sharp and therefore the envelope mean loses its smoothness. |
| Cubic spline interpolation<br>(Fritsch et al.,1980) | • The obtained interpolating curve is continuously changed after having new extrema.<br>• It uses global information to calculate the derivative of envelopes.<br>• May create extra extrema by itself, leading to difficulty in achieving convergence of EMD. |
| A B-spline interpolation<br>(Riemenschneider et al., 2005) | • Does not highly reduce the end effects.<br>• As the scale of the IMF mode gets larger, the influence of the end effects becomes larger.<br>• It propagates into the low-frequency data components. |

As reported in Tables 2.2 and 2.3, the performance of the standard EMD technique may be affected by the end effects, especially when the scale of the IMFs gets larger.

### 2.3.4 Standard G-P correlation dimension analysis

According to Grassberger [41], the correlation dimension (referred to as $D_2$) is one of the fractal dimensions associated with the properties of a dynamic system [42, 43]. It is derived from the correlation sum, which is "a cumulative correlation function that measures the fraction of points in the *m*- dimensional reconstructed space" [44] and is defined as,

$$C(r,m) = \lim_{N_m \to \infty} \frac{2}{N_m(N_m-1)} \sum_{i,j=1,j>i}^{N_m} I(r - \|x(i,m) - x(j,m)\|) \tag{2.9}$$

where $I$ is the Heaviside step function, such that $I(x) = 0 \; if \; x \leq 0 \; and \; I(x) = 1 \; for \; x > 0$, $\|\ldots\|$ indicates the Euclidean-norm of the vector; $N_m = N - (m-1)\tau$ is the number of the reconstructed vectors and $r$ is the correlation length referred to as the radius of the measuring device [41]. The correlation sum increases monotonically from zero ($r$=0) to one ($r$ = the diameter of the attractor).

The summation in Equation (2.9) counts the number of pairs $\left(x(i,m), x(j,m)\right)$ whose distance $\|x(i,m) - x(j,m)\|$ is less than radius $r$. That is, the correlation sum can be defined as the cumulative distribution function (CDF) of the distances between a pair of points drawn independently according to a probability measure [45]. Equation (2.9) defines the correlation sum for a time series with infinite length. In practice, a time series with a limited length provides an estimation of the correlation sum [44].

Assuming that the limit of the correlation sum in Equation (2.9) exists; $m$ and $N_m$ are sufficiently large; and the values of the measuring radii $(r)$ at uniform or logarithmic intervals are sufficiently small, the correlation dimension can be defined as,

$$D_2 = \frac{\partial \log(C(r,m))}{\partial \log(r)} = \lim_{r \to 0} (\log C(r,m) \, / \log r) \tag{2.10}$$

where, $D_2$ is the correlation dimension, $C(r,m)$ is the correlation sum, they are related by means of the power law to satisfy the asymptotic relation,

$$C(r,m) \approx r^{D_2(m)} \; as \; r \to 0 \tag{2.11}$$

As the embedding dimension increases, the estimated correlation dimension also increases until it reaches a plateau. The plateaued dimension value gives an estimate of the actual correlation dimension of the underlying chaotic attractor.

Correlation dimension has the promising properties to characterize system dynamics. However, the existing algorithms for computing the correlation dimension have fairly high complexity and thus are not suitable for online monitoring. Table 2.4 shows some limitations of the existing correlation dimension algorithms.

**Table 2.4** Limitations of correlation dimension algorithms

| Algorithm | Computational complexity | Accuracy and handling noise |
|---|---|---|
| **G-P**<br>**(**Grassberger et al.,1983**)** | $O(N^2 . m_{max} . n_{ri})$ | • Accurate with huge sample size<br>• Applicable to a very low Gaussian noise NSR = 2 % |
| **The box-assisted correlation**<br>**(**Theiler, 1987**)** | $O(N . \log N . m_{max} . n_{ri})$ | • Low accuracy (high statistical error)<br>• Not suitable for embedding dimension greater than $0.75 \ln N$ |
| **Theiler**<br>**(**Theiler, 1990**)** | $O(N^2 . m_{max} . C(r_i))$ | • Large error for noisy signals |
| **GKA**<br>**(**Yu et al., 2000**)** | $O\left((N^2 + {n_{ri}}^2) . m_{max}\right)$ | • Applicable to different types of noise up to NSR = 20%<br>• Not suitable for long time series; $N > 10^5$ |

### 2.4 Sensor placement optimization in SHM

Sensor placement aims at determining the minimum spatial locations for a collection of sensors, in which the accuracy in parameter identification is maximized [2]. Research on sensing structural response is reviewed in section 2.4.1. Main methods and evaluation criteria as well as main research areas and applications for sensor placement optimization in SHM are introduced in section 2.4.2 and summarized in Table 2.8.

### 2.4.1 Sensing structural response

A sensor is a device that converts a physical phenomenon into an electrical signal [46]. Sensors are most commonly used to make quantifiable measurements and are available to measure many different quantities such as acceleration, strain, displacement, temperature and humidity. Choosing the right sensor requires considering what we want to measure and the environment of the sensor. The whole measurement system should be calibrated and traceable to the national standards organization [47].

In many cases, sensors are designed to meet a particular performance specification. According to Mukhopadhyay et al. [48], sensors for structural health monitoring have three performance characteristics: 1) they should be able to measure without causing any harm or damage of the structure; 2) they should also be robust to poor-signal-noise ratio compared to the level of structural damage they are trying to detect, and 3) they must be highly reliable and able to function for a long period of time, potentially over years.

**Table 2.5** Summary of displacement sensors [52]

| Sensor type | Advantages | Disadvantages | Applications |
|---|---|---|---|
| Magnetic | • More stable in noisy environments<br>• Capable of achieving low temperature sensitivity | • Susceptible to external magnetic inferences<br>• Used only for ferromagnetic materials | • Monitoring crankshaft for misfire<br>• Monitoring weld health in welded steel armor plates |
| Optical | • Insensitivity to stray magnetic field<br>• No loading effects on the structure | • Not suitable to be bent at steep angles<br>• Easily can be damaged | • Monitoring hull deflection of a composite patrol boat<br>• Measure composite bridge decks |
| Ultrasonic | • Resistant to ambient noise<br>• Capable to detect small defects at large distances | • Has a “dead” region where damage cannot be detected<br>• Time consuming | • Study of wear, chipping temperature in tooling parts<br>• Examining bolts or rivets in aircraft wings |
| Acoustic emission | • Less sensitive to material surface roughness for geometry<br>• Sensitive for crack formation detection | • Susceptible noise<br>• Possible mass loading issues | • Monitor seal and blade-tip rubbing in turbo machinery<br>• Damage assessment in steel-concrete composite bridge deck |

Common sensor technologies include piezoelectric, piezo-resistive and force-balance principles [49]. Other technologies include the use of magneto-restrictive actuators or the combination of ultrasonic excitation with piezo detectors [49]. At the level of sensor interfaces, a key revolution in sensors is the use of standard IEEE P1451.x interfaces [50]. In fact, Fiber optic sensors emerged as an important technology for structural integrity [51]. Using the strain as well as the fiber length, distribution information about the mechanical state of the structure is provided [51].

The premise of vibration-based SHM is that perturbations in a structural system cause changes in measured vibration signals. Therefore, kinematic quantities usually measured in vibration testing include accelerations, strain and displacement [48]. In Tables 2.5-2.7, different types of displacement, acceleration and strain are summarized [52].

**Table 2.6** Summary of acceleration sensors [52]

| Sensor type | Advantages | Disadvantages | Applications |
|---|---|---|---|
| Capacitive | • More sensitivities than Piezoresistive accelerometer<br>• Capable of measuring static acceleration | • Needs to compensate for drift and interference affects<br>• Low resolution and fragile | • Measure aircraft wing flutter response<br>• Measure hard disk drive acceleration due to writing process |
| MEMS | • Small, lightweight with high acceleration<br>• Lower cost than other accelerometers | • Degradation of the performance over time<br>• Expensive to repair | • Used for automotive airbag development measurements<br>• Monitor laptop computer vibration and stop hard drive processes to prevent damage |
| Piezoelectric | • Wide dynamic range with low output noise<br>• Capable of producing high output voltage | • Low bandwidth<br>• Sensor to be mounted to structure causing possible mass loading affects | • Used to measure vibration response in an exhaust system<br>• Measure acceleration response of TPS panel impact |
| Piezoresistive | • Not highly affected by electromagnetic fields<br>• Measures static acceleration | • Limited resolution due to resistive noise<br>• Mainly for low to mid frequency applications | • Measure acceleration of ejection seats<br>• Measure crash test dummy acceleration due to collisions |

**Table 2.7** Summary of strain sensors [52]

| Sensor type | Advantages | Disadvantages | Applications |
|---|---|---|---|
| Piezoresistive | • Capable of recognizing static forces<br>• Simplicity of mounting to the surface | • Sensor to be mounted to structure<br>• Susceptible to external sources of noise and temperature | • Measure strains in gas turbine fan blades<br>• Measure helicopter blade deflections |
| Optical | • Not susceptible to electromagnetic interferences<br>• Multiplexing capability | • Require fiber optic cable to be run to each sensor<br>• Needs a power source | • Strain monitoring of bridges, dams and buildings<br>• Monitoring ship hul strains |

### 2.4.2 Summary of optimal sensor placement in SHM

Most of the methods summarized in Table 2.8 use a deterministic way with unspecified types and sources of uncertainty [53]. In addition, a predefined number of discrete sensor configurations are required, in which the global optima is not guaranteed [54]. Moreover, in order to satisfy operational and geometrical constraints, there is a need to combine constraint satisfaction with heuristic search [53].

**Table 2.8** Summary of optimal sensor placement main research areas for SHM

| SPO Research Areas | SPO Criteria | SPO Methodologies |
|---|---|---|
| State Estimation<br>Feedback Control Design<br>Parameter Identification | Fisher Information Matrix (Borguet et al. , 2008) | Deterministic Optimization Methods<br>(Borguet et al., 2008) |
| | Mutual Information Function (Udwadia,1994)<br>Information Entropy (Chang, 1999) | Sequential SPO Methods<br>(Kierkegaard, 1994) |
| | Mean Square Error (Li et al., 2008)<br>Frequency Response Function (Schulz et al., 2008) | Combinatorial Optimization Methods<br>(Zhao et al., 2008) |

## 2.5 Research gap and challenges

Besides the reported limitations of the aforementioned studies in Sec. 2.3.3 and Sec.2.3.4, structural health monitoring is facing some fundamental research challenges [3]. The first one is related to optimal sensor placement which determines the number and locations of the sensors to be deployed in the structures. Most of the existing approaches in this regard are deterministic without considering the impact of uncertainty caused by operational and environmental noise [53, 55]. This limitation will hinder the optimization results from effectively detecting the damage incurred in the structures in a timely manner. In addition, some methods require the number of sensors should be given priori, in which the global optimum is not guaranteed [54].

The second challenge is that, damage is usually a local phenomenon and the signal patterns acquired from vibration sensors of structural damage are nonlinear and nonstationary [12] making the online monitoring of the underlying processes much more challenge. Another fundamental challenge is the low signal to noise ratio resulting from operational and environmental noise which affect the dynamic response of the structure. Thus, the sensitivity of the selected features for damage detection may not be satisfying, and thus causes an unnecessarily long delay for damage detection.

This research conducted in this dissertation is intended to address and fill some gaps from the above identified research challenges. The detailed methodology is presented in Chapters 4-6, and summarized in Chapter 3.

# REFERENCES

1. Adams, D., *Health monitoring of structural materials and components: methods with applications*. 2007: Wiley.
2. Rilling, G., P. Flandrin, and P. Gonçalvés. *On empirical mode decomposition and its algorithms*. 2003.
3. Sohn, H., et al., *A review of structural health monitoring literature: 1996-2001*. 2004: Los Alamos National Laboratory Los Alamos,, New Mexico.
4. Salehian, A., *Identifying the location of a sudden damage in composite laminates using wavelet approach*. 2003, Worcester Polytechnic Institute.
5. Yang, J.N. and Y. Lei. *System identification of linear structures using Hilbert transform and empirical mode decomposition*. 2000: Society of Photo-Optical Instrumentation Engineers.
6. Balageas, D., C.-P. Fritzen, and A. Güemes, *Structural health monitoring*. 2010: Wiley Online Library.
7. D.Montalvao, N.M., A.Ribeiro, *A review of vibration-based structural health monitoring with special emphasis on composite materials.* Shock and Vibration Digest 2006. **38** (4): p. 295–324.

8. J.T.Kim, Y.S.R., H.M.Cho, N.Stubbs *Damage identification in beam-type structures : frequency-based method vs mode-shape-based method.* Engineering Structures, 2003. **25 (1)**: p. 57–67.

9. C.R.Farrar, D.A.J., *Comparative study of damage identification algorithm applied to a bridge : I. Experiment.* Smart Materials&Structures, 1998. **7 (5)**: p. 704–719.

10. A.K.Pandey, M.B., M.M.Samman, *Damage detection from changes in curvature mode shapes.* Journal of Sound and Vibration, 1991. **145(2)**: p. 321–332.

11. Ganguli, M.C.a.R., *Damage assessment of structures with uncertainty by using mode-shape curvatures and fuzzy logic.*

12. Huang, N. and N. Attoh-Okine, *The Hilbert-Huang transform in engineering*. 2005: CRC Press.

13. Yang, J.N., et al., *Hilbert-Huang based approach for structural damage detection.* Journal of engineering mechanics, 2003. **130**(1): p. 85-95.

14. Nag, A., D.R. Mahapatra, and S. Gopalakrishnan, *Identification of delamination in composite beams using spectral estimation and a genetic algorithm.* Smart Materials and Structures, 2002. **11**(6): p. 899.

15. Loewke, K., et al., *Structural health monitoring of composite materials using the two dimensional fast fourier transform.* Smart Mater. Struct.

16. Paget, C.A., et al., *Damage assessment in composites by Lamb waves and wavelet coefficients.* Smart Materials and Structures, 2003. **12**(3): p. 393.

17. Kim, H. and H. Melhem, *Damage detection of structures by wavelet analysis.* Engineering Structures, 2004. **26**(3): p. 347-362.

18. Lemistre, M., et al. *Damage localization in composite plates using wavelet transform processing on Lamb wave signals*. 1999.

19. Salehian, A., Z. Hou, and F. Yuan. *Identification of location of a sudden damage in plates using wavelet approach*. 2003.

20. Huang, N.E., et al., *The empirical mode decomposition and the Hilbert spectrum for nonlinear and nonstationary time series analysis.* Proceedings of the Royal Society of London. Series A: Mathematical, Physical and Engineering Sciences, 1998. **454**(1971): p. 903-995.

21. Quek, S.T., P. Tua, and Q. Wang, *Detecting anomalies in beams and plate based on the Hilbert–Huang transform of real signals.* Smart Materials and Structures, 2003. **12**(3): p. 447.

22. Bernal, D. and B. Gunes. *An examination of instantaneous frequency as a damage detection tool*. 2000.

23. Zemmour, A.I., *The Hilbert-Huang transform for damage detection in plate structures*. 2006.

24. Chiang, L.H., E. Russell, and R.D. Braatz, *Fault detection and diagnosis in industrial systems*. 2001: Springer Verlag.

25. Melhem, H. and H. Kim, *Damage detection in concrete by Fourier and wavelet analyses.* Journal of engineering mechanics, 2003. **129**(5): p. 571-577.

26. Nag, A., D.R. Mahapatra, and S. Gopalakrishnan, *Identification of delamination in a composite beam using a damaged spectral element.* Structural Health Monitoring, 2002. **1**(1): p. 105-126.

27. Farge, M., *Wavelet transforms and their applications to turbulence.* Annual Review of Fluid Mechanics, 1992. **24**(1): p. 395-458.

28. Ihn, J.B. and F.K. Chang, *Detection and monitoring of hidden fatigue crack growth using a built-in piezoelectric sensor/actuator network: I. Diagnostics.* Smart Materials and Structures, 2004. **13**(3): p. 609.

29. Valle, C. and J.W. Littles Jr, *Flaw localization using the reassigned spectrogram on laser-generated and detected Lamb modes.* Ultrasonics, 2002. **39**(8): p. 535-542.

30. Daubechies, I., *Ten lectures on wavelets*. Vol. 61. 1992: SIAM.

31. Rioul, O. and M. Vetterli, *Wavelets and signal processing.* Signal Processing Magazine, IEEE, 1991. **8**(4): p. 14-38.

32. Staszewski, W., *Structural and mechanical damage detection using wavelets.* The Shock and Vibration Digest, 1998. **30**(6): p. 457-472.

33. Silva, M., R. Gouyon, and F. Lepoutre, *Hidden corrosion detection in aircraft aluminum structures using laser ultrasonics and wavelet transform signal analysis.* Ultrasonics, 2003. **41**(4): p. 301-305.

34. Hera, A. and Z. Hou, *Application of wavelet approach for ASCE structural health monitoring benchmark studies.* Journal of engineering mechanics, 2003. **130**(1): p. 96-104.

35. Hou, Z., M. Noori, and R.S. Amand, *Wavelet-based approach for structural damage detection.* Journal of engineering mechanics, 2000. **126**(7): p. 677-683.

36. Guangshu, H., *Digital signal processing—theory, algorithm and realization (the second edition)[M]*. 2003, Beijing: Tsinghua University Press.

37. Huang, N.E., et al., *The empirical mode decomposition and the Hilbert spectrum for nonlinear and nonstationary time series analysis.* Proceedings of the Royal Society of London. Series A: Mathematical, Physical and Engineering Sciences, 1998. **454**(1971): p. 903-995.

38. Vincent, H., S. Hu, and Z. Hou. *Damage detection using empirical mode decomposition method and a comparison with wavelet analysis*. 1999.

39. Yang, J.N., et al., *System identification of linear structures based on Hilbert–Huang spectral analysis. Part 1: Normal modes.* Earthquake engineering & structural dynamics, 2003. **32**(9): p. 1443-1467.

40. Tua, P., S. Quek, and Q. Wang, *Detection of cracks in plates using piezo-actuated Lamb waves.* Smart Materials and Structures, 2004. **13**(4): p. 643.

41. Grassberger, P., T. Schreiber, and C. Schaffrath, *Nonlinear time sequence analysis.* International Journal of Bifurcation and Chaos, 1991. **1**(3): p. 521-547.

42. Grassberger, P. and I. Procaccia, *Measuring the strangeness of strange attractors.* Physica D: Nonlinear Phenomena, 1983. **9**(1-2): p. 189-208.

43. Corana, A., *Parallel computation of the correlation dimension from a time series.* Parallel Computing, 1999. **25**(6): p. 639-666.

44. Williams, G.P., *Chaos theory tamed*. 1997: CRC Press.

45. Diks, C., *The correlation dimension of returns with stochastic volatility.* Quantitative Finance, 2004. **4**(1): p. 45-54.

46. Ristic, L., *Sensor technology and devices.* Measurement Science and Technology, 2000. **11**(12): p. 1829.

47. Staszewski, W., C. Boller, and G.R. Tomlinson, *Health monitoring of aerospace structures: smart sensor technologies and signal processing*. 2004: Wiley.

48. Mukhopadhyay, S. and I. Ihara, *Sensors and technologies for structural health monitoring: a review*, in *new developments in sensing technology for structural health monitoring*. 2011, Springer. p. 1-14.

49. Kim, H.-Y., *Sensors and systems for structural health monitoring*. 2006, Google Patents.

50. Lee, K. *IEEE 1451: A standard in support of smart transducer networking*. in *Instrumentation and Measurement Technology Conference, 2000. IMTC 2000. Proceedings of the 17th IEEE*. 2000: IEEE.

51. Michie, W., G. Thursby, D. Walsh, B. Culshaw, and M. Konstantaki, *Distributed sensing of physical and chemical parameters for structural monitoring.* 1997.

52. Adams, D., *Health monitoring of structural materials and components: methods with applications*. 2007: Wiley.

53. Pukelsheim, F., *Optimal design of experiments*. Vol. 50. 2006: Society for Industrial Mathematics.

54. Cox, D.R. and N. Reid, *The theory of the design of experiments*. Vol. 86. 2000: Chapman & Hall/CRC.

55. Guo, H., et al., *Optimal placement of sensors for structural health monitoring using improved genetic algorithms.* Smart Materials and Structures, 2004. **13**(3): p. 528.

56. Zhong, C. and Z. Shixiong, *Analysis on end effects of EMD method.* Journal of Data Acquisition and Processing, 2003. **18**(1): p. 114-118.

# CHAPTER III

# RESEARCH METHODOLOGY

To address the challenges in structural health monitoring as summarized in Chapter II, this chapter outlines the overall research methodology proposed in this dissertation. In order to achieve the three research objectives, which were identified in Chapter I, we propose three corresponding research tasks. A new sensor placement methodology for damage detection in multistory buildings will be developed (Research Task 1). The proposed method minimizes the uncertainty in parameter estimation in the differential equations modeling process, making the extracted mode shapes less influenced by operational and environmental noise. The correlation dimension, which is a nonlinear effective index to capture the process dynamics, will be utilized in Research Task 2 for damage detection. A prediction based change point detection is created in Research Task 3, the Hilbert instantaneous phase will be used for damage point detection, while the damage severity prediction will be investigated using the energy of the selected IMF within the predicted window. A schematic of the overall methodology is illustrated in Figure 3.1. And the three research tasks are further explained in the following sub-sections.

## 3.1 Research task 1: sensor placement optimization in SHM (Chapter IV)

The proposed methodology uses partial differential equation modeling of the benchmark structure [1] to formulate the optimal criteria for the optimal sensor placement damage detection problem.

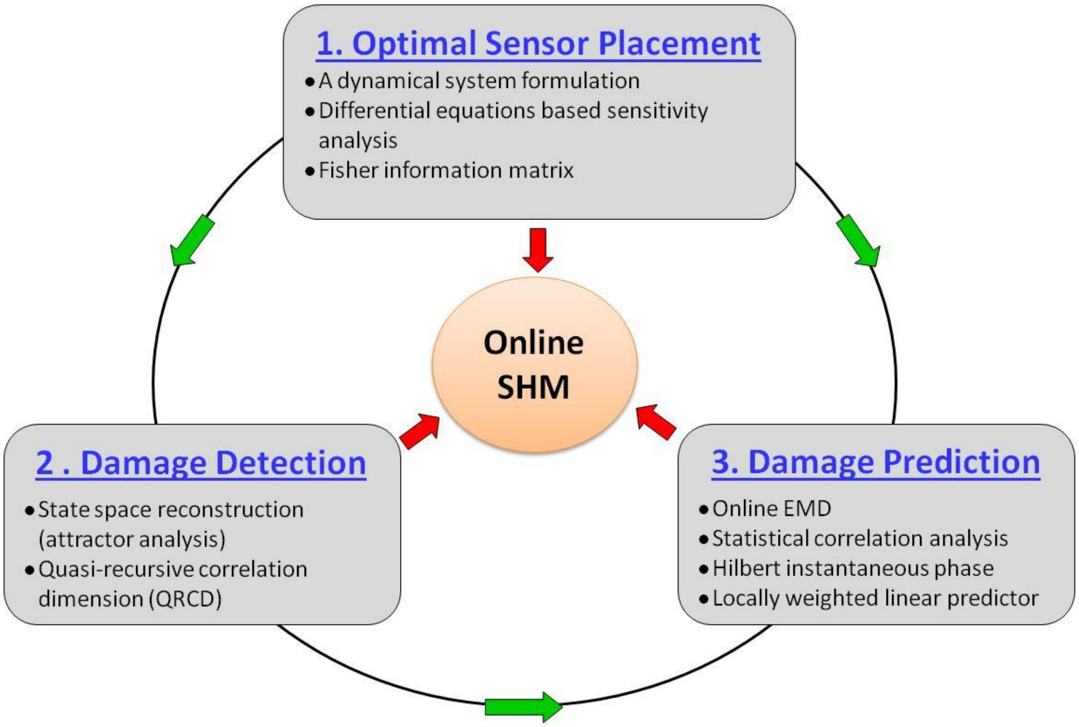

**Figure 3.1** Schematic of the research methodology

An analytical closed form solution of the equivalent ordinary differential system is presented to investigate the dynamic characteristics of the underlying structure. Furthermore, the proposed methodology applies displacement functions to model the displacement of the random field. Moreover, for the sensor placement optimization, the Fisher information matrix (FIM) is used to minimize the overall uncertainty of the estimated parameters. The proposed methodology in Research Task 1 is presented in Chapter IV.

### 3.2 Research task 2: damage detection for online SHM applications (Chapter V)

In this research task, a novel quasi-recursive correlation dimension algorithm (QRCD) for online damage detection of structures based on attractor analysis is developed. It can significantly alleviate the complexity of computation for correlation dimension, and thus make the online monitoring of nonlinear/nonstationary processes using correlation dimension much more applicable and efficient.

After reconstructing the attractor set in state space from the raw time series, the data can be quantified using different forms of dimensions. The correlation dimension is the most popular measure of dimension due to the fact that its calculation is relatively fast, simple and yields a deeper understanding of the underlying dynamic system. Moreover, it has an operational and more rigorous mathematical definition which provides different estimation algorithms to deal with not only experimental time series data, but also simulation data [2].

In order to overcome some of the main limitations of standard G-P algorithm mentioned in Chapter II, a robust quasi recursive algorithm is introduced. The proposed quasi-recursive correlation dimension algorithm reduces the level of computational complexity to $O(N \cdot m_{max} \cdot n_{ri})$ using the overlapping consecutive segmentations. This algorithm Increases the applicability and efficiency of the online monitoring of nonlinear/nonstationary processes using correlation dimension. Moreover, it can be applied to dynamical systems containing long -range interactions, in which all pairs must be included in the computation of the correlation dimension.

The proposed quasi-recursive correlation dimension algorithm lowers the coefficient before the $N^2$, computing simultaneously in a recursive way all distances for embedding dimensions. Additionally, it reduces the level of computational complexity to $O(N \cdot m_{max} \cdot n_{ri})$ using the overlapping consecutive segmentations technique within each embedding dimension. Thus, the online monitoring of nonstationary sensor data using correlation dimension can be carried out in an efficient manner as will be presented in Chapter V.

### 3.3 Research task 3: damage prediction for online SHM (Chapter VI )

To track structural integrity and ensure safe and reliable systems, a novel hybrid method for online structural health monitoring based on the Hilbert energy spectrum and a locally weighted average predictor is presented. The proposed method is based on local empirical mode decomposition (EMD) with *piecewise cubic Hermite interpolation*. Moreover, it uses an adaptive window which is designed to significantly reduce the computational complexity as well as achieving low latency, making the online monitoring and prediction of nonlinear/nonstationary processes much more applicable and efficient.

The empirical mode decomposition algorithm of the entire recorded signal can have undesirable consequences, such as a high computational cost in obtaining IMFs, or obscuring physical interpretation [3]. Thus, an effective online monitoring method for the nonlinear and nonstationary signals based on local empirical mode decomposition with *piecewise cubic Hermite interpolation* is presented.

It should be pointed out that the *Hilbert instantaneous phase* depends on structural parameters such as mass, damping and stiffness [4]. Thus, it is an effective and sensitive feature to be used for change point detection and the *energy* of the predicted IMF will be used to quantify the predicted damaged state.

# REFERENCES

1. Johnson, E., et al., *Phase I IASC-ASCE structural health monitoring benchmark problem using simulated data*. Journal of engineering mechanics, 2003. **130**(1): p. 3-15.
2. Grassberger, P.I.P., *Characterization of strange attractors*. Physical Review Letters, 1983a. **50**(5): p. 346-9.
3. Rilling, G., P. Flandrin, and P. Gonçalvés. *On empirical mode decomposition and its algorithms*. 2003.
4. Salvino, L. and D. Pines. *Structural damage detection using empirical mode decomposition and HHT*. 2002.

# CHAPTER IV

# OPTIMAL SENSOR PLACEMENT FOR SHM UNDER UNCERTAINTY

This chapter addresses sensor placement optimization (SPO) for damage detection in multistory buildings. In the following sections, the sensor placement optimization problem is formulated using partial differential equation modeling and Fisher information matrix based on the American Society of Civil Engineering (ASCE) benchmark structure [36].

## 4.1 Introduction and motivation

Monitoring large civil infrastructures often require multiple sensors at multiple locations. However, it is uneconomical to install sensors to cover the entire structure. Therefore, an optimal sensor placement scheme for structural health monitoring (SHM) applications is crucial. Optimal deployment of sensors plays an important role in developing small, lightweight and energy efficient SHM systems. Many methods have been developed in the field of SPO [1-3]. However, most of these optimization approaches are deterministic with unspecified types and sources of uncertainty [4]. In addition, a predefined number of discrete sensor configurations are required, in which the global optima is not guaranteed [5]. In order to satisfy operational and geometrical constraints, there is a need to combine constraint satisfaction with heuristic search [4].

To tackle this challenge, this research presents a new sensor placement methodology for damage detection in multistory buildings. The proposed method minimizes the uncertainty in parameter estimation in the differential equations modeling process, making the extracted mode shapes of vibrations less influenced by operational and environmental noise.

## 4.2 Review of related research in sensor placement optimization

This section provides a literature review in the area of SPO. It can be classified into three categories, namely, optimal sensor placement methods (Sec. 4.2.1), optimal sensor placement criteria (Sec. 4.2.2), and optimal sensor placement main research areas (Sec. 4.2.3).

### 4.2.1 Sensor placement optimization methods

Sensor placement optimization aims at determining the spatial locations for a collection of sensors, in which the accuracy in parameter identification is maximized [1]. The main research areas and their applications for sensor placement optimization in SHM are summarized in Table 4.1.

**Table 4.1** Classification of research in optimal sensor placement in SHM

| SPO Research Areas | SPO Criteria | SPO Methodologies | SPO Application |
|---|---|---|---|
| State Estimation | Fisher Information Matrix (Borguet et al. , 2008) | Deterministic Optimization Methods (Linear, nonlinear & Integer Programming) (Borguet et al., 2008) | Environmental Protection (Zemmour, 2006) |
| Feedback Control Design | Mutual Information Function (Udwadia,1994)<br>Information Entropy (Chang, 1999) | Sequential SPO Methods (Forward and backward) (Kierkegaard, 1994) | Homeland Security (Chiang et al., 2001) |
| Parameter Identification | Mean Square Error (Li et al., 2008)<br>Frequency Response Function (Schulz et al., 2008) | Combinatorial Optimization Methods (Genetic, Annealing & Monkey algorithms) (Zhao et al., 2008) | SHM:<br>Civil Structures (Meo et al., 2004)<br>Aerospace (Pappa et al., 1998)<br>Laboratory Specimens (Sohn et al., 2002) |

Several sensor placement techniques have been developed using genetic algorithms (GA) in active vibration control [1]. The applicability of combining the GA with evolutionary computation to develop an SPO for SHM schemes is investigated in Ref. [5]. This study presents a tradeoff relationship between the performance of a limited number of sensors and the overall sensor network performance. However, sensor placement optimization methods based on GA often generate invalid solutions during the evaluation process [5].

Gao et al. [6] proposed a probabilistic sensor placement optimization approach, in which for every sensor of a given sensor set, a probabilistic damage detection model is defined over a confident monitoring region. The joint effectiveness of all sensors is estimated as the union of the individual sensor detection probabilities for all sensors within the network. The previous approach uses a covariance matrix adaptation evolution technique for the purpose of searching the decision variable domain. According to Ref. [4], oversimplified probabilistic damage detection models, and unspecified types and sources of uncertainty are two main drawbacks of the probabilistic sensor placement optimization approach.

Integer and combinatorial optimization methods are widely used in SPO for vibration control and noise attenuation [7-10]. Choosing potential sensor locations is a subjective task and may cause significant variation of the optimal solution [8]. A method using the information measure based on the sensitivities of the frequency response function was reported in Ref. [11]. This method not only minimizes the number of sensors placed on a structure but also increases the amount of information gathered by the sensors. However, according to Ref. [4], in order to satisfy operational and geometrical constraints, there is a need to combine constraint satisfaction with heuristic search.

An efficient sensor placement optimization algorithm which uses simultaneous perturbation gradient approximation was reported in Ref. [12]. This multivariate stochastic approximation method takes into account noise in function evaluations or experimental measurements, which makes this particular method efficient for large-dimensional problems. However, its gradient approximation does not guarantee a global optimum [4].

One of the most commonly cited digital signal process techniques used for SHM was developed by Liu et al. [13]. This study demonstrated that the sequential sensor placement algorithm is a relative computationally effective method to obtain a good sensor configuration although it cannot be guaranteed to have an optimal solution.

### 4.2.2 Sensor placement optimization criteria

Optimal sensor placement methods are application dependent. That is, the efficiency of a certain SPO method depends on the evaluation criteria to some extent [14]. In this subsection, some SPO evaluation criteria in SHM applications are reviewed.

One of the most used criteria for SPO is the Fisher information matrix (FIM) presented in Ref. [15]. It uses the determinant of the FIM to identify the sensor array that maximizes both spatial independence and signal strength of the target mode shapes. Statistically, the Fisher information matrix is the inverse of the covariance matrix of the estimate error for an efficient unbiased estimator [16]. To increase the quality of the model parameter estimation relative to the location of sensors, Udwadia [15], proposed that the optimal sensor placement that best estimates the model parameters is that which optimizes some metrics of the FIM. To decrease the uncertainties of the estimates, three metrics of the FIM are used; 1) the trace; 2) the determinant; and 3) the condition number of the FIM. A modified version of the FIM based on the kinetic energy is presented to formulate the optimal criteria for the SPO problem [17, 18]. In the kinetic energy-based method, FIM was weighted with the mass matrix and the objective function is to maximize the measure of the kinetic energy of the structure [18]. The selected sensor positions with possible large amplitudes are expected to increase the signal to noise ratio.

Said and Staszewski [19] employed the mutual information function to determine the optimal sensor locations on a composite plate. By eliminating arbitrary dependences between features obtained from the selected sensor regions, the authors found the optimal sensor placement by maximizing the overall mutual information function. Considering only an equally spaced sensor configuration, the average mutual information between location sets is used to find the optimal sensor spacing on a rectangular plate [20].

According to Chang [21], to improve the quality of the model parameter estimation, the optimal sensor configuration is developed by minimizing the information entropy. The objective function is based on the prediction errors between the analytical and the experimental models. Chang used the information entropy as the measure of the uncertainty in the parameter estimates. The uncertainty in the parameter estimation due to measurement noise, modeling error and unknown excitation, is quantified using probability density functions.

Different from criteria based on information theory, Schulz et al. [22] proposed the frequency response function to formulate the optimal criteria for the SPO damage detection problem. Alternative criteria for SPO for randomly vibrating structures can be achieved by minimizing the mean square error of the response prediction [23].

### 4.2.3 Sensor placement optimization main research areas

Depending on the context, “sensor placement” has been used in the literature in different areas, such as state estimation, feedback control design and parameter identification [24]. The sensor placement optimization for state estimation of distributed systems has been well studied by Kubrusly et al. [25] and Alonso et al. [24]. They proposed a reduced number of measurements for state reconstruction. Moreover, in their studies, they investigated optimality criteria based on principal angles between subspaces. Another approach of SPO for state estimation is related to both distillation column and fixed-bed reactor models [26]. The optimality criterion for locating sensors is based on the covariance matrix of the observability of nonlinear systems.

Design of feedback control systems is another category, where SPO is studied. Chmielewski et al. [27] investigated the sensor placement optimization for the purpose of designing control and monitoring systems. They found that the sensor’s location that yields the best estimate of process variables is the one with pre-specified performance criteria, such as precision and reliability. The problem of placing sensors for feedback control systems has been studied by Green [11], who utilized the performance metric that incorporates worst case spatial disturbances. Moreover, Zhang [28] used systems described by partial differential equations in placing sensors for feedback control systems.

Another category is SPO for parametric identification. Most of the existing related work derives from the theory of experimental design [4-6, 27]. Selecting sensor locations for the purpose of parameter identification is often based on the FIM, which provides a measure closely related to the expected accuracy of the model parameters [7]. Ucinski [8] addressed the optima sensor placement and investigated the optimal trajectories for moving sensors. The minimum number of sensors needed for SHM application was studied by Kirkegaad et al. [9].

Optimal sensor placement applications cover several related and overlapping research fields such as condition monitoring of machines and structures, damage detection, structural integrity, and assessment and failure prevention [29]. The types of structures include aerospace, aircraft and civil infrastructures such as bridges and buildings. Other applications include, but not limited to, environmental protection [30], homeland security for early warning and detection of possible bioterrorist attacks [31] and vibration control of large flexible space structures and noise control of aircraft fuselages [32].

In the present study, a new optimal sensor placement methodology for damage detection in multistory buildings under uncertainty is developed. The proposed methodology has the following advantages: 1) partial differential equation modeling of the benchmark structure is proposed to formulate the optimal criteria for the SPO damage detection problem. The dynamic characteristics of the underlying structure are accurately calculated using a closed form solution of the equivalent ordinary differential system. Moreover, instead of using partial differential equations (PDEs) for each node in the Finite Element Method (FEM), displacement functions are used, which reduce the computational time with a satisfying accuracy; and 2) a multi-component objective function based on FIM is used to minimize the overall uncertainty of the estimated parameters. The proposed methodology includes the following steps: 1) structural partial differential equation formulation and model validation; 2) correlation analysis; 3) sensor placement optimization. The overall proposed methodology is illustrated in Figure 4.1.

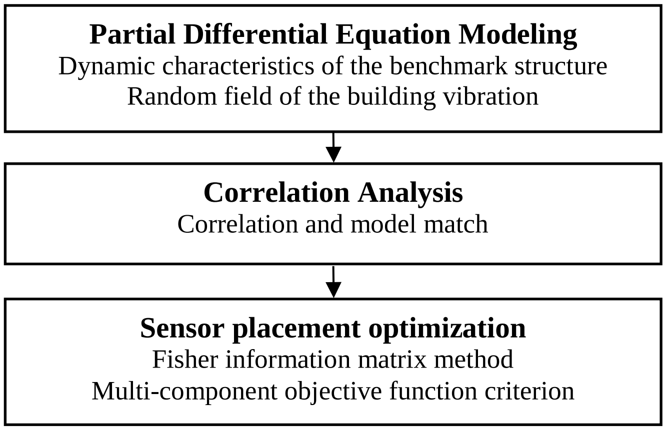

**Figure 4.1** The overall optimal sensor placement methodology

### 4.3 Dynamic response for multistory buildings using PDE modeling

In this section, the dynamic response for multistory buildings is formulated using an equivalent continuum model consisting of flexural and shear cantilever beams, respectively, with a lateral deformation as shown in Figure 4.2.

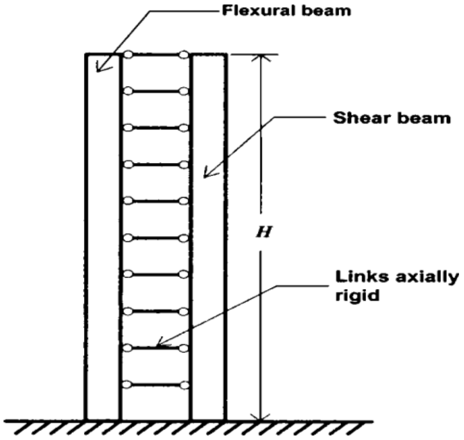

**Figure 4.2** Simplified continuous model to estimate the horizontal dynamic response for multistory buildings [33]

In order to transmit horizontal forces, flexural and shear cantilever beams are assumed to be connected by infinitely many axially rigid members. Moreover, floor masses are assumed to remain constant along the height of the building. Accordingly, the free response of the continuous model shown in Figure 4.2 is given by the following partial differential equation (PDE) [33]:

$$\frac{1}{EI_0}\left(\rho(z)\frac{\partial^2 u(z,t)}{\partial t^2}+c(z)\frac{\partial u(z,t)}{\partial t}\right)+\frac{1}{H^4}\frac{\partial^2}{\partial z^2}\left(S_1(z)\frac{\partial^2 u(z,t)}{\partial z^2}\right)-\frac{\alpha_0^2}{H^4}\frac{\partial}{\partial z}\left(S_2(z)\frac{\partial u(z,t)}{\partial z}\right)=0 \quad (4.1)$$

where $\rho(z)$; is the mass per unit length in the underlying model; $u(z,t)$ represents the lateral displacement height $z$ at time $t$; $c(z)$ is the damping coefficient per unit length; $EI_0$ is the flexural rigidity of the flexural beam at the base of the structure; $H$ is the total height of the multistory building; and $\alpha_0$, $S_1(z)$ and $S_2(z)$ are non-dimensional parameters given by

$$\alpha_0 = H\left(\frac{GA_0}{EI_0}\right)^{0.5}, \quad S_1(z)=\frac{EI(z)}{EI_0}, \quad S_2(z)=\frac{GA(z)}{GA_0}$$

where, $GA_0$ is the shear rigidity of the shear beam at the base of the building; $EI(z)$ and $GA(z)$ are the flexural rigidity of the flexural beam and the shear rigidity of the shear beam along the height, respectively.

The overall lateral deformation of the multistory building is controlled by the dimensionless parameter $\alpha_0$. In multistory buildings, a value of $\alpha_0 = 1.5$ corresponds to a combined shear and flexural deformations model [42].

## 4.4 The differential equation modeling of the ASCE benchmark structure

In this section, the ASCE benchmark structure is briefly reviewed (Sec. 4.4.1). Followed by a PDE analytical model to predict the horizontal dynamic response of the four-story building, when subjected to horizontal forced excitations (Sec. 4.4.2).

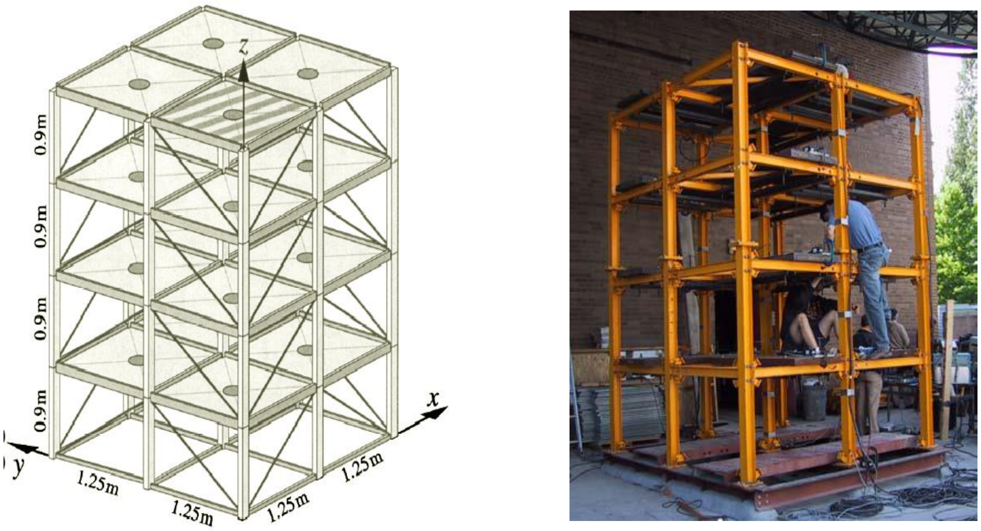

**Figure 4.3** Benchmark structure: (left) Diagram of the analytical model and (right) Steel-frame structure [34]

### 4.4.1 ASCE benchmark structure

The benchmark structure was designed by the American Society of Civil Engineering (ASCE) for the application of SHM. It is a 4-story, 2-bay by 2-bay steel frame scale model structure and one floor slab per bay per floor as shown in Figure 4.3. It is located in the Earthquick Engineering Research Laboratory at the University of Britsh Columbia Available (http://wusceel.cive.wustl.edu/asce.shm/). It consists of a symetric plan with an area of 2.5 m by 2.5 m and a height of 3.6 m. Properties of the benchmark structural members are given in Table 4.2 [34].

**Table 4.2** Properties of the benchmark structural members

| Property | Columns | Floor beams | Braces |
|---|---|---|---|
| Section type | B100 x 9 | S75 x 11 | L25 x 25 x 3 |
| Cross-sectional area *A* ($m^2$) | $1.133 \times 10^{-3}$ | $1.43 \times 10^{-3}$ | $0.141 \times 10^{-3}$ |
| Moment of inertia (strong direction) $I_y$ ($m^4$) | $1.97 \times 10^{-6}$ | $1.22 \times 10^{-6}$ | 0 |
| Moment of inertia (week direction) $I_x$ ($m^4$) | $0.664 \times 10^{-6}$ | $0.249 \times 10^{-6}$ | 0 |
| St. Venant torsion constant *J* ($m^4$) | $8.01 \times 10^{-9}$ | $38.2 \times 10^{-9}$ | 0 |
| Young's modulus *E* (Pa) | $2 \times 10^{11}$ | $2 \times 10^{11}$ | $2 \times 10^{11}$ |
| Shear modulus *G* (Pa) | E/2.6 | E/2.6 | E/2.6 |
| Mass per unit length (Kg/m) | 8.89 | 11.0 | 1.11 |

As illustrated in Figure 4.3, a bracing system placed along the diagonal was fixed for each bay. To emulate a real structure, a concrete slab was built on each floor, and the removal of this bracing system is designed to simulate damage to the structure. For the experiment wind ambient excitation, two types of forced excitation sources were applied, namely, impact hammer test and electrodynamics shaker. A more detailed description of the benchmark structure problem can be found in the work of Johnson et al. [34]. A simulation program for generating the response of force sensor data in the ASCE benchmark structure is available in Ref. [35]. It is a MATLAB program based on a 120- degrees of freedom (DOF) finite element model [34]. It assumes the movement of floors as perfect rigid bodies in a continuum system, while floor nodes have only horizontal translation and rotation about the central column. Columns and floor beams are modeled as elastic Euler-Bernoulli beams. Braces are modeled as axial bars with no bending stiffness. Moreover, roof acceleration is modeled as independent filtered Gaussian white noise. The finite element model assumes a root mean square (RMS) 10% of the largest RMS of the acceleration response [34]. One undamaged pattern and six damage patterns generated from this benchmark model were used, defined in Table 4.3 and shown graphically in Figure 4.4 [36].

**Table 4.3** Damage patterns of the ASCE benchmark structure [36]

| Damage pattern | Damage description |
|---|---|
| $D_0$: Damage pattern zero | No damage |
| $D_1$: Damage pattern one | Remove all braces in 1st floor. |
| $D_2$: Damage pattern two | Remove all braces in 1st and 3rd floor. |
| $D_3$: Damage pattern three | Remove a brace near sensor location 2 at 1st floor |
| $D_4$: Damage pattern four | Damage pattern 3 & remove a brace near sensor 9 at 3rd floor. |
| $D_5$: Damage pattern five | Damage pattern 4 & loosen floor beam near sensor 3 at 1st floor. |
| $D_6$: Damage pattern six | Remove 2/3 stiffness of a brace near sensor 2 at the 1st floor. |

### 4.4.2 The proposed differential equation model for predicting the dynamic response

The focus of this research is to formulate a continuum PDE model to predict the *horizontal* dynamic behavior of the benchmark structure, described in section (4.4.1). The proposed equivalent models consist of flexural and shear cantilever beams deforming in lateral configurations.

To predict the global horizontal dynamic behavior, floors are assumed to be perfectly rigid in plane with a uniform distributed consistent mass and are modeled using three global degrees of freedoms (translation in the *x* and y directions and rotation about the center column) per floor. On the other hand, to predict the local horizontal dynamic behavior, floors are assumed to be piece-wise rigid in plane and are modeled using two local degrees of freedoms (translation in *x* and y directions) at each coordinate of the lumped mass.

Several other assumptions were made as follows prior to formulating the continuum PDE model of the benchmark structure:

1) Floor masses remain constant along the height of the building;
2) The whole benchmark structure is modeled as a continuum model with a flexural cantilever beam and a shear cantilever beam;
3) Braces are modeled as axial bars; and
4) The columns and floor beams are modeled as Euler-Bwennoulli beams.

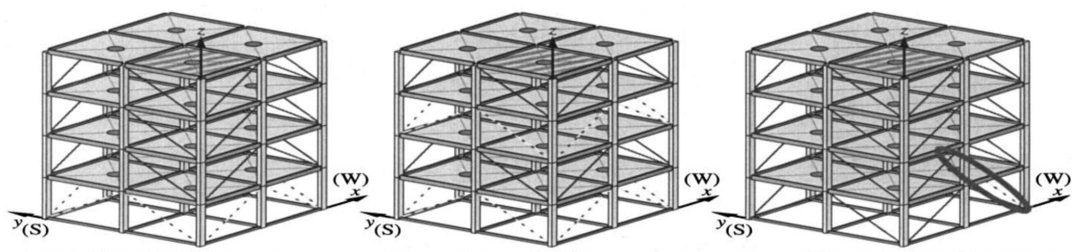

(*i*) no stiffness in 1st floor braces (*ii*) no stiffness in 1st floor braces
no stiffness in 3rd floor braces (*iii*) no stiffness in one 1st floor brace

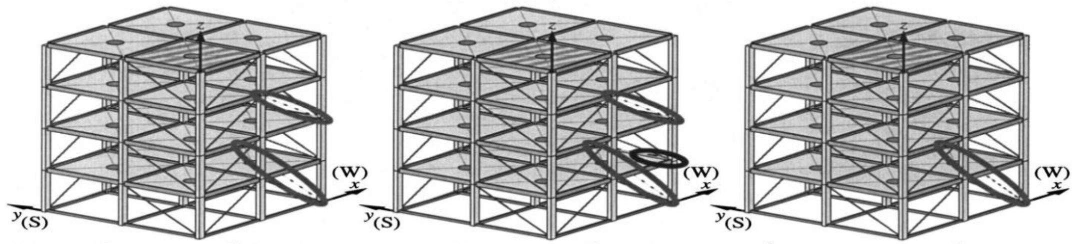

(*iv*) no stiffness in one 1st floor brace
no stiffness in one 3rd floor brace (*v*) no stiffness in one 1st floor brace
no stiffness in one 3rd floor brace
beam-column connection weakened (*vi*) $^2/_3$ stiffness in one 1st floor brace

**Figure 4.4** Six damage patterns generated from the benchmark model [36]

With the assumptions mentioned above and Equation (4.1), the overall lateral affine deformation of the un-damped healthy benchmark structure when subjected to horizontal roof excitation can be expressed by the following partial differential equation,

$$\frac{\rho(z)}{EI_1}\left(\frac{\partial^2 u(x,y,z,t)}{\partial t^2}\right)+\frac{1}{H^4}\frac{\partial^2}{\partial z^2}\left(S_1(z)\frac{\partial^2 u(x,y,z,t)}{\partial z^2}\right)-\frac{\alpha_0^2}{H^4}\frac{\partial}{\partial z}\left(S_2(z)\frac{\partial u(x,y,z,t)}{\partial z}\right)=-\frac{\rho(z)}{EI_1}\frac{\partial^2}{\partial t^2}f_e(t)_x \tag{4.2}$$

$$\frac{\rho(z)}{EI_1}\left(\frac{\partial^2 v(x,y,z,t)}{\partial t^2}\right)+\frac{1}{H^4}\frac{\partial^2}{\partial z^2}\left(S_1(z)\frac{\partial^2 v(x,y,z,t)}{\partial z^2}\right)-\frac{\alpha_0^2}{H^4}\frac{\partial}{\partial z}\left(S_2(z)\frac{\partial v(x,y,z,t)}{\partial z}\right)=-\frac{\rho(z)}{EI_1}\frac{\partial^2}{\partial t^2}f_e(t)_y \tag{4.3}$$

where, $\alpha_0 = H\left(\frac{GA_1}{EI_1}\right)^{0.5}$, $S_1(z) = \frac{EI(z)}{EI_1}$, $S_2(z) = \frac{GA(z)}{GA_1}$, $GA_1$ and $EI_1$ are the shear rigidity of the shear beam and the flexural rigidity of the flexural beam at the roof of the building, respectively; $u(x,y,z,t)$ and $v(x,y,z,t)$ are the lateral displacement at height *z* at time *t* and spatial domain *(x,y)* in *x*- direction and *y*- direction, respectively*;* $z \in \{0.9, 1.8\ , 2.7, 3.6\}\ and\ \ x = y\ \in [0, 2.5]$ represent the height and the symmetric dimensions of the benchmark structure's four floors, respectively; $f_e(t)_x$ and $f_e(t)_y$ are the forced excitation function for the benchmark structure in both the lateral *x*- direction as well as in lateral *y*- direction, respectively. Parameters $S_1(z)$ and $S_2(z)$ control the variation of flexural rigidity and shear rigidity along the height in the flexural and shear beams, respectively.

Following Ref. [42], a value of the lateral stiffness ratio $\alpha_0$ of 1.5 best controls the degree of participation of overall flexural and overall shear deformations of the benchmark structure with $EI_1$ equals to 0.04 and $GA_1$ has a value of 0.007. In the above PDEs (Equation 4.2 and Equation 4.3), applying the properties of the benchmark structural members mentioned in Table 4.2, two components need to be identified in each lateral direction; the excitation force $f_e(t)$ as well as the lateral displacement at height *z* at time *t* and spatial domain *(x,y).*

#### 4.4.2.1 Formulation of the excitation force

In the benchmark structure, the mechanical mass shaker was used as an excitation and it was located on the roof at the top of the center column. According to Ref. [37], the mechanical essentric mass shaker generates sinusoidal excitation horizontal directions. Let $\varepsilon \in N(0,1)$ be a random variable which accounts for modeling errors. Then, the harmonic excitation force in *x*-direction can be mathematically represented by,

$$f_e(t)_x = A\sin(\omega t + \varphi + \varepsilon_t) + \varepsilon_t{}^* \tag{4.4}$$

where, $A$ and $\varphi$ are the amplitude and the phase shift of the oscillation, respectively; $\omega$ is the angular frequency of the excitation force ; $\varepsilon_\mathrm{t}$ and $\varepsilon_\mathrm{t}{}^*$ are the measurement noise and the dynamical noise, respectively.

In this study, since the excitation force in both *x* and *y* directions are generated using the same frequency and phase with only different amplitude, then the relationship between the forced excitation function in *x* and *y* directions is assumed to be,

$$f_e(t)_x = (1.09)f_e(t)_y$$

To further investigate the dynamic response of the underlying structure subjected to a lateral excitation, the floors are assumed to be semi-rigid in plane and modeled using two local degrees of freedom (translation in *x* and y directions) at each coordinate of the lumped mass. In addition, a stochastic random field of the building vibration is formulated by expanding the suitable displacement functions as truncated series in *x* and *y* directions with coefficients as functions of *z*.

#### 4.4.2.2 The lateral displacement

According to Ref. [33], the elastic behavior response of the structure can be calculated as the sum of the response of individual modes of vibration. Thus, the lateral displacements $u(x,y,z,t)$ and $v(x,y,z,t)$ will be further analyzed at height *z* and time *t* as a linear combination of the modal response,

$$u(z,t) = \sum_{i=1}^{\infty} u_i(z,t) \tag{4.5}$$

$$v(z,t) = \sum_{i=1}^{\infty} u_i(z,t) \tag{4.6}$$

where, $u_i(z,t) = \Gamma_i \phi_i(z) D_i(t)_x$ and $v_i(z,t) = \Gamma_i \phi_i(z) D_i(t)_y$. For the benchmark structure, it has been found that the first three modes of vibration are enough to represent the general elastic behavior of the building [33]. Thus, Equation (4.5) and Equation (4.6) become,

$$u(z,t) = \sum_{i=1}^{3} u_i(z,t) = \sum_{i=1}^{3} \Gamma_i \, \phi_i(z) D_i(t)_x \tag{4.7}$$

$$v(z,t) = \sum_{i=1}^{3} v_i(z,t) = \sum_{i=1}^{3} \Gamma_i \, \phi_i(z) D_i(t)_y \tag{4.8}$$

where, $u_i(z,t)$ and $v_i(z,t)$ stand for the contribution of the *i*-th mode to the total response at height *z* and time *t* in *x* and *y* directions, respectively; $\Gamma_i$ is the modal participation factor of the *i*-th mode of vibration; $\phi_i(z)$ is the *i*-th mode shape of vibration at height *z*; and $D_i(t)_x$ and $D_i(t)_y$ are the deformation response at time *t* of the underlying system corresponding to the *i*-th mode of the building vibration in *x* and *y* directions, respectively.

Moreover, the modal participation factor $\Gamma_i$ in a continuum modal with uniformly distributed mass can be written in terms of mode shapes of the vibration as follows [33],

$$\Gamma_i = \frac{\int_0^1 \phi_i(z)dz}{\int_0^1 \phi_i^2(z)dz} \tag{4.9}$$

#### 4.4.2.3 Formulation of the displacement functions

According to Ref. [40], displacement functions within the stochastic random field of each floor in *x* and *y* directions are designated by *u* and *v*, respectively (see Figure 4.5) and formulated as [40],

$$u(x,y,z) = u_0(z) + x u_1(z) + x^2 u_2(z) \tag{4.10}$$

$$v(x,y,z) = v_0(z) + y v_1(z) + y^2 v_2(z) \tag{4.11}$$

The displacement functions are considered to be dependent on time as well as space. So, $u_i(z)$ is $u_i(z,t)$ and $v_i(z)$ is $v_i(z,t)$ for each $i \in \{1, 2, 3\}$.

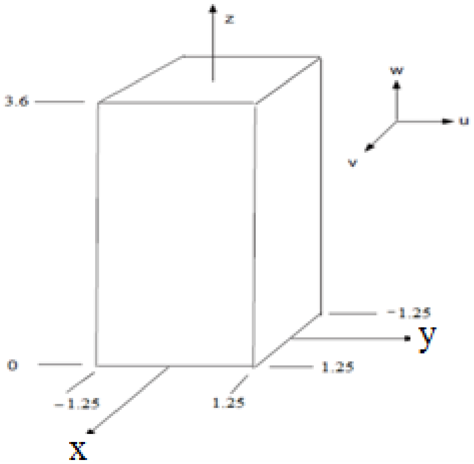

**Figure 4.5** Illustration of displacements in the *x*, *y*, and *z* directions [40]

### 4.4.3 Representative ordinary differential equations

Using the method of separation of variables in Equation (4.7), then Equation (4.2) leads to the following two ordinary differential equations (Appendix A1),

$$\frac{d^2 D_i(t)}{dt^2} + \omega_i^2 D_i(t) + \ddot{f}_e(t)_x = 0 \tag{4.12}$$

$$\frac{d^2}{dz^2}\left(S(z)\frac{d^2\phi_i(x,y,z)}{dz^2}\right) - \frac{\alpha_0^2 d}{dz}\left(S(z)\frac{d\phi_i(x,y,z)}{dz}\right) - \omega_i^2 \frac{H^4}{EI_1}\rho(z)\phi_i(x,y,z) = 0 \tag{4.13}$$

Boundary conditions that are relevant to the experimental setting are those at the fixed bottom (*z=0*) and the free top (*z=3.6*) of the continuum model and can be expressed as,

When *z=0*

$$\phi_i(z) = 0 \text{ and } \frac{d\phi_i(z)}{dz} = 0 \tag{4.14}$$

And when *z=3.6*

$$EI\frac{d^2\phi_i(z)}{dz^2} = 0 \text{ and } EI\frac{d^3\phi_i(z)}{dz^3} = 0 \tag{4.15}$$

The first two boundary conditions imply null displacement and rotation at the bottom of the benchmark structure, while the last two boundary conditions imply no moment and shear forces at the free end top of the underlying structure.

Similarly, the ODE system describes the horizontal dynamic response of the benchmark structure in *y*-direction is identical to the ODE system in *x*-direction except the following equation,

$$\frac{d^2D_i(t)}{dt^2} + \omega_i^2 D_i(t) + \ddot{f}_e(t)_y = 0 \tag{4.16}$$

### 4.4.4 The approximated acceleration of the benchmark structure in *x*-direction

According to Ref. [33], to approximate the acceleration of the benchmark structure, there is a need to combine the first three modes of vibration of the benchmark structure along with the model participation factor of the *i*-th mode of vibration at height *z* as shown in Figure 4.6 and expressed by the following Equation,

$$a(z,t) \cong \sum_{i=1}^{3} \Gamma_i\, \phi_i(z)\ddot{D}_i(t)_x \tag{4.17}$$

where, $\ddot{D}_i(t)$ is the relative acceleration of the *i*-th mode of the building vibration in *x*-direction.

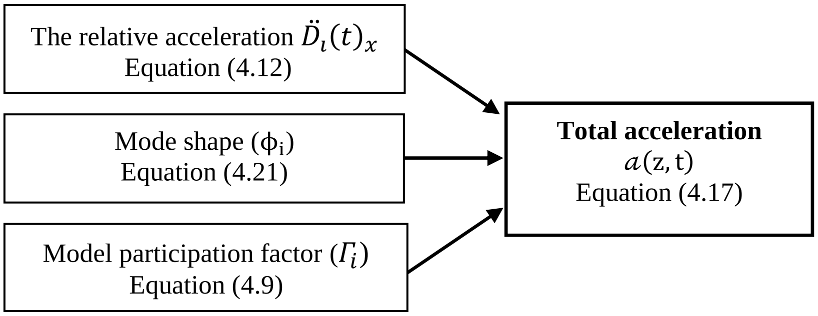

**Figure 4.6** The overall procedure of approximating the acceleration in *x*-direction

Next, using the displacement functions (Equation (4.10) and Equation (4.11)), the acceleration in *x*-direction and *y*-direction can be expressed as follows,

$$\ddot{u}(x,y,z,t) = \sum_{i=1}^{3} \ddot{D}_i(t)_x \left[\Gamma_i\phi_i(z) + x(\Gamma_i\phi_i(z)+1) + x^2\left(\Gamma_i \frac{d^2\phi_i(z)}{dz^2} + \frac{d\phi_i(z)}{dz}\,\frac{1}{\phi_i(z)}\right)\right] \tag{4.18}$$

$$\ddot{v}(x,y,z,t) = \sum_{i=1}^{3} \ddot{D}_i(t)_y \left[\Gamma_i\phi_i(z) + y(\Gamma_i\phi_i(z)+1) + y^2\left(\Gamma_i \frac{d^2\phi_i(z)}{dz^2} + \frac{d\phi_i(z)}{dz}\,\frac{1}{\phi_i(z)}\right)\right] \tag{4.19}$$

The formulation of the acceleration in Equation (4.18) and Equation (4.19) will be used to formulate the Jacobian matrix for the sensor placement optimization, which will be discussed in Section (4.6).

*Analytical solution for the proposed differential equation system*

For a uniform stiffness along the height of the benchmark structure ($S_1(z) = S_2(z)$=1), Equation (4.12) can be simplified as [43],

$$\frac{d^4\phi_i(z)}{dz^4} - \beta^4\phi_i(z) = 0 \tag{4.20}$$

where, $\beta^4 = \frac{\rho(z)\omega_i^2}{EI}$. Using the general solution of Equation (4.20) and the boundary conditions (Equation (4.14) and Equation (4.15)), the mode shape of vibration corresponding to the *i*-th mode with a uniform stiffness along the height can be obtained by (Appendix A2)

$$\phi_i(z) = \left(\cosh(\beta_i z) - \cos(\beta_i z)\right) - \frac{\cosh(3.6\beta_i)+\cos(3.6\beta_i)}{\sinh(3.6\beta_i)+\sin(3.6\beta_i)}\left(\sinh(\beta_i z) - \sin(\beta_i z)\right) \tag{4.21}$$

According to Miranda et al. [42], the eigenvalue parameter ($\beta_i$), corresponding to the *i*-th mode of vibration can be found using the associated characteristic equation, which in our application has been found to be (Appendix A3),

$$1 + \cos(3.6\beta_i)\cos\text{h}(3.6\beta_i) = 0 \tag{4.22}$$

where, $\beta_i \cong 0.5208$, 1.3039 and 2.1819, are the numerical solutions for *i*= 1, 2, 3 respectively.

## 4.5 Validation of the proposed differential equation model

To verify the proposed PDE model, there is a need to compare the approximated acceleration generated by the PDE model with the experimental data using the Model Assurance Criterion (MAC) [42]. The Model Assurance Criterion is often utilized to pair mode shapes derived from analytical models and test measurements [45]. The MAC is defined as a scalar constant relating the degree of consistency between the reference model vector $d$ and another model vector *c* with respect to a mode shape *r* as follows [45],

$$MAC_{cdr} = \frac{\left|\{\psi_{cr}\}^T\{\psi_{dr}^*\}\right|^2}{\{\psi_{cr}\}^T\{\psi_{cr}^*\}\{\psi_{dr}\}^T\{\psi_{dr}^*\}}$$

Here, $\psi$ represents model coefficient; $T$ is the transpose; $*$ is the complex conjugate; $\{\}$ is a vector. The MAC provides a measure of consistency, which is a confidence factor in the evaluation of a model vector from different excitation locations or different model parameter estimation algorithms [45]. The MAC values lie between zero and one. A value close to one shows a good correlation between eigenvectors under consideration while a value close to zero indicates no consistent correspondence. To evaluate the proposed PDE model, the MAC is expressed as follows,

$$MAC(Exp, PDE) = \frac{\left|\sum_{i=1}^{N}(a_{Exp})_i(a_{PDE})_i^{\,T}\right|^2}{\left(\sum_{i=1}^{N}(a_{Exp})_i(a_{Exp})_i^{\,T} \cdot \sum_{i=1}^{N}(a_{PDE})_i(a_{PDE})_i^{\,T}\right)}$$

in which $(a_{PDE})$ computed from Equation (4.11) and $(a_{Exp})$ are the experimental and analytical (PDE) acceleration vectors, from a combined first three mode shapes, respectively; and *N* denotes the total global master degrees of freedom (translation in *x* and *y* directions and rotation about the center column). A general overview of how well the test data and the PDE model of the benchmark structure agree in all degrees of freedom using the MAC technique is shown in Table 4.4.

**Table 4.4** MAC values of the undamaged acceleration random field for experimental and initial PDE models

| Forced excitation (Noise to Signal ratio10%) | First floor | Second floor | Third floor | Fourth floor |
|---|---|---|---|---|
| MAC value | 0.887 | 0.879 | 0.853 | 0.836 |

In practical applications, if the MAC value is less than 0.6, then it is highly recommended that the correlation and the consistency between the underlying models and experimental data are questionable [49]. Generally, high MAC values ($\geq 0.8$) imply a good correlation between the analytical and the experimental models [51]. For the MAC values in Table 4.4, the minimum value is 0.836, suggesting a good correlation between the PDE model and the experimental data.

### 4.6 A dynamical system formulation of the sensor placement problem

In this section, the Fisher information matrix (FIM) will be utilized to solve the sensor placement problem.

#### 4.6.1 Fisher information matrix for sensor placement optimization

According to Refs.[54, 59], the FIM can be written as,

$$FIM = \boldsymbol{\phi}^{\boldsymbol{T}}\boldsymbol{\phi}$$

Here, $\boldsymbol{\phi}$ refers to the Jacobian matrix of the acceleration [61] of the multistory structure with respect to each sensor location. The Jacobian matrix formulation is illustrated in Appendix A4. Using the Singular Value Decomposition (SVD) [60], $\boldsymbol{\phi}$ can be defined as,

$$\boldsymbol{\phi} = USV^T$$

where, $U \in \mathbb{R}^{m\times m}, V \in \mathbb{R}^{n\times n}$ is an orthogonal matrix whose columns are left (right) singular vectors that define an orthonormal basis for the output sensor measurement space and for the input parameter space, respectively; and $S \in \mathbb{R}^{m\times n}$ is a rectangular diagonal matrix with nonnegative real numbers on the diagonal called singular values $\sigma$.

#### 4.6.2 The Objective function based on Fisher information matrix

In this study, the objective function has three components. The first one is based on the determinant of FIM [64] which is the product of the singular values. The determinant of FIM has to be maximized since its inverse is a measure of the overall uncertainty on the estimated parameters [1]. The second component of the objective function for the sensor placement is the trace of the FIM [64] defined as the sum of the singular values. The last component of the objective function is the condition number of the FIM [37] which is defined as the ratio of the largest to the smallest singular value. Each of the previous metrics emphasizes on a specific aspect of the optimization problem. Thus, it is recommended to combine them in aggregated Figure of Merit (FOM), which should be maximized and can be expressed as [64],

$$FOM = w_1(CN) + w_2(Tr) - w_3(Dt)$$

where, CN, Tr and Det are the condition number, trace and determinant of the FIM, respectively; $w_i$ are weighting factors between the components of the objective function.

### 4.7 Application to ASCE benchmark problem

This section uses the benchmark structure as a case study for the proposed optimal sensor placement methodology. Three different optimization algorithms, namely, Sequential Space Filling (SSF) [46], Genetic Algorithm (GA) [1-2], and the Simulated Annealing Algorithm (SA) [55] were adopted to optimize the final locations of the eight sensors.

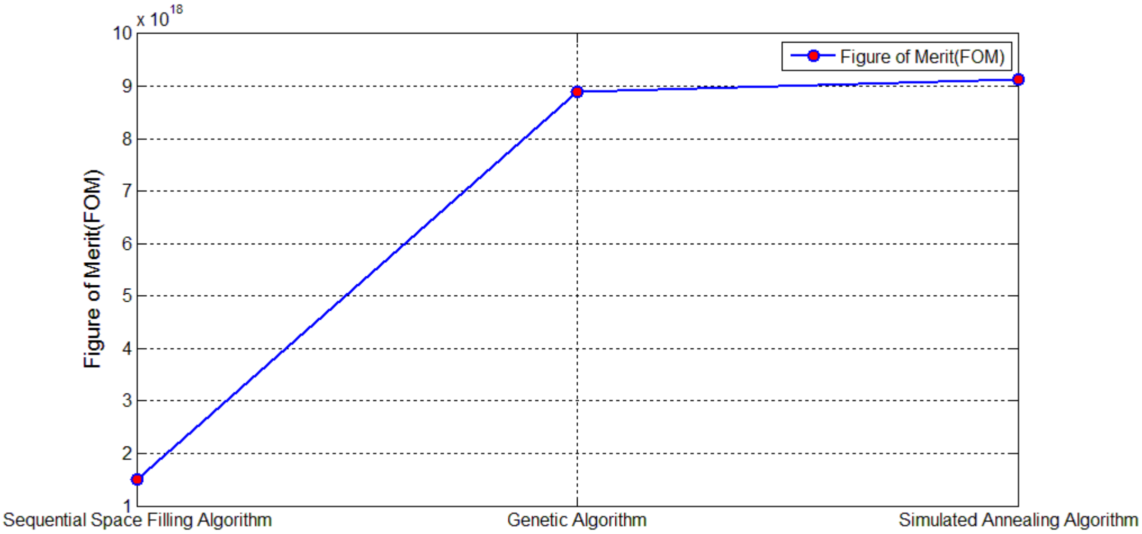

**Figure 4.7** Performance comparison of the FOM for different optimization algorithms

After running each method thirty times and choosing the best results for each method, it has been found that the performance of the Simulated Annealing algorithm is the best in solving the sensor placement problem in the optimality of sensor location (see Figure 4.7).

### 4.7.1 Optimization of the sensor configuration using the Simulated Annealing Algorithm

Simulated Annealing is a probabilistic method to find the global optimal of an objective function that may possess several local optimal [47]. The SA is analogue to the physical process in thermodynamics, especially to the way that liquids freeze and crystallize, or metals cool and anneal [47]. The algorithm starts with a random initial sensor configuration then the perturbation operator works on each decision variable. In an iteration of the SA, each variable is randomly selected for perturbation and the new sensor configuration is randomly found around its neighbors, where the distance of random search is proportional to the annealing temperature. Next, the new sensor configuration is compared with the previous one and the a better solution with respect to the objective function is always accepted, while the weaker solution is accepted only if a randomly threshold is greater than a probability value which is defined in Ref. [61] by,

$$p = e^{(\Delta E/T)}$$

in which $\Delta E$ denotes the change in objective function value (FOM) and $T$ is the temperature control parameter which will be gradually reduced until the objective function value has converged or reach maximum number of iteration.

### 4.7.2 Optimization results and discussion

A schematic of the benchmark structure is shown in Figure 4.8, where the locations of the existing sixteen sensors are indicated by circles (four sensors in each floor). Moreover, the 3D graphic random field of the objective function (Figure of Merit) for the fourth floor is shown in Figure 4.9.

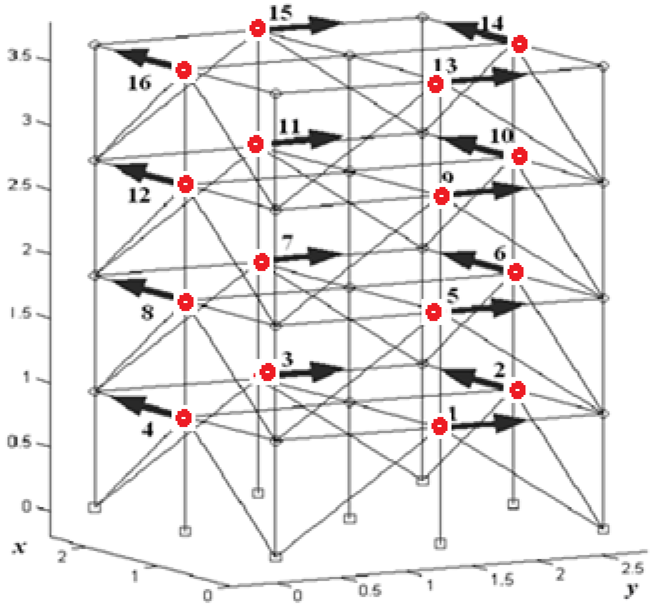

**Figure 4.8** Existing placements of sensors on the ASCE benchmark structure [34]

In this section, the optimal sensor placement of the benchmark structure is studied using the simulated annealing algorithm (SA). Eight sensor locations are randomly selected as an initial input and a 0.98 of cooling factor is applied.

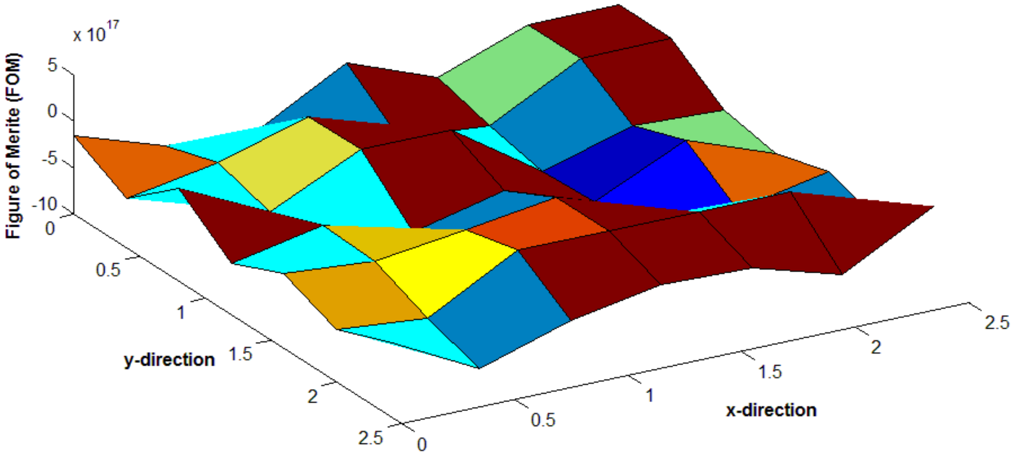

**Figure 4.9** 3D graphic random field for the fourth floor of the benchmark structure

Applying unit weights to each component of the FOM, the objective function of the FIM is computed as shown graphically in Figure 4.10. Moreover, the optimal sensor coordinates are given in Tables 4.5 and shown in Figure 4.11.

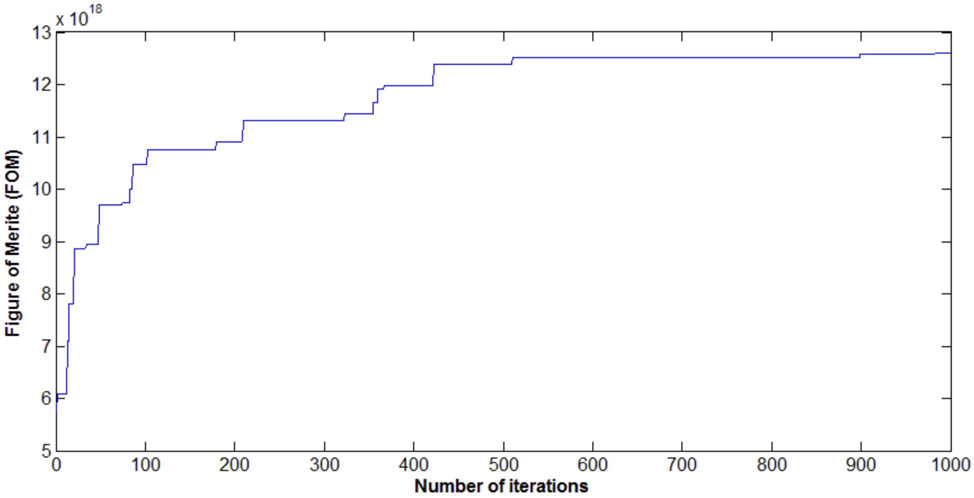

**Figure 4.10** Figure of Merit using simulated annealing algorithm

**Table 4.5** Optimal sensor coordinates based on the Figure of Merit

| Sensor number | $S_1$ | $S_2$ | $S_3$ | $S_4$ |
|---|---|---|---|---|
| Coordinates | (0.0, 2.2, 0.9) | (2.2, 0.3, 0.9) | (0.1, 2.5, 1.8) | (0.2, 2.5, 1.8) |
| Sensor number | $S_5$ | $S_6$ | $S_7$ | $S_8$ |
| Coordinates | (0.6, 2.3, 2.7) | (2.5, 0.0, 2.7) | (2.4, 0.4, 3.6) | (0.7, 1.4, 3.6) |

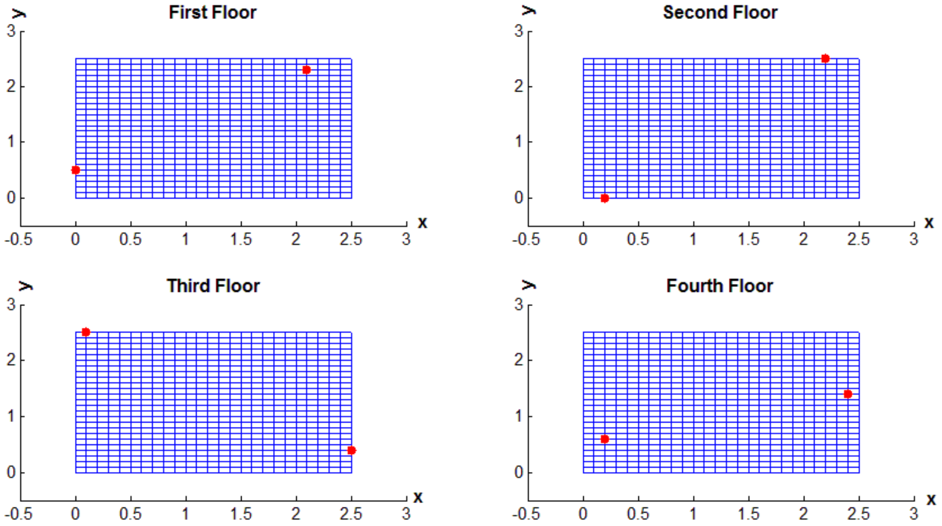

**Figure 4.11** Optimal sensor locations for the four floors of the benchmark structure

Based on the optimization results, it is observed that the FOM values converge directly after 150 iterations with a maximum average value of $12.6 \times 10^{18}$. From Table 4.5, it can be seen that the optimal sensor locations are located near the boundaries of the benchmark structures. This result may due to the nature of the bracing system placed diagonally on each floor of each exterior face. In fact, the removal of this bracing system is designed to simulate damage to the benchmark structure.

### 4.7.3 Capability of damage detection for the ASCE benchmark structure

In order to validate the efficiency of the selected optimal sensor sets using the simulated annealing algorithm, six damage patterns generated from the benchmark model, taken from Ref. [34] and summarized in Table 4.3, are considered. Each test case is repeated forty times with different realization of measurement noise and the average of each test case is further investigated. In addition, the Hotelling $T^2$ multivariate control chart [50] for monitoring the mean vector of the process is used. The out-of-control average run length ($ARL_1$), which is the number of observations needed until the change is detected, was investigated for the sensor configuration of the benchmark structure before and after the optimization. The results of the comparison using $ARL_1$ as a performance measure are summarized in Table 4.6.

**Table 4.6** $ARL_1$ results for the sensor configuration of the benchmark structure using Hotelling $T^2$ control charts for all six different damage patterns

| **Operating condition** | **$ARL_1$ (before optimization)** | **$ARL_1$ (after optimization))** |
|---|---|---|
| Very slight damage<br>Patterns 6 and 3 | P 6: $ARL_1$= 10.6<br>P 3: $ARL_1$= 5.2 | P 6: $ARL_1$= 6.2<br>P 3: $ARL_1$= 3.1 |
| Medium local damage<br>Patterns 4 and 5 | P 4: $ARL_1$= 2.6<br>P 5: $ARL_1$= 2.5 | P 4: $ARL_1$= 2.3<br>P 5: $ARL_1$= 2.0 |
| Severe damage<br>Patterns 1 and 2 | P 1: $ARL_1$= 1.0<br>P 2: $ARL_1$= 1.0 | P 1: $ARL_1$= 1.0<br>P 2: $ARL_1$= 1.0 |

From Table 4.6, we noticed that, the Hotelling $T^2$ control chart after optimization has shorter $ARL_1$ than that before optimization except for the severe damage cases (patterns 1 and 2); in other words, the Hotelling $T^2$ control chart captures the damage earlier using the optimized sensor locations.

Based on reported percentage loss in stiffness associated to each damage pattern shown in Table 4.7 [34], the power of damage detection occurred in the benchmark structure using the proposed SPO methodology can be quantified.

**Table 4.7** Percent loss in stiffness associated to different damage patterns for the benchmark structure

| **Damage patterns** | **$D_0$** | **$D_1$** | **$D_2$** | **$D_3$** | **$D_4$** | **$D_5$** | **$D_6$** |
|---|---|---|---|---|---|---|---|
| Percent loss in stiffness (Johnson et al., 2004) | N/A | 30% | 60% | 5.6% | 10.2% | 11.3% | 2.3% |

From Table 4.7, the proposed SPO methodology using the simulated annealing algorithm has the capability to differentiate between operating conditions with different levels of damage. In fact, the optimal sensor configuration has improved the detection performance in capturing all different levels of percent loss in structural stiffness, especially, the operating conditions with slight damage.

### 4.8 Summary

In this chapter, a PDE analytical model to predict the horizontal dynamic response of the four-story building when subjected to horizontal forced excitations is formulated and solved. The proposed PDE model has been validated with relation to experimental results using correlation analysis. The dynamic characteristics of the benchmark structure are approximated using the proposed PDE model. Moreover, a stochastic random field of the building vibration was formulated by expanding the suitable displacement functions as truncated series in *x* and *y* directions. Closed form solutions for mode shapes and acceleration of the benchmark structure corresponding to the *i*-th mode were obtained.

An optimal sensor placement method based on FIM was developed to the benchmark problem, in which the uncertainty in the estimated parameters was minimized. Results of the test benchmark case study indicated: 1) the proposed method based on the simulated annealing algorithm is effective in determining the optimal sensor locations; 2) it also illustrated that in damage detection applications, the optimized sensor locations result in an improved capability for damage detection.

# REFERENCES

1. Guo, H., et al., *Optimal placement of sensors for structural health monitoring using improved genetic algorithms.* Smart Materials and Structures, 2004. **13**(3): p. 528.

2. Hwang, S.-F. and R.-S. He, *A hybrid real-parameter genetic algorithm for function optimization.* Advanced Engineering Informatics, 2006. **20**(1): p. 7-21.

3. Zhao, R. and W. Tang, *Monkey algorithm for global numerical optimization.* Journal of Uncertain Systems, 2008. **2**(3): p. 165-176.

4. Pukelsheim, F., *Optimal design of experiments*. Vol. 50. 2006: Society for Industrial Mathematics.

5. Cox, D.R. and N. Reid, *The theory of the design of experiments*. Vol. 86. 2000: Chapman & Hall/CRC.

6. Fedorov, V.V. and P. Hackl, *Model-oriented design of experiments*. Vol. 125. 1997: Springer Verlag.

7. Qureshi, Z., T. Ng, and G. Goodwin, *Optimum experimental design for identification of distributed parameter systems.* International Journal of Control, 1980. **31**(1): p. 21-29.

8. Ucinski, D., *Optimal measurement methods for distributed parameter system identification*. 2004: CRC.

9. Kirkegaard, P.H. and R. Brincker, *On the optimal location of sensors for parametric identification of linear structural systems.* Mechanical Systems and Signal Processing, 1994. **8**(6): p. 639-647.

10. Cherng, A.P., *Optimal sensor placement for modal parameter identification using signal subspace correlation techniques.* Mechanical Systems and Signal Processing, 2003. **17**(2): p. 361-378.

11. Green, K., *Optimal sensor placement for parameter identification*. 2006, Rice University.

12. Li, Q., et al., *Accurate estimation of the Fisher information matrix for the PET image reconstruction problem.* Medical Imaging, IEEE Transactions on, 2004. **23**(9): p. 1057-1064.

13. Fuqing, L. and Z. Lingmi, *Successive method for optimal placement of actuators and sensors.* Journal of Astronautics, 2000. **3**: p. 010.

14. Sohn, H., et al., *A review of structural health review of structural health monitoring literature 1996-2001*. 2002, Los Alamos National Laboratory.

15. Udwadia, F.E., *Methodology for optimum sensor locations for parameter identification in dynamic systems.* Journal of Engineering Mechanics, 1994. **120**(2): p. 368-390.

16. Mottershead, J. and M. Friswell, *Model updating in structural dynamics: a survey.* Journal of sound and vibration, 1993. **167**(2): p. 347-375.

17. Friswell, M. and J.E. Mottershead, *Finite element model updating in structural dynamics*. Vol. 38. 1995: Springer.

18. Wang, M., G. Heo, and D. Satpathi, *A health monitoring system for large structural systems.* Smart materials and structures, 1998. **7**(5): p. 606.

19. Said, W.M. and W.J. Staszewski. *Optimal sensor location for damage detection using mutual information*. in *International Conference on Adaptive Structures and Technologies*. 2001: Technomic Publishing Company.

20. Trendafilova, I., W. Heylen, and H. Van Brussel, *Measurement point selection in damage detection using the mutual information concept.* Smart materials and structures, 2001. **10**(3): p. 528.

21. Chang, F.-K., *Structural health monitoring 2000: proceedings of the 2nd international workshop on structural health monitoring, stanford university, Stanford, CA, September 8-10, 1999*. 1999: Technomic Publishing Company.

22. Schulz, M.J., et al. *Structural health monitoring using frequency response functions and sparse measurements*. in *Society for Experimental Mechanics, Inc, 16 th International Modal Analysis Conference.* 1998.

23. Papadimitriou, C., Y. Haralampidis, and K. Sobczyk, *Optimal experimental design in stochastic structural dynamics.* Probabilistic engineering mechanics, 2005. **20**(1): p. 67-78.

24. Valle, C. and J.W. Littles Jr, *Flaw localization using the reassigned spectrogram on laser-generated and detected Lamb modes.* Ultrasonics, 2002. **39**(8): p. 535-542.

25. Ihn, J.B. and F.K. Chang, *Detection and monitoring of hidden fatigue crack growth using a built-in piezoelectric sensor/actuator network: I. Diagnostics.* Smart Materials and Structures, 2004. **13**(3): p. 609.

26. Wouwer, A.V. and M. Zeitz, *State estimation in distributed parameter systems.* Control Systems, Robotics and Automation, Theme in Encyclopedia of Life Support Systems, 2001.

27. Chmielewski, D.J., T. Palmer, and V. Manousiouthakis, *On the theory of optimal sensor placement.* AIChE journal, 2002. **48**(5): p. 1001-1012.

28. Zhang, G., *Optimum sensor localization/selection in a diagnostic/prognostic architecture*. 2005.

29. Marquardt, D.W., *An algorithm for least-squares estimation of nonlinear parameters.* Journal of the Society for Industrial & Applied Mathematics, 1963. **11**(2): p. 431-441.

30. Zemmour, A.I., *The Hilbert-Huang transform for damage detection in plate structures*. 2006.

31. Chiang, L.H., E. Russell, and R.D. Braatz, *Fault detection and diagnosis in industrial systems*. 2001: Springer Verlag.

32. Pappa, R.S., G.H. James, and D.C. Zimmerman, *Autonomous modal identification of the space shuttle tail rudder.* Journal of Spacecraft and Rockets, 1998. **35**(2): p. 163-169.

33. Reinoso, E. and E. Miranda, *Estimation of floor acceleration demands in high-rise buildings during earthquakes.* The Structural Design of Tall and Special Buildings, 2005. **14**(2): p. 107-130.

34. Johnson, e., et al., *Phase I IASC-ASCE structural health monitoring benchmark problem using simulated data.* Journal of Engineering Mechanics, 2004. **130**(1): p. 3-15.

35. Task-group. *ASCE benchmark structure*. ASCE-SHM 2004 [cited 2012 May, 20th ]; Available from: http://wusceel.cive.wustl.edu/asce.shm/).

36. Johnson, E., et al., *Phase I IASC-ASCE structural health monitoring benchmark problem using simulated data.* Journal of engineering mechanics, 2003. **130**(1): p. 3-15.

37. Sohn, H., et al., *A review of structural health monitoring literature: 1996-2001*. 2004: Los Alamos National Laboratory Los Alamos, New Mexico.

38. Beards, C., *Structural vibration: analysis and damping*. 1996: Butterworth-Heinemann.

39. Coddington, E.A., *An introduction to ordinary differential equations*. 2012: Courier Dover Publications

40. White, L., *A reduced three-dimensional dynamic structural model for structural health assessment.* Applied mathematics and computation, 2006. **182**(1): p. 572-588.

41. Ewing, G.M., *Calculus of variations with applications*. 1985: Dover publications.

42. Miranda, E. and S. Taghavi, *Approximate floor acceleration demands in multistory buildings. I: Formulation.* Journal of structural engineering, 2005. **131**(2): p. 203-211.

43. Chopra, A.K., *Dynamics of structures: Theory and applications to earthquake engineering*. Vol. 2. 2001: Prentice Hall Saddle Rivere NY NY.

44. Miranda, E. and C.J. Reyes, *Approximate lateral drift demands in multistory buildings with nonuniform stiffness.* Journal of structural engineering, 2002. **128**(7): p. 840-849.

45. Allemang, R.J., *The modal assurance criterion–twenty years of use and abuse.* Sound and Vibration, 2003. **37**(8): p. 14-23.

46. Huang, W., Z. Kong, and A. Chennamaraju, *Robust design for fixture layout in multistation assembly systems using sequential space filling methods.* Journal of computing and information science in engineering, 2010. **10**(4).

47. Staszewski, W.J. and K. Worden. *Overview of optimal sensor location methods for damage detection*. in *SPIE's 8th Annual International Symposium on Smart Structures and Materials*. 2001: International Society for Optics and Photonics.

48. Marwala, T., *Finite-element-model updating using nelder–mead simplex and newton broyden–Fletcher–Goldfarb–Shanno Methods.* Finite-element-model Updating Using Computional Intelligence Techniques: Applications to Structural Dynamics, 2010: p. 25-47.

49. Pan, Q., *System identification of constructed civil engineering structures and uncertainty*. 2007, Citeseer.

50. Montgomery, D.C., *Introduction to statistical quality control*. 2007: John Wiley & Sons

51. Yun-Xin, W., *Sensitivity-based finite element model updating methods with application to electronic equipments*. 1999, Faculté Polytechnique de Mons, Belgium.

52. Fritzen, C. and S. Zhu, *Updating of finite element models by means of measured information.* Computers & Structures, 1991. **40**(2): p. 475-486.

53. Luber, W. and O. Sensburg. *Identification of errors and updating in analytical models using test data*. in *Proceedings-spie the international society for optical engineering*. 1995: Spie international society for optical.

54. Lieven, N. and D. Ewins. *Spatial correlation of mode shapes, the coordinate modal assurance criterion (COMAC)*. in *International Modal Analysis Conference*. 1988.

55. Johansson, A.T., T. Abrahamsson, and F. van Keulen. *Comparison of several error metrics for FE model updating*. in *Proceedings of the 25th International Modal Analysis Conference (IMAC-XXV), February 19-22, Orlando, Florida, USA*. 2007.

56. Wu, J. and Q. Li, *Structural parameter identification and damage detection for a steel structure using a two-stage finite element model updating method.* Journal of Constructional Steel Research, 2006. **62**(3): p. 231-239.

57. Nair, K.K., A.S. Kiremidjian, and K.H. Law, *Time series-based damage detection and localization algorithm with application to the ASCE benchmark structure.* Journal of Sound and Vibration, 2006. **291**(1): p. 349-368.

58. Dascotte, E., J. Strobbe, and H. Hua, *Sensitivity-based model updating using multllple types of simultaneous state variables.* 1995.

59. Kammer, D. and L. Yao, *Enhancement of on-orbit modal identification of large space structures through sensor placement.* Journal of Sound and Vibration, 1994. **171**(1): p. 119-139.

60. Lay, D.C., *Linear algebra and its applications.* Addison Wesley, Pearson Education, Inc, 2003.

61. Tong, K., N. Bakhary, and A. Kueh, *Optimal sensor placement for structural health monitoring using improved simulated annealing.*

62. Yang, J.N., et al., *An adaptive extended Kalman filter for structural damage identification.* Structural Control and Health Monitoring, 2006. **13**(4): p. 849-867.

63. Black, C. and C. Ventura. *Blind test on damage detection of a steel frame structure*. in *Society for Experimental Mechanics, Inc, 16 th International Modal Analysis Conference.* 1998.

64. Borguet, S. and O. Léonard, *The Fisher information matrix as a relevant tool for sensor selection in engine health monitoring.* International Journal of Rotating Machinery, 2008. **2008**.

# CHAPTER V

# DAMAGE DETECTION BASED ON QUASI-RECURSIVE CORRELATION DIMENSION ANALYSIS

The nonlinear and nonstationary nature of the sensor measurements representing structural damage brings a great challenge to structural health monitoring (SHM). In order to detect structural damages in their incipient stage, some features sensitive to the damages should be extracted from the sensor signal. The correlation dimension, which is an effective index to capture the process dynamics, has a promising potential to play such a role. However, the traditional algorithms for computing the correlation dimension have fairly high complexity $O(N^2)$ and thus are not suitable for online monitoring. To tackle this challenge, this study presents a novel quasi-recursive correlation dimension algorithm (QRCD) for online detection of structural damages. The algorithm can significantly alleviate the complexity of computation for correlation dimension to approximate O(N), making the online monitoring of nonlinear/nonstationary processes using correlation dimension much more applicable and efficient.

## 5.1 Introduction and motivation

Many structures' damages occur in localized areas and exhibit a nonlinear and nonstationary dynamic behavior, bringing a great challenge to SHM. Since damage changes the physical parameters (mass, stiffness, damping, etc.) of the structures, model-based methods which depend on the model parameters (for example, natural frequency, mode shape, and modal damping), have been widely used for damage detection [1]. For large structures like bridges, damage may cause a very small change in natural frequency which is difficult to detect [2]. According to Ref. [3], changes in the mode shapes of a structure can be a more sensitive model parameter than the natural frequency for detection of local damage. However, extracted mode shapes may be influenced by operational and environmental noise. Another drawback of using mode shapes with sensor data is that the accuracy of the damage detection may be affected by the number of sensors and the choice of sensor coordinates [4]. Pandey et al. [5] suggested to use model curvature, namely, the second spatial derivative of the mode shape, as an extracted feature for damage detection. However, mode shape curvatures are less reliable when used as damage detection in structures with multiple damage [6, 7].

Wavelet analysis is one of the fastest evolving signal processing tools in the domain of damage detection [8]. Researchers in the SHM domain have also applied wavelet analysis to identify the existence and location of the structural damage [9-12]. Naldi et al. [12] explored the use of wavelet coefficients to detect damage in structural components. They used the coefficients of the Daubechies wavelet to identify the damage in a beam that was characterized by linear isotropic hardening. Nair et al. [13, 14] developed a damage detection algorithm based on the energy using the Haar and Morlet wavelet transforms of the vibration signals. Bukkapatnam et al. [15] utilized a wavelet-based distortion energy, which is calculated for each of many resolution levels of a wavelet representation, to detect both the existence and the location of damage in a structure. Park et al. [9] presented a method to find the minimum number of wavelet coefficients relevant to structural damages. However, according to Ref. [16], most of the recent applications of wavelet analysis are limited to linear dynamics. Moreover, the intrinsic physical property of the original signal could be highly affected by the selected mother wavelet [17]. That is, wavelet analysis method is non-adaptive because the same mother wavelet has to be used for all signal data.

An effective technique in studying nonlinear and nonstationary dynamic systems by characterizing sensor signals is needed for SHM. One of the effective methodologies to capture system dynamics is the correlation dimension [18]. It has noticeable advantages over many other types of exponent dimensions due to its relatively simple and fast calculation. It has a consistent estimation and a high sensitivity to the dynamic change [19]. The value of the correlation dimension has an important practical implication: the next highest integer above the correlation dimension describes the level of complexity of the underlying system, by representing the minimum number of degrees of freedom needed to model the system [20].

Although correlation dimension has the promising properties to characterize system dynamics, the existing algorithms for computing the correlation dimension have fairly high complexity and thus are not suitable for online monitoring. To tackle this challenge, this study presents a quasi-recursive correlation dimension algorithm (QRCD) for online damage detection of structures using an overlapping segmentation technique. It can significantly alleviate the complexity of computation for correlation dimension, and thus make the online monitoring of nonlinear/nonstationary processes using correlation dimension much more applicable and efficient.

## 5.2 Review of related research in correlation dimension analysis

In this section, a brief review of the related research is presented. It can be classified into two categories, namely, applications of correlation dimension (section 5.2.1) and algorithms for computing correlation dimension (section 5.2.2).

### 5.2.1 Related research in application of correlation dimension

Due to the fact that the existence of damage changes the physical parameters (mass, stiffness and damping) of structures, model-based methods which depend on the model parameters (natural frequency, mode shape and modal damping) are widely used for damage detection of structures [1]. However, these model-based methods have some limitations such as insensitivity to very small local damage [2], and are influenced by operational and environmental noise [3]. The accuracy of the damage detection system is affected by the total number of sensors adopted and the choice of sensor location [1]. Moreover, the model-based methods are less reliable when used in structures with multiple damage [7].

Logan and Mathew [21] applied the correlation dimension in the fault diagnosis applications. Their studies demonstrated that the correlation dimension is an effective approach in classifying three major rolling element-bearing faults. The work reported by Jiang *et al.* in Ref. [22] applied correlation dimension to gearbox fault diagnosis, and showed the capability of the correlation dimension in identifying industrial gearbox defects. It was found that the value of the correlation dimension decreases when a gearbox becomes cracked or has a broken tooth.

The applicability of correlation dimension using Grassberger-Procaccia (G-P) algorithm in large rotating machinery is reported in Ref. [7, 23]. This investigation indicates that the correlation dimension is effective in differentiating kinematic mechanisms. Koizumi et al. [24] employed the modified G-P algorithm [25] to investigate the chattering vibration during the cutting process. The correlation dimension shows its effectiveness as a diagnostic parameter for neural changes which occur in glaucoma [26]. In addition, the correlation dimension can differentiate between healthy brain states and those with schizophrenia or brain tumors [27].

Most of the work with applications of correlation dimension using G-P algorithm has been reported in the areas of machinery condition monitoring and fault diagnosis domains, but not in the field of SHM. In this chapter, a unique approach to computing correlation dimension called quasi-recursive correlation dimension (QRCD) is proposed for online damage detection of structures.

### 5.2.2 Related research in algorithms for computing correlation dimension

The standard G-P algorithm of correlation dimension computes the correlation sum for various radii $r_i$. The computational complexity of the G-P method is $\mathrm{O}(N^2 . m_{max} . n_{ri})$ , where $N$ is the length of the time series, $m_{max}$ is the maximum number of embedding dimensions and $n_{ri}$ is the number of different radii $r_i$. One possible approach to reduce the high complexity is to estimate the correlation sum from a subgroup $M$ of the actual sample size $N$, which reduces the complexity to $O(N.M.m_{max}.n_{ri})$ [28].

Another approach to reduce the high complexity is called the box-assisted correlation algorithm [29]. Under specific conditions, it uses only a small number of points that are in the same or in adjacent boxes called reference points and dramatically reduces the computational complexity to $O(N.\log N.m_{max}.n_{ri})$. However, Theiler [30] pointed out that such reference points should be as many as the number of points in the original data set. Although the complexity is reduced, it is at the expense of highly increased computational uncertainty, which then reduces the accuracy of the correlation dimensions [31, 32]. Moreover, the box-assisted correlation algorithm has relatively high statistical error and thus is not suitable for embedding dimensions greater than or equal to $0.75\ln(N)$ [29].

A method using a Theiler window as a threshold for radius $r$ was introduced in Ref. [19]. It reduces the computational complexity to $O(N^2.m_{max}.C(r_i))$, where $C(r_i)$ is a very small value $(\ll 1)$ because $D_2$ defined for small $r_i$, that is, the correlation sum value is needed only for small $r_i$. This method achieves both a high rate of accuracy and a reduced computational complexity. According to Theiler's algorithm [19], the correlation sum is calculated for a bounded range of $r$. So, it blows up for noisy signals [33]. That means for each new embedding dimension, noise effect predominates and as a result, the signal behaves randomly.

An efficient algorithm which computes the Gaussian kernel correlation integral (GKA) from noisy time series was reported by Yu *et al.* [34]. The GKA was used to estimate the underlying correlation dimension. It reduced the computational complexity to $O\left((N^2+{n_{ri}}^2).m_{max}\right)$. The GKA works for not only Gaussian noise, but also other types of noise provided that the noise level is relatively low (below15% of the signal content). On the other hand, it is not suitable for very long time series ($N > 10^5$) [34] since the algorithm for calculating the correlation sum is still $O\left(N \times N_{ref}\right)$, where $N_{ref}$ is a set of reference points randomly chosen on the attractor, which increases rapidly with increasing the length of the time series. Table 5.1 summarizes the aforementioned methodologies in computing correlation dimension.

**Table 5.1** Comparison of algorithms for computing the correlation dimension (NSR: noise-signal ratio)

| **Algorithm** | **Computational complexity** | **Accuracy and handling noise** |
|---|---|---|
| **G-P**<br>**(**Grassberger et al.,1983**)** | $O(N^2.m_{max}.n_{ri})$ | • Accurate with huge sample size<br>• Applicable to a very low Gaussian noise NSR = 2 % |
| **The box-assisted correlation**<br>**(**Theiler, 1987**)** | $O(N.\log N\,.m_{max}.n_{ri})$ | • Low accuracy (high statistical error)<br>• Not suitable for embedding dimension greater than $0.75\ \ln \mathrm{N}$ |
| **Theiler**<br>**(**Theiler, 1990**)** | $O(N^2.m_{max}.C(r_i))$ | • Large error for noisy signals |
| **GKA**<br>**(**Yu et al., 2000**)** | $O\big((N^2+{n_{ri}}^2).m_{max}\big)$ | • Applicable to different types of noise up to NSR = 20%<br>• Not suitable for long time series; $N > \ 10^5$ |

## 5.3 State space reconstruction for time series sensor signal

To understand the state space reconstruction technique, we need to understand the concepts of state space, attractor, evolution function and trajectory. For simplicity, we avoided the mathematical definition of these fundamental concepts and here’s a brief review of these definitions taken from Ref. [20].

**State space:** An abstract mathematical space in which coordinates represent the variables needed to specify the state of a dynamical system at any time.

**Attractor:** The state space point or set of points representing various possible steady-state conditions of a system; in other words, an equilibrium state or group of states to which a dynamical system converges.

**Trajectory:** A list of successive states of a dynamical system.

**Evolution function:** a fixed rule that describes what future states follow from the current state within the dynamical system.

From the previous definitions, *an attractor* is the invariant subset of state- space point or set of points representing the various possible steady-state conditions of a dynamical system. And the *trajectory* is the subsequent motion visualized through the state-space. For most dynamic systems, the evolution function is not available. An alternative approach to characterize the dynamic system in its state space is by studying its *attractor*. Figure 5.1 shows the well-known reference trajectories of the Lorenz attractor [35].

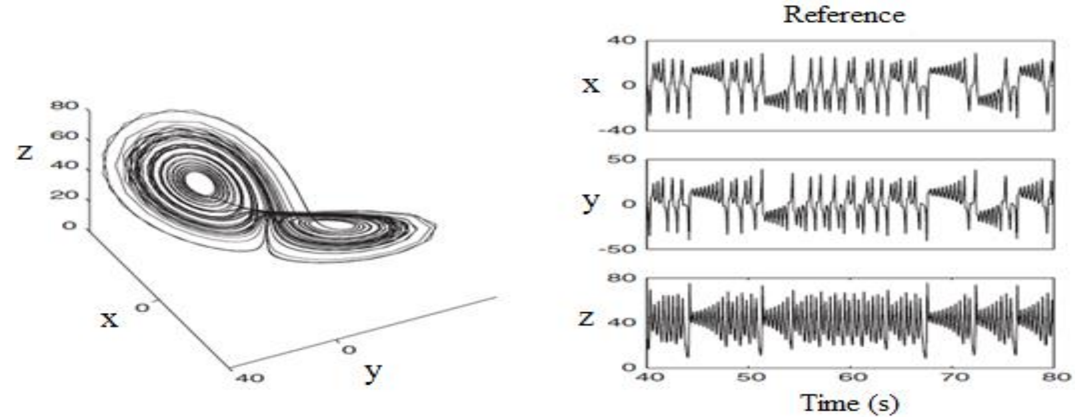

**Figure 5.1** Reference trajectories of the Lorenz attractor. 3D trajectory (left) along with 1 D time series for the same signal (right) [35]

Having only one access to the system's state variables is almost a challenge to infer useful information about the underlying system [36]. The technique of state-space reconstruction requires time series measurements of a single variable from which to specify the instantaneous state of the dynamical system [20]. Also, for low-dimensional systems, the state space reconstruction provides a representation of the steady-state dynamics of the underlying system. Moreover, it helps distinguish highly deterministic data from random data [20, 37].

In our proposed method, a state space analysis of time series sensor signal is the first step in computing correlation dimension. It utilizes the attractor reconstruction to re-create the full dimensional phase space for a single raw time series measurement [38], by embedding the time series into a higher dimensional state space along with a time-delay procedure.

The optimal time delay is chosen as the first minimum of the ‘mutual information function [20], while the minimum embedding dimension is chosen using the “false nearest neighbors” method [39]. According to Takens [40], taking delayed versions of the time series sensor signal $x = x_{n,\ n=1,2,\ldots N}$ and embedding them in an *m*-dimensional Euclidean space, the state space vectors can be constructed as

$$X_n = \left[x_{n-(m-1)\tau} \ \ \cdots \ \ x_{n-\tau} \ \ x_n\right] \tag{5.1}$$

where $n$ is a time index, $N$ is the number of observations, $\tau$ is the time delay and $m$ is the embedding dimension.

## 5.4 Proposed quasi-recursive correlation dimension analysis

In this section, the standard Grassberger-Procaccia (G-P) algorithm to estimate the correlation dimension is introduced first (section 5.4.1). On the top of it, a novel quasi-recursive correlation dimension (QRCD) algorithm using the chord estimator is presented (section 5.4.2). The proposed method not only significantly alleviates the computational complexity of correlation dimension, but also reduces the cost for basic computational operation (distance measure), thus making the online monitoring of nonlinear/ nonstationary processes using correlation dimension much more applicable and efficient.

### 5.4.1 Standard G-P correlation dimension analysis

The correlation dimension can be defined as,

$$D_2 = \frac{\partial \log(C(r,m))}{\partial \log(r)} = \lim_{r\to 0}(\log C(r,m) \,/\, \log r) \tag{5.2}$$

It can be seen from Equation (5.2) that the correlation dimension is the slope of the linear scaling region, which is a straight-line relation on a plot of the logarithm of correlation sum versus the logarithm of the measuring radius [33, 41].

*Advantages of the correlation dimension for process change detection*

In state-space modeling, a trajectory on a chaotic attractor may visit some parts on the attractor more often than others. Also, a trajectory can move at various directions. From Equation (5.2), it can be seen that the correlation dimension is a function of the measuring radius and the embedding dimension over the total number of available points; that is, the correlation dimension consider not only the geometry of the attractor (its size and shape), but also the probabilistic aspects of the trajectories [20]. Thus, the correlation dimension has a high sensitivity to dynamical changes; and, for a given dataset, it explores the attractor to a much finer scale than other exponent dimensions [20]. Moreover, the value of the correlation dimension has an important practical implication: the next highest integer value above the correlation dimension describes the level of complexity of the underlying dynamic system by representing the minimum number of active degrees of freedom needed to model the system [20]

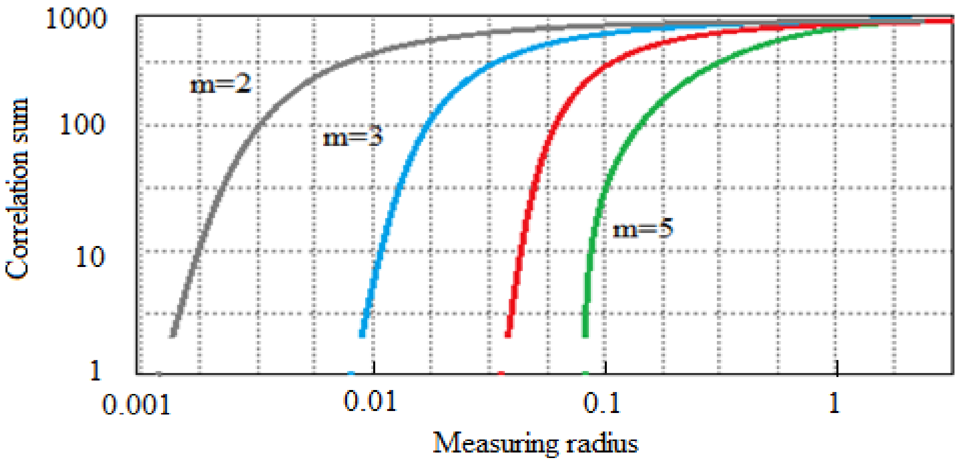

**Figure 5.2** The correlation sum as a function of measuring radius. (*m* represents embedding dimension)

Estimating the correlation dimension of the reconstructed attractor begins with plotting the correlation sum $C(r, m)$ versus radius $(r)$ on a log coordinate. The estimated correlation dimension will be the slope of the linear scaling region using the least–squares linear regression of log $C(r, m)$ versus log $r$ as illustrated in Figure 5.2. As the embedding dimension increases, the estimated correlation dimension also increases until it reaches a plateau as illustrated in Figure 5.3. The plateaued dimension value gives an estimate of the actual correlation dimension of the underlying chaotic attractor [20, 38, 42].

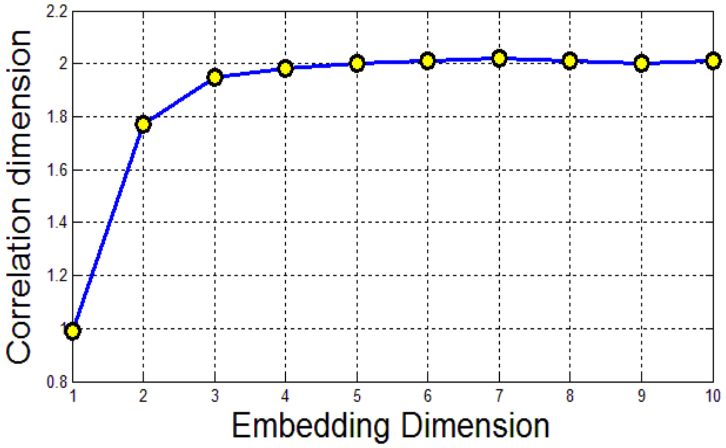

**Figure 5.3** Relationship between correlation dimension and embedding dimension

The standard G-P correlation dimension algorithm requires a large sample size, especially at small radii. Otherwise, insufficient sample size will cause an inaccurate estimation of the correlation dimension. The required sample size is application dependent [43-45]. In practice, a reliable estimation of the correlation dimension should rely on the estimation for several embedding dimensions and for different radii, thus the computational complexity will be of O $(N^2.m_{max}.n_{ri})$ [20, 23, 25, 43, 44, 46]. Thus, Equation (5.2) requires the computation of Euclidean distances between a large set of points, and the number of points needed increases in an exponential way with the value of $D_2$ [41].

### 5.4.2 The proposed quasi-recursive correlation dimension algorithm

According to the procedure of the standard G-P correlation dimension, its algorithm has a computational complexity of $O(N^2.m_{max}.n_{ri})$. Our proposed quasi-recursive correlation dimension computation will significantly reduce the computational complexity by computing all squared Euclidean distance in a recursive way between embedding dimensions (section 5.4.2.1) and within embedding dimensions using the overlapping segmentation techniques (section 5.4.2.2).

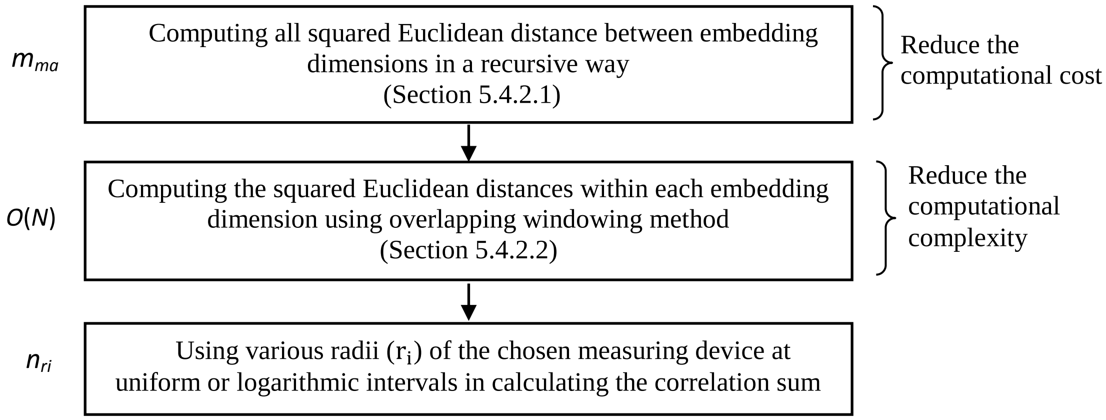

**Figure 5.4** The computational complexity of the proposed QRCD

An illustration of the computational complexity of the proposed quasi-recursive correlation dimension is given in Figure 5.4. The proposed quasi-recursive correlation dimension algorithm reduces the computational complexity to $O(\mathrm{N_w} \cdot m_{max} \cdot n_{ri})$, where $\mathrm{N_w}$ represents the length of the windowed signal. Thus, it makes the online monitoring of nonlinear/nonstationary processes using correlation dimension much more applicable and efficient. Moreover, as opposed to other correlation dimension algorithms [29, 32] , which used a subset of the whole data points, the proposed method fully utilizes the complete data set and adequately represents the attractor when embedded in several dimensions [47].

### 5.4.2.1 Recursive squared Euclidean distance between embedding dimensions

The correlation sum is calculated over all pairs of points. We present a lemma that shows the computation of the squared Euclidean distance between embedding dimensions in a recursive way, which consequently reduces the computation cost by eliminating the expensive Euclidean-norm operation to a great extent.

**Lemma 1:** For a given time series $\{x_{\mathrm{i}}\}$, i=1,…N. Let $\mathrm{N_w}$ be the length of the data points in windowed signal which is reconstructed in a space with embedding dimension $m$ and time delay

$\tau$. Also, let $a_{i,j}^{m,\tau}$ be the squared Euclidean distance between state vectors x(*i*) and x(*j*) in embedding dimension *m*, and $a_{i,j}^{m-1,\tau}$ be the squared Euclidean distance between state vectors x(*i*) and x(*j*) in embedding dimension *m*-1. Then the following recursive form with respect to embedding dimension holds:

$$a_{i,j}^{m,\tau} = a_{i,j}^{m-1,\tau} + [x(i + (m-1)\tau) - x(j + (m-1)\tau)]^2 \, , m \geq 1$$

**Proof:** Using Takens' time-delay embedding procedure and the following trajectory matrix compiled from the time-delayed signal vectors [38]

$$X = \begin{bmatrix} x_1 & x_{1+\tau} & \cdots & x_{1+(m-1)\tau} \\ x_2 & x_{2+\tau} & \cdots & x_{2+(m-1)\tau} \\ . & . & . & . \\ . & . & . & . \\ . & . & . & . \\ x_{N_w-(m-1)\tau} & x_{N_w-(m-2)\tau} & \cdots & x_{N_w} \end{bmatrix} \tag{5.3}$$

Each row in matrix *X* (Equation (5.3)) is in fact a state vector using state space reconstruction with embedding dimension of *m*, and delay of $\tau$, i.e.,

$$\vec{x}(i) = [x(i), x(i+\tau), \ldots x(i+(m-1)\tau)], \ \ i = 1, \ldots, N_w - (m-1)\tau$$

Thus, the distance between state vectors $\vec{x}(i)$ and $\vec{x}(j)$ can be computed as follows,

$$a_{i,j}^{m,\tau} = \sum_{k=0}^{m-1} [x(i + k\tau) - x(j + k\tau)]^2$$

$$= \sum_{k=0}^{m-2} [x(i + k\tau) - x(j + k\tau)]^2 + [x(i + (m-1)\tau) - x(j + (m-1)\tau)]^2 \tag{5.4}$$

The first part of the right hand side of Equation (5.4) is actually the distance between $\vec{x}(i)$ and $\vec{x}(j)$ in embedding dimension of (*m-1*) with lag $\tau$, i.e. $a_{i,j}^{m-1,\tau}$. Then Equation (5.4) can be expressed in recursive form by Equation (5.5) with respect to the embedding dimension

$$a_{i,j}^{m,\tau} = a_{i,j}^{m-1,\tau} + [x(i + (m-1)\tau) - x(j + (m-1)\tau)]^2 \tag{5.5}$$

Using Lemma 1, the computation cost will be reduced since the computation of distances is done only once for all the embedding dimensions. Moreover, the new components added to the recursive rule is just a basic addition operation for two floating point numbers obtained from the strictly upper triangular distance matrix of the raw scalar time series, instead of the repeated expensive operations in calculating Euclidean distance between points embedded in higher dimensions.

### 5.4.2.2 Computational complexity of correlation dimension with sliding windows

The proposed quasi-recursive correlation dimension algorithm can also reduce the computational complexity by computing the squared Euclidean distances within each embedding dimension using overlapping windowing technique (lemma 2). The overlapping window is implemented to not only reduce the computational complexity, but also localize the properties of the sensor signals. Thus, it makes the online monitoring of nonlinear/nonstationary processes using correlation dimension much more applicable and efficient. The principle of the overlapping segmentation technique is demonstrated in Figure 5, where $\mathrm{N_w}$ denotes the length of the windowed signal, and $\mathrm{x_{w_s}}$ and $\mathrm{N_{w_s}}$ refer to the sliding windowed signal points and sliding window length, respectively.

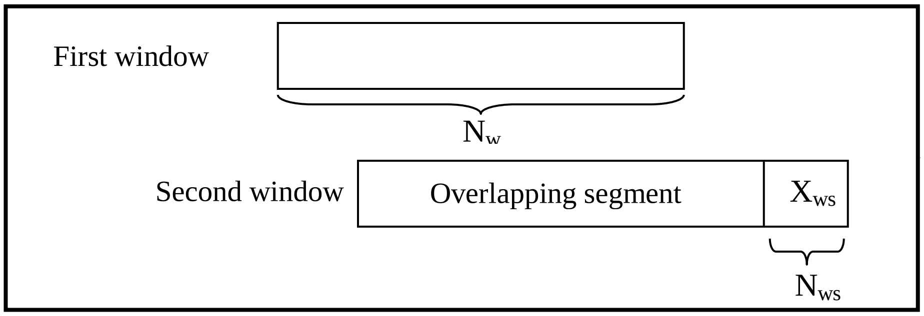

**Figure 5.5** Overlapping segmentation method

**Lemma 2**: Let $\{\mathrm{x_i}\}_{\mathrm{i=1}}^{\mathrm{N_s}}$ be a raw scalar time series, and $\mathrm{N_w}$ be the length of the data points in windowed signal which is reconstructed in a space with embedding dimension *m* and time delay

$\tau$. Also let the sliding windowed signal length $\mathrm{N}_{\mathrm{w}_\mathrm{s}}$ be far smaller than $\mathrm{N}_\mathrm{w}$. Then the computational complexity of the correlation dimension is $O(\mathrm{N}_\mathrm{w} \cdot m_{max} \cdot n_{ri})$.

**Proof:** Suppose $\mathrm{N}_\mathrm{w}$ and $\mathrm{N}_{\mathrm{w}_\mathrm{s}}$ are the length of the window and the sliding windowed signal length (see Figure. 5.5), respectively. Then the computational complexity for calculating the square Euclidean distance between all pairs in any chosen window is as follows,

$$O\left(\frac{1}{2}\left(\mathrm{N}_\mathrm{w}(\mathrm{N}_\mathrm{w}-1)\right)\right) \tag{5.6}$$

Now, by implementing the overlapping window shown in Figure 5.5, there is an overlapping segment $O_s = \mathrm{N}_\mathrm{w} - \mathrm{N}_{\mathrm{w}_\mathrm{s}}$. Consequently, Equation (5.6) will be

$$O\left[\frac{1}{2}\left(((\mathrm{N}_\mathrm{w})^2 - \mathrm{N}_\mathrm{w}) - \left(\left(\mathrm{N}_\mathrm{w} - \mathrm{N}_{\mathrm{w}_\mathrm{s}}\right)^2 - \left(\mathrm{N}_\mathrm{w} - \mathrm{N}_{\mathrm{w}_\mathrm{s}}\right)\right)\right)\right]$$

As long as $\mathrm{N}_{\mathrm{w}_\mathrm{s}} \ll \mathrm{N}_\mathrm{w}$, the computational complexity for calculating the square Euclidean distance between all pairs in any chosen window is $O(\mathrm{N}_\mathrm{w})$. Then, the overall computational complexity of the correlation dimension is $O(\mathrm{N}_\mathrm{w} \cdot m_{max} \cdot n_{ri})$. Q.E.D.

In order to estimate the correlation dimension accurately, the minimum window size is taken to satisfy the condition represented by $D_2 < 2\log(N)$, where $N$ is the window size [48], while the sliding window could be as small as one data point. That is because when the embedding dimension increases, the embedded time series length decreases as can be seen from Equation3 Thus, a small number of data points limit the total number of embedding dimensions that should be explored. That is, the attractor will not be fully reconstructed. [49]. Thus, a sufficient window size can avoid this issue.

### 5.4.3 Error analysis of the estimated correlation dimension

As discussed in Sec 5.4.1, the estimated correlation dimension is the slope of the linear scaling region using the least–squares linear regression of log *C(r, m)* versus log *r*. As the embedding dimension increases, the estimated correlation dimension also increases until it reaches a plateau (see Figure 5.2). The plateaued correlation dimension value gives an estimate of the actual correlation dimension of the underlying dynamic system. According to Theiler [50], there are two sources of errors in estimating correlation dimension from real data, namely, statistical error and systematic error as shown in Figure 5.6.

The estimated correlation dimension has a large statistical error when the correlation sum is computed for small radii ($r_i$) as illustrated in Figure 5.6. On the other hand, determining the correlation dimension for large radii ($r_i$) becomes difficult because of large systematical error caused by concaving of the log C(r,m) versus log(r) curve. This is due to the fact that, at large ($r_i$), the correlation sum will be dominated by saturation effects ($C(r, m) \to 1$), which happen when ($r_i$) becomes the size of the attractor. A tradeoff must be made for determining the range of radii ($r_i$) in order to have a robust estimation of correlation dimension.

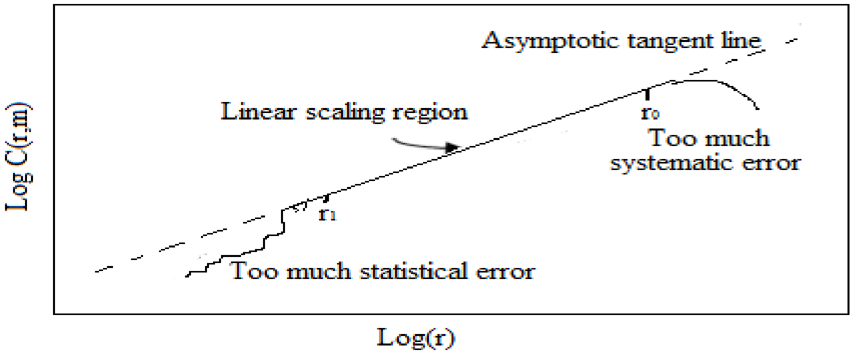

**Figure 5.6** Logarithm of the correlation sum (log C(r,m)) versus logarithm of the measuring radios ( log(r))

The effect of the total error involved in the correlation dimension estimation using the proposed method is minimized due to the following reasons: (1) the upper bound $r_0$ of the linear scaling region is chosen to be the Infimum of the set of all distances $r$, in which the correlation sum for each $r$ equal one; that is, $r_0 = inf\{r: C(r) = 1\}$, which reduces the effect of the systematical error; and (2) in order to minimize the effect of the statistical error, the proposed method takes the advantage of the optimal chord estimator [30] to determine the lower bound of the optimal linear scaling region. Assuming that the distances are independent and the power-law relation for the scaling region holds, that is, for some $r_0 > 0$ and $r \leq r_0$ , $C(r) = const \times r^{D2}$ [20], then the optimal choice of lower bound $r_1$ in the corresponding embedding dimension $m$ can be determined by the criterion as $\frac{C(r_0)}{C(r_1)} \approx 5$, [51], which minimizes the relative variance of the estimated correlation dimension. In other words, the upper and lower bound of the linear scaling region are chosen so that the ratio of their corresponding correlation sums is about five. The optimal chord estimator is the easiest and the fastest of all other estimators [52], and is used in this study to determine the lower bound of the optimal linear scaling region.

Third, the global structure of the reconstructed attractor is robust enough to the measurement noise that a trajectory still reflects global scaling [19]; but the correlation dimension is sensitive to the dynamical noise as demonstrated in section 5.5.2, case study two.

### 5.5 Case studies

In this section, four case studies are presented in sections 5.5.1 to 5.5.4, respectively, to illustrate the effectiveness of the proposed methodology. 1) In the first case study, three well-known test examples were taken from the literature: Hennon attractor, Lorenz attractor, and Van der pol Oscillator attractor [22, 53]. These examples are used to demonstrate the accuracy of correlation dimension computation using the proposed method as well as its computational efficiency. 2) The second case study uses simulation data generated by different ARMA models to test the sensitivity of the correlation dimension based EWMA and CUSUM control charts to process changes. 3) In the third case study, the numerically simulated datasets of the American Society of Civil Engineers' (ASCE) benchmark structure are used to test the sensitivity of correlation dimension for damage detection of the ASCE benchmark structure [54]. In section 5.5.4, the change of correlation dimension when damages occur is compared to loss in stiffness of the structures.

### 5.5.1 Case study 1: computational accuracy of the correlation dimension

To evaluate the computational accuracy of the correlation dimension using the proposed QRCD algorithm, three well known test examples were taken from the literature [22, 53], namely; Hennon attractor, Lorenz attractor and Van der pol oscillator attractor. For these three attractors, a comparison between the true value of the correlation dimension which were computed analytically in Ref. [22], and the estimated ones using our proposed QRCD algorithm as well as the standard G-P, is summarized in Table 5.2. Furthermore, the CPU time for these two types of estimation methods are compared and shown in Table 5.2.

The proposed algorithm significantly reduces the computational complexity in terms of CPU time by at least 60%, but still with a satisfying accuracy of the correlation dimension. In fact, the proposed algorithm has achieved a more accurate estimation of the true value of the correlation dimension over the standard G-P method. Moreover, a comparison of CPU time between the proposed method and the standard G-P method for Lorenz attractor is illustrated in Figure 5.7.

**Table 5.2** Computational results of quasi-recursive correlation dimension and standard correlation dimension algorithms for well-known test attractors

| **Signal model** (2000 points) | $\mathbf{D_2}$ Expressed analytically [22] | $\widetilde{\mathbf{D}}_2$ Estimated by standard G-P method | $\widetilde{\mathbf{D}}_2$ Estimated by proposed method | **CPU time (s)** Standard G-P method | | | **CPU time (s)** Proposed method | | |
|---|---|---|---|---|---|---|---|---|---|
| | | | | $m_{max}$ | | | $m_{max}$ | | |
| | | | | 10 | 20 | 30 | 10 | 20 | 30 |
| Lorenz | 2.02 | 2.09 | 2.07 | 34.24 | 152.13 | 421.34 | 0.40 | 0.44 | 0.49 |
| Henon | 1.26 | 1.28 | 1.25 | 34.08 | 138.96 | 361.02 | 0.31 | 0.35 | 0.41 |
| Van der pol | 1.00 | 1.08 | 1.05 | 34.41 | 156.81 | 429.79 | 0.42 | 0.52 | 0.65 |

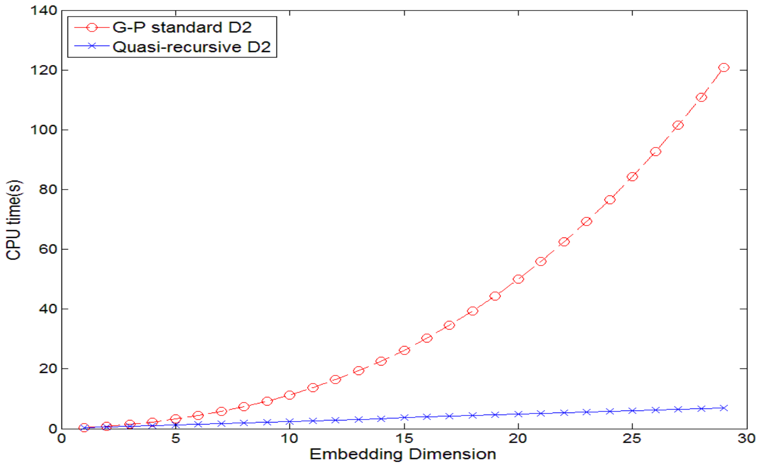

**Figure 5.7** Comparison of CPU time between the two versions of the correlation dimension for Lorenz Attractor

### 5.5.2 Case study 2: detection of process changes simulated using ARMA models

This case study demonstrates the effectiveness of the proposed method in detecting the process changes, which are simulated using time series ARIMA models. The performance of the proposed method is compared with the multi-scale monitoring scheme using wavelet decomposition reported by [55], which is able to detect the changes caused by not only mean shifts as the existing wavelet-based statistical process control methods [56-58], but also the variance change of the dynamic processes.

According to Guo et al. [55], the auto-correlated measurement data $y_t$, are generally modeled as,

$$y_t = x_t + e_t$$

$$x_t = \phi_1 x_{t-1} + \ \dots \phi_n x_{t-n} - \theta_1 a_{t-1} - \cdots \theta_m a_{t-m} + a_t$$

where, $a_t$ is the process noise, which is assumed to be independent of sensor noise $e_t$ as shown in the block diagram in Figure 5.8.

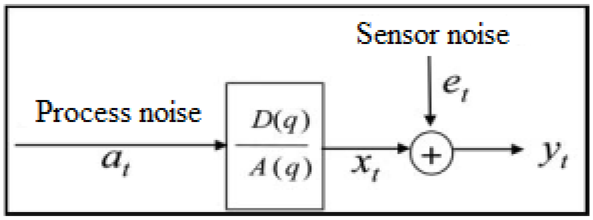

**Figure 5.8** Process model structure [55]

Under the normal process condition, $H_0: y_t \sim N(0, \sigma_a^2 + \sigma_e^2)$, where $\sigma_a^2$ is monitored to reflect the change of the process variance. For comparison purposes, we used the three faults tested [55], namely:

1) Mean shift of process noise: $H_1^1: a_t \sim N(\mu_a,\ \sigma_a^2)$
2) Variance change of process noise: $H_1^2: a_t \sim N(0, \delta_a^2\ \sigma_a^2)$
3) Variance change of measurement errors: $H_1^3: e_t \sim N(0, \delta_e^2\ \sigma_e^2)$

To illustrate the effectiveness of the proposed method for detecting the occurrence of process faults (mean shift and variance change of the process noise) and variance change of measurement errors, a higher order auto-correlated processes that have strong dynamic characteristics represented by ARMA (2, 1) is used (see Table 5.3). Each model is stable with *i.i.d.* Gaussian process noise and all their characteristic roots are within the unit circle [59].

**Table 5.3** ARMA (2, 1) models with different parameters [55]

| **Model** | **Parameters** | |
|---|---|---|
| | $A(q)$ | $D(q)$ |
| Model 1 | $1 - 0.99\,q^{-1} + 0.49\ q^{-2}$ | $1 - 0.7q^{-1}$ |
| Model 2 | $1 - 0.1\,q^{-1} + 0.8\ q^{-2}$ | $1 - 0.7q^{-1}$ |
| Model 3 | $1 - 0.6\,q^{-1} + 0.4\ q^{-2}$ | $1 - 0.7q^{-1}$ |

*Fault one (mean shift of process noise)*

For detecting mean shift of process noise, three different control charts are used: EWMA control charts using correlation dimension as the statistic to be monitored (denoted as CD-EWMA),the standard EWMA chart that directly monitors original signals (S-EWMA) and A wavelet-based EWMA chart using the optimal monitoring level of Haar wavelet coefficients (referred to as W-EWMA). More detailed information of multi-scale monitoring of auto-correlated processes using Haar wavelet analysis can be found in Ref. [55]. The control limits of EWMA charts are set up to make the in-control average run length ($\mathrm{ARL}_0$) approximately equal to 370 [55, 60]. The weighted factor (λ=0.2) is used as a reference for performance evaluation throughout this case study. To illustrate the effectiveness of the proposed method for detecting the mean shift of the process noise (fault one), it was assumed that, when the process is under control ($H_0$), the process noise follows the distribution of $N(0, 1)$. Assume under the fault condition one ($H_1^1\colon a_t \sim N(\mu_a,\ \sigma_a^2)$) that the process noise changed to three different normal distributions: $N(0.5, 1)$, $N(1, 1)$ and $N(1.5, 1)$, respectively, at observation $n$=651. The out-of-control average run length ($\mathrm{ARL}_1$), which is the number of observations needed until a shift is detected, was investigated for each model listed in Table 5.3. Each simulation is repeated 3000 times to ensure the accuracy of the $\mathrm{ARL}_1$. The performance of CD-EWMA, W-EWMA and S-EWMA in detecting mean shift of process noise was tested and shown in Figure 5.9.

The proposed CD-EWMA control charts have shorter ARL than W-EWMA control charts. In fact, the comparison indicates that the proposed scheme is more sensitive to the process noise mean shift than the W-EWMA control charts. Also, it consistently demonstrates a better detection power in detecting a noise small mean shift than the S- EWMA, which monitors the original signals.

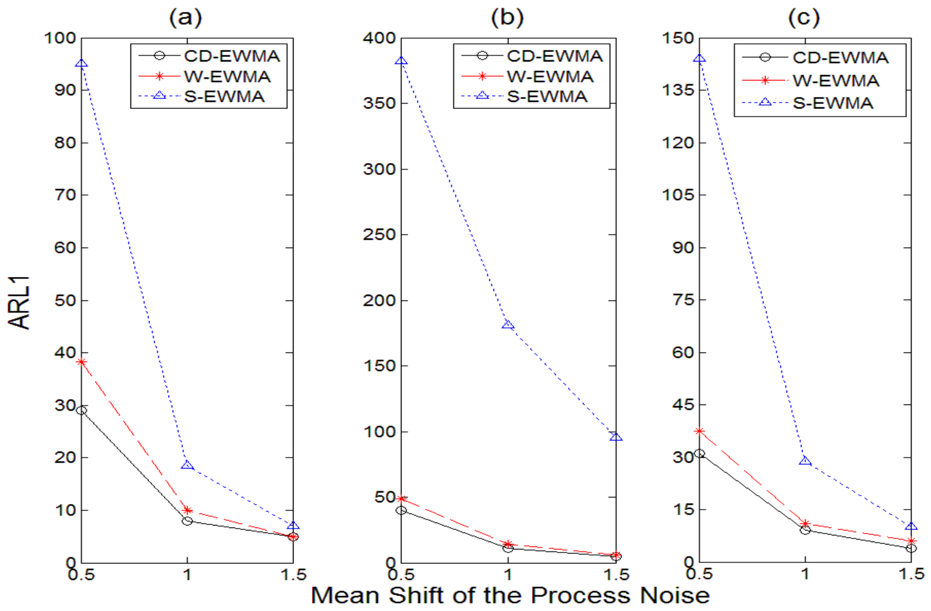

**Figure 5.9** $\mathrm{ARL}_1$ comparisons of CD-EWMA, W-EWMA and S-EWMA for detecting mean shift of the process noise for the three models mentioned in Table 3: (a) data generated by model 1, (b) data generated by model 2, (c) data generated by model 3

*Fault two* (*variance change of process noise*)

For detection variance change of the process noise, a quasi-recursive correlation dimension based CUSUM chart, denoted as CD-CUSUM; a wavelet based CUSUM chart, referred to as W-CUSUM; and a standard CUSUM chart, denoted as S-CUSUM are used. The control limits of CUSUM charts are designed to make the in-control average run length ($\mathrm{ARL}_0$) approximately equal to 370, in which the process noise follows the normal distribution with (0, 1) and $\lambda$=0.2 [55, 60]. Also, it is assumed that under the fault condition two ( $H_1^2: a_t{\sim}N(0, \delta_a^2\ \sigma_a^2)$ that the process noise changed to two different normal distributions: $N(0,\ 2^2)$ and $N(0,\ 3^2)$, respectively, at observation $n$=651. The out-of-control average run length ($\mathrm{ARL}_1$) was investigated for each model listed in Table 5.3. Each simulation has been replicated 3000 times to ensure the accuracy of the $\mathrm{ARL}_1$. Following the same procedure as in Ref. [55], the performance of CD-CUSUM, W-CUSUM and S-CUSUM in detecting the variance change of the process noise was tested, when the mean of the process noise is in-control, shown in Figure 5.10.

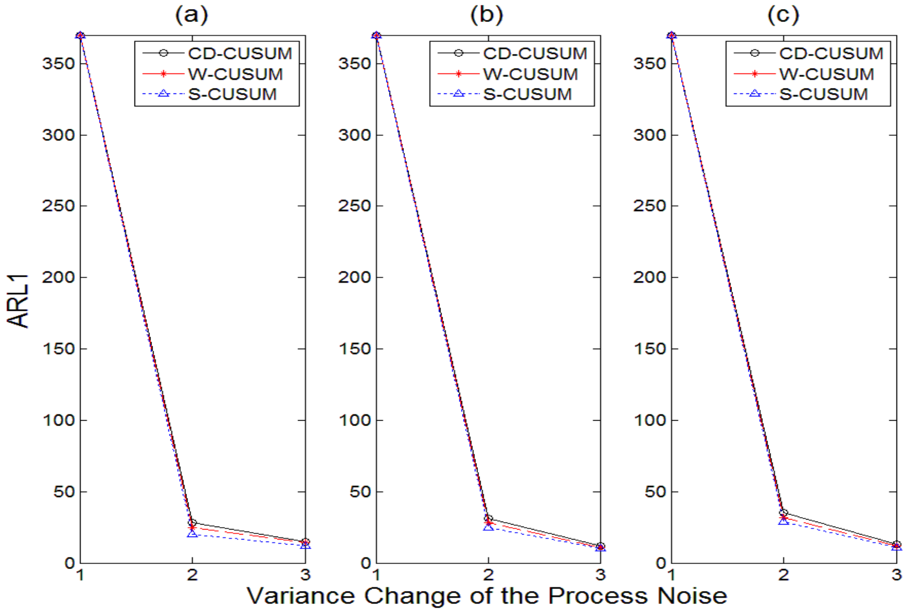

**Figure 5.10** ARL$_1$ comparison of CD-CUSUM, W-CUSUM and S-CUSUM in detecting variance change of the process noise with *N*(0,1) for the three models mentioned in Table 3: (a) data generated by model 1, (b) data generated by model 2, (c) data generated by model 3

The performance comparison of detecting the variance change of the process noise, as can be seen from Figure 5.10, shows that all three CUSUM charts have similar detection performance, with slightly smaller ARL$_1$ for S-CUSUM and W-CUSUM. In fact, the S-CUSUM chart has slightly smaller ARL$_1$ than both CD-CUSUM and W-CUSUM charts. However, taking into account robustness to a mean shift of the process noise, the W-CUSUM charts have a better detection performance than S-CUSUM [55, 60].

A further study is carried out when the process noise under the fault condition two ( $H_1^2: a_t \sim N(0, \delta_a^2\, \sigma_a^2)$) has changed from N(0,1.5$^2$) to three different normal distributions: *N*(0, $2^2$), *N*(0, $2.5^2$) and *N*(0, $3^2$), respectively, at observation *n*=651 The performance of CD-CUSUM, W-CUSUM and the S-CUSUM in detecting variance change of the process noise was tested and shown in Figure 5.11.

As illustrated in Figure 5.11, when the process noise changes from $N(0, 1.5^2)$, the proposed CD-CUSUM does outperform both the wavelet based CUSUM chart and the standard CUSUM chart, especially when the variance change of the process noise is increasing.

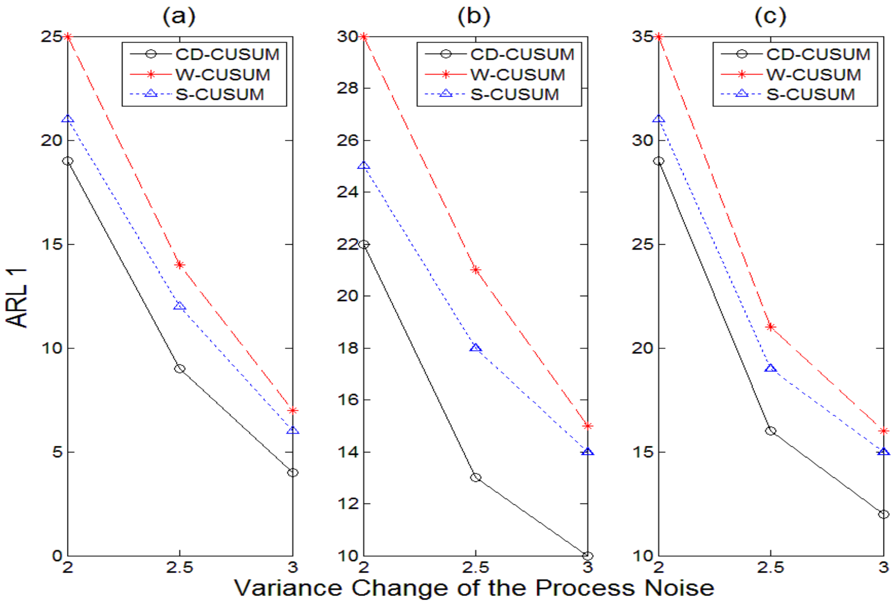

**Figure 5.11** $ARL_1$ comparison of CD-CUSUM, W-CUSUM and S-CUSUM in detecting variance change of the process noise with $N(0,1.5^2)$ for the three models mentioned in Table 3: (a) data generated by model 1, (b) data generated by model 2, (c) data generated by model 3

*Fault three* (*variance change of measurement errors*)

Following the work by Guo et al. [55], the performance of CD-CUSUM, W-CUSUM and S-CUSUM in detecting variance change of measurement errors was tested and shown in Figure 5.12.

It can be seen that the proposed CD-CUSUM chart takes a slightly longer detection delay than the W-EWMA, but it shows a better detection power in detecting variance change of measurement errors than the standard CUSUM.

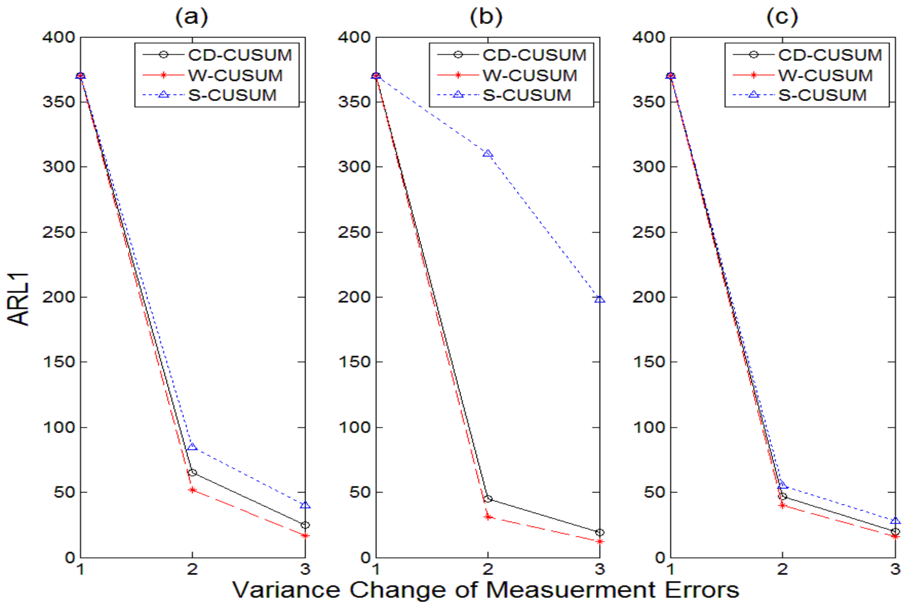

**Figure 5.12** ARL1 comparisons of CD-CUSUM, W-CUSUM and S-CUSUM in detecting variance change of measurement errors for the three models mentioned in Table: (a) data generated by model 1, (b) data generated by model 2, (c) data generated by model 3

The simulation results in this case study indicate that the proposed QRCD based EWMA and CUSUM control charts are sensitive to the mean shift and the variance change of the process noise. In fact, under certain conditions such as: high level of noise and when the process noise changes from $N(0, 1.5^2)$, it shows better detection performance not only over the standard EWMA and CUSUM charts, but also over the wavelet based EWMA and CUSUM charts.

### 5.5.3 Case study 3: damage detection for the ASCE benchmark structure

To validate the proposed method in detecting the occurrence of different damage patterns at relatively high levels of noise, the proposed method is applied to a benchmark study, which was designed by the American Society of Civil Engineers (ASCE) for the applicatoin of SHM [54]. The results of applying the proposed method in the benchmark study were compared with Morlet wavelet based damage feature, which is widely used in SHM due to its high sensitivity to very small damages [14]. The benchmark structure from which simulation data was taken consists of a 4-story and 2-bay by 2-bay steel frame structure as shown in Figure 5.13 [54].

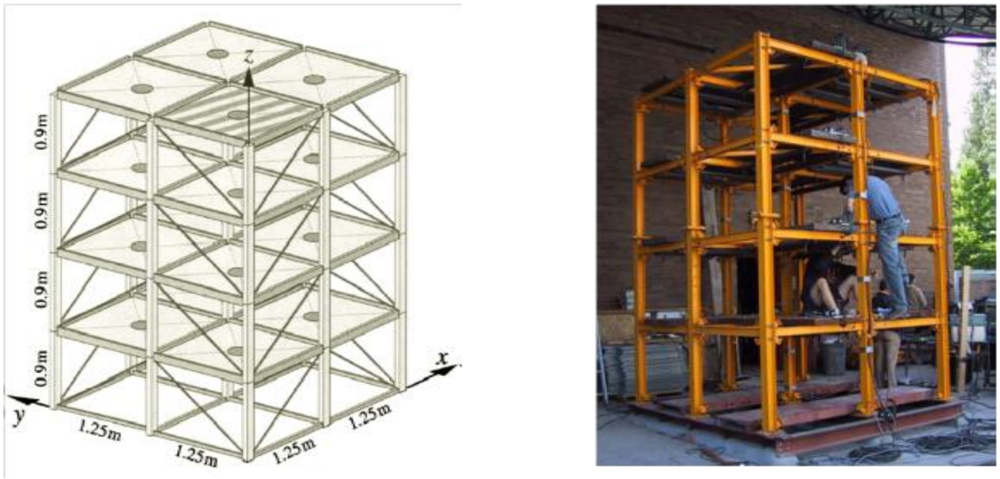

**Figure 5.13** Benchmark structure: Steel-frame structure (left) along with diagram of the analytical model (right) [54]

As illustrated in Figure 5.13, a bracing system placed along the diagonal was fixed for each bay. To emulate a real structure a concrete slab was built at each floor, and the removal of this bracing system is designed to simulate damage to the structure. For the experiment wind ambient excitation, two types of forced excitation sources were applied, namely, impact hammer test and electrodynamics shaker. A more detailed description of the bench mark structure problem can be found in the work by Johnson et al. [54]. A simulation program for generating the response of force sensor data in the ASCE benchmark structure is available at Ref. [61]. It is a MATLAB program based on 12- degrees of freedom (DOF) shear-building finite element model [54]. One undamaged case and six damage patterns generated from this benchmark model were used and are summarized in Table 5.4.

The detection performance of the QRCD algorithm has been tested by comparing the value of the average run length of the QRCD with that of the Wavelet analysis, which has been widely used to analyze nonstationary signals [17]. We set up the control limits of EWMA according to the in-control average run length ($ARL_0$), which is approximately equal to 370 with $\lambda=0.2$ [60]. Then two groups of EWMA control charts for both Morlet wavelet based damage feature [62] and QRCD-based damage feature $D_2$ for the six damage patterns in Table 5.4 were constructed. It is assumed that the process is under the in-control condition with case 0, which is an undamaged operating condition, and is changed to other cases at observation *n*=651. The results of the comparison using the average run length as a performance measure are summarized in Tables 5.5 and 5.6.

**Table 5.4** Damage patterns of the ASCE benchmark structure (12 DOF shear building)

| Damage pattern | Damage description |
|---|---|
| $D_0$: Damage pattern zero | No damage |
| $D_1$: Damage pattern one | Remove all braces in 1st floor. |
| $D_2$: Damage pattern two | Remove all braces in 1st and 3rd floor. |
| $D_3$: Damage pattern three | Remove a brace near sensor location 2 at 1st floor |
| $D_4$: Damage pattern four | Damage pattern 3 & remove a brace near sensor 9 at 3rd floor. |
| $D_5$: Damage pattern five | Damage pattern 4 & loosen floor beam near sensor 3 at 1st floor. |
| $D_6$: Damage pattern six | Remove 2/3 stiffness of a brace near sensor 2 at the 1st floor. |

**Table 5.5** Comparison results between QRCD and Morlet wavelet based EWMA control charts for the data with low level noise (NSR of 5%) for all six different damage patterns

| **Operating condition** | **$ARL_1$ (MWC)** | **$ARL_1$ (QRCD)** |
|---|---|---|
| Very slight damage<br>Patterns 6 and 3 | P 6: $ARL_1$= 16.4<br>P 3: $ARL_1$= 3.4 | P 6: $ARL_1$= 23.1<br>P 3: $ARL_1$= 5.2 |
| Medium local damage<br>Patterns 4 and 5 | P 4: $ARL_1$= 2<br>P 5: $ARL_1$= 2 | P 4: $ARL_1$= 2.5<br>P 5: $ARL_1$= 2.1 |
| Severe damage<br>Patterns 1 and 2 | P 1: $ARL_1$= 1.4<br>P 2: $ARL_1$= 1.4 | P 1: $ARL_1$= 1.4<br>P 2: $ARL_1$= 1.4 |

**Table 5.6** Comparison results between QRCD and Morlet wavelet based EWMA control charts for the data with high level noise (NSR of 20%) for all six different damage patterns

| **Operating condition** | **$ARL_1$ (MWC)** | **$ARL_1$ (QRCD)** |
|---|---|---|
| Very slight damage<br>Patterns 6 and 3 | P 6: $ARL_1$= 170<br>P 3: $ARL_1$= 150 | P 6: $ARL_1$= 101<br>P 3: $ARL_1$= 82.3 |
| Medium local damage<br>Patterns 4 and 5 | P 4: $ARL_1$= 23.1<br>P 5: $ARL_1$= 16.4 | P 4: $ARL_1$= 13.7<br>P 5: $ARL_1$= 10.2 |
| Severe damage<br>Patterns 1 and 2 | P 1: $ARL_1$= 3.5<br>P 2: $ARL_1$= 3.5 | P 1: $ARL_1$= 2.2<br>P 2: $ARL_1$= 2.2 |

From the comparison, we noticed that for noisy data with noise-signal ratio (NSR) up to 5%, the Morlet wavelet based damage feature $E_7$ has shorter $ARL_1$ than that of QRCD; in other words, it captures the damage earlier than the QRCD with small noise. For larger noise level, for example, the signals with NSR between 5% and 20%, which are typical of almost all practical situations [54], the QRCD has shorter $ARL_1$ than Morlet wavelet based method, which means QRCD is a more effective damage detection feature than the Morlet wavelet coefficients for a high level of noise, especially for small damage.

### 5.5.4 Case study 4: correlation dimension and stiffness of benchmark structure

For the purpose of determining the dynamical change of the underlying system, the proposed approach introduces a relative change indicator (RCI). It is based on the percentage change between the value of the QRCD computed for undamaged state and the damage state. The relative change indicator of the correlation dimension is defined as follows,

$$\mathrm{RCI} = \frac{\left|D_2^{new} - D_2^{old}\right|}{D_2^{old}} \times 100 \tag{5.7}$$

As the value of RCI increases, the dynamical change greatly increases. The RCI of the correlation dimension will be compared with the percent loss in stiffness of shear-building models.

In the 12-DOF shear-building finite element based model [54], the structural damage is clearly reflected in the change of its stiffness and mass matrices, where the columns and floor beams are modeled as Euler-Bernoulli and the braces are bars with no bending stiffness. Identically, the structural damage manifests itself physically in its dynamic properties such as the correlation dimension of the state of the state space attractor. Most of the structural damage algorithms depend on a comparison between the global stiffness matrix of the structure before and after damage [63]. The magnitude of damage is expressed as a percentage loss of stiffness, which is very critical in civil structural damage monitoring [64]. Therefore, to test the accuracy and sensitivity of the proposed damage quantification index, a comparison was conducted with the percent loss in stiffness matrices of the 12-DOF models, as shown in Table 5.7.

**Table 5.7** Comparison between the proposed relative change indicator and percent loss in stiffness of 12 degrees of freedom shear-building models

| Damage patterns | No damage | 1 | 2 | 3 | 4 | 5 | 6 |
|---|---|---|---|---|---|---|---|
| Average $D_2$ | 5.5 | 4.1 | 3.0 | 5.3 | 5.2 | 5.0 | 5.48 |
| RCI | N/A | 25.45% | 45.45% | 3.63% | 5.45% | 9.09% | 0.36% |
| Percent loss in stiffness [65] | N/A | 30% | 60% | 5.6% | 10.2% | 11.3% | 2.3% |

A noteworthy issue in using RCI as a damage quantification index is that it is very consistent to percent loss in stiffness as shown in Table 5.7. In fact, the comparison indicates that the RCI can accurately capture the percent loss in stiffness matrix of the structure, and thus effectively differentiate between operating condition with different levels of damage. Also, as the value of RCI increases, the severity of damage increases. Thus, it has the capability to correctly classify the different levels of damage as small damage (case 3 and case 6), medium damage (case 4 and case 5) and major damage (case 1 and case 2). Moreover, the proposed method not only captures the percent loss in stiffness matrices of structure, but also does not require the computation for the mass matrix of the structure, which makes the estimation of magnitude of damage much easier [63], [65, 66].

## 5.6 Summary

In this chapter, a novel QRCD analysis for online SHM has been developed. The proposed method adopts a recursive approach in the computation using overlapping quasi-recursive techniques. Thus, the online monitoring of sensor data using correlation dimension can be carried out in an efficient way. The simulation results indicate: 1) the superiority of the proposed method over the G-P standard correlation dimension algorithm by significantly reducing the computational complexity in terms of CPU time by at least 60% (for different levels of damage); 2) the proposed EWMA and CUSUM control charts are sensitive to the mean shift and the variance change of the process noise (occurrence of damages). The results also indicate that, under certain conditions (high level of noise and small damage), the proposed method shows a better detection performance not only over the standard EWMA and CUSUM charts, but also over the wavelet EWMA and CUSUM charts; 3) the developed methodology is less influenced by process noise compared to the wavelet analysis based approaches; and 4) it is also demonstrated that the proposed RCI based on the correlation dimension has the capability to capture the percent loss in stiffness of the structure, and thus effectively differentiate between operating condition with different levels of damage.

# REFERENCES

1. Montalvao, D., N. Maia, and A. Ribeiro, *A review of vibration-based structural health monitoring with special emphasis on composite materials.* Shock and Vibration Digest, 2006. **38**(4): p. 295-326.

2. Kim, J.T., et al., *Damage identification in beam-type structures: frequency-based method vs mode-shape-based method.* Engineering structures, 2003. **25**(1): p. 57-67.

3. Farrar, C.R. and D.A. Jauregui, *Comparative study of damage identification algorithms applied to a bridge: I. Experiment.* Smart Materials and Structures, 1998. **7**: p. 704.

4. Montalvao, N.M., A.Ribeiro, *A review of vibration-based structural health monitoring with special emphasis on composite materials.* Shock and Vibration Digest 2006. **38** (4): p. 295–324.

5. Pandey, A., M. Biswas, and M. Samman, *Damage detection from changes in curvature mode shapes.* Journal of sound and vibration, 1991. **145**(2): p. 321-332.

6. Ganguli, M.C.a.R., *Damage assessment of structures with uncertainty by using mode-shape curvatures and fuzzy logic.*

7. Chandrashekhar, M. and R. Ganguli, *Damage assessment of structures with uncertainty by using mode-shape curvatures and fuzzy logic.* Journal of sound and vibration, 2009. **326**(3): p. 939-957.

8. Sohn, H., et al., *A review of structural health monitoring literature: 1996-2001*. 2004: Los Alamos National Laboratory Los Alamos,, New Mexico.

9. Park, C., J. Tang, and Y. Ding, *Aggressive data reduction for damage detection in structural health monitoring.* Structural Health Monitoring, 2010. **9**(1): p. 59-74.

10. Tian, J., Z. Li, and X. Su, *Crack detection in beams by wavelet analysis of transient flexural waves.* Journal of sound and vibration, 2003. **261**(4): p. 715-727.

11. Basu, B., *Identification of stiffness degradation in structures using wavelet analysis.* Construction and building materials, 2005. **19**(9): p. 713-721.

12. Naldi, G. and P. Venini, *Postprocessing singular solutions by the wavelet transform.* structural damage assessment using advanced signal processing procedures, 1997: p. 109-120.

13. Nair, K. and A. Kiremidjian, *Damage detection using Haar wavelet transforms of vibration signals.* ASME Journal of Applied Mechanics, 2009. **76**: p. 061015-1.

14. Nair, K.K. and A.S. Kiremidjian, *A damage detection algorithm using the morlet wavelet transform.* ASCE Journal of Engineering Mechanics, in review., 2009.

15. Bukkapatnam, S., et al., *A wavelet-based, distortion energy approach to structural health monitoring.* Structural Health Monitoring, 2005. **4**(3): p. 247-258.

16. Staszewski, W., K. Worden, and G. Tomlinson, *Optimal sensor placement for neural network fault diagnosis.* Parmee and Denham [2396], page, 1996.

17. Shi, C. and Q. Luo, *Hilbert-Huang transform and wavelet analysis of time history signal.* Acta Seismologica Sinica, 2003. **16**(4): p. 422-429.

18. Moon, F.C., *Chaotic and fractal dynamics: an introduction for applied scientists and engineers*. Vol. 269. 1992: Wiley.

19. Theiler, J., *Estimating fractal dimension.* JOSA A, 1990. **7**(6): p. 1055-1073.

20. Williams, G.P., *Chaos Theory Tamed*. 1997, Washington D. C.: National Academy Press.

21. Logan, D. and J. Mathew, *Using the correlation dimension for vibration fault diagnosis of rolling element bearings—I. Basic concepts.* Mechanical Systems and Signal Processing, 1996. **10**(3): p. 241-250.

22. Jiang, J., J. Chen, and L. Qu, *The application of correlation dimension in gearbox condition monitoring.* Journal of Sound and Vibration, 1999. **223**(4): p. 529-541.

23. Wang, W., J. Chen, and Z. Wu, *The application of a correlation dimension in large rotating machinery fault diagnosis.* Proceedings of the Institution of Mechanical Engineers, Part C: Journal of Mechanical Engineering Science, 2000. **214**(7): p. 921-930.

24. Koizumi, T., N. Tsujiuchi, and Y. Matsumura, *Diagnosis with the correlation integral in time domain.* Mechanical Systems and Signal Processing, 2000. **14**(6): p. 1003-1010.

25. Wang, W., et al., *The application of some non-linear methods in rotating machinery fault diagnosis.* Mechanical Systems and Signal Processing, 2001. **15**(4): p. 697-705.

26. Schmeisser, E.T., *Fractal analysis of steady-state-flicker visual evoked potentials: Feasibility*. JOSA A, 1993. **10**(7): p. 1637-1641.

27. Kotini, A. and P. Anninos, *Detection of non-linearity in schizophrenic patients using magnetoencephalography*. Brain topography, 2002. **15**(2): p. 107-113.

28. Mayer-Kress, G., *Application of dimension algorithms to experimental chaos.* Directions in chaos, 1987. **1**: p. 122-135.

29. Theiler, J., *Efficient algorithm for estimating the correlation dimension from a set of discrete points.* Physical Review A, 1987. **36**(9): p. 4456-4462.

30. Theiler, J., *Statistical precision of dimension estimators.* Physical Review A, 1990. **41**(6): p. 3038-3051.

31. Holzfuss, J. and G. Mayer-Kress, *Dimensions and entropies in chaotic systems*. 1986, Springer-Verlag, Berlin.

32. Harikrishnan, K., R. Misra, and G. Ambika, *Revisiting the box counting algorithm for the correlation dimension analysis of hyperchaotic time series.* Communications in Nonlinear Science and Numerical Simulations, 2012. **17**: p. 263-276.

33. Grassberger, P., *An optimized box-assisted algorithm for fractal dimensions.* Physics Letters A, 1990. **148**(1-2): p. 63-68.

34. Yu, D., et al., *Efficient implementation of the Gaussian kernel algorithm in estimating invariants and noise level from noisy time series data.* Physical Review E, 2000. **61**(4): p. 3750.

35. Monbet, V. and P.F. Marteau, *Non parametric resampling for stationary Markov processes: The local grid bootstrap approach.* Journal of statistical planning and inference, 2006. **136**(10): p. 3319-3338.

36. Trendafilova, I. *A state space based approach to health monitoring of vibrating structures*. 2003: Trans Tech Publ.

37. Todd, M., et al., *Vibration-based damage assessment utilizing state space geometry changes: local attractor variance ratio.* Smart Materials and Structures, 2001. **10**: p. 1000-1008.

38. Kantz, H., T. Schreiber, and R.S. Mackay, *Nonlinear time series analysis*. Vol. 2000. 1997: Cambridge university press Cambridge.

39. Kennel, M.B., R. Brown, H.D.I. Abarbanel, *Determining embedding dimension for phase-space reconstruction using a geometrical construction.* Physical Review A. 1992. **45** (6): p. 3403-3411.

40. Takens, F., *Detecting strange attractors in turbulence*. In Dynamical Systems and Turbulence, ed. D.A.R.L.-S. Young. 1981, Berlin Springer. 366-81

41. Grassberger, P., T. Schreiber, and C. Schaffrath, *Nonlinear time sequence analysis.* International Journal of Bifurcation and Chaos, 1991. **1**(3): p. 521-547.

42. Grassberger, P. and I. Procaccia, *Measuring the strangeness of strange attractors.* Physica D: Nonlinear Phenomena, 1983. **9**(1-2): p. 189-208.

43. Nerenberg, M. and C. Essex, *Correlation dimension and systematic geometric effects.* Physical Review A, 1990. **42**(12): p. 7065-7074.

44. Essex, C. and M. Nerenberg, *Fractal dimension: Limit capacity or Hausdorff dimension?* American Journal of Physics, 1990. **58**: p. 986.

45. Schuster, H.G. and W. Just, *Deterministic chaos*. 1988: Wiley Online Library.

46. Smith, L.A., *Intrinsic limits on dimension calculations.* Physics Letters A, 1988. **133**(6): p. 283-288.

47. Main, I.G., *Damage mechanics with long-range interactions: correlation between the seismic b-value and the fractal two-point correlation dimension.* Geophysical Journal International, 1992. **111**(3): p. 531-541.

48. Eckmann, J.P. and D. Ruelle, *Fundamental limitations for estimating dimensions and Lyapunov exponents in dynamical systems.* Physica D: Nonlinear Phenomena, 1992. **56**(2-3): p. 185-187.

49. Jiang, W., *Time series analysis and correlation dimension estimation: mathematical foundation and applications*. 1995, Florida Atlantic University.

50. Theiler, J., *Spurious dimension from correlation algrothms applied to limited time-series data.* Physical Review A, 1986. **34**(3): p. 2427-32.

51. Theiler, J. and T. Lookman, *Statistical error in a chord estimator dimension.: the "rule of five".* International Journal of Bifurcation and Chaos, 1993. **3**: p. 765-771.

52. Theiler, J., Lookman, T. , *Statistical error in a chord estimator of correlation dimension: the rule of ve.* Int. J. Bifrucation and Chaos 1993. **3**: p. 765-771.

53. Rolo-Naranjo, A. and M.E. Montesino-Otero, *A method for the correlation dimension estimation for on-line condition monitoring of large rotating machinery.* Mechanical Systems and Signal Processing, 2005. **19**(5): p. 939-954.

54. Johnson, e., et al., *Phase I IASC-ASCE structural health monitoring benchmark problem using simulated data.* Journal of Engineering Mechanics, 2004. **130**(1): p. 3-15.

55. Guo, H., K. Paynabar, and J. Jin, *Multiscale monitoring of autocorrelated processes using wavelets analysis.* IIE Transactions, 2012. **44**(4): p. 312-326.

56. Chicken, E., J.J. Pignatiello Jr, and J.R. Simpson, *Statistical process monitoring of nonlinear profiles using wavelets.* Journal of Quality Technology, 2009. **41**(2): p. 198-212.

57. Jeong, M.K., J.C. Lu, and N. Wang, *Wavelet-based SPC procedure for complicated functional data.* International Journal of Production Research, 2006. **44**(4): p. 729-744.

58. Jin, J. and J. Shi, *Automatic feature extraction of waveform signals for in-process diagnostic performance improvement.* Journal of Intelligent Manufacturing, 2001. **12**(3): p. 257-268.

59. Pandit, S.M. and S.M. Wu, *Time series and system analysis with applications*. 1990, New York: RE Krieger Pub. Co.

60. Montgomery, D.C. and R. Gerth, *Introduction to statistical quality control.* IIE Transactions, 1998. **30**(6): p. 571.

61. Task-group. *ASCE benchmark structure*. ASCE-SHM 2004 [cited 2012 May, 20th ]; Available from: http://wusceel.cive.wustl.edu/asce.shm/). .

62. Nair, K.K. and A.S. Kiremidjian, *A damage detection algorithm using the morlet wavelet transform.* under review, 2009.

63. Galiote, M., J. Escobar, and R. Gómez. *Identification of stiffness loss as a measure of damage in buildings*. 2008: International Association for Earthquake Engineering.

64. Escobar, J.A., J.J. Sosa, and R. Gómez, *Structural damage detection using the transformation matrix.* Computers & structures, 2005. **83**(4): p. 357-368.

65. Reifsnider, K., *Damage in composite materials*. Vol. 775. 1982: Astm Intl.

66. Adams, D.E., *Health monitoring of structural materials and components.* Methods with Applications. Willey, New York, 2007.

# CHAPTER VI

# DAMAGE PREDICTION USING EMPIRICAL MODE DECOMPOSITION BASED ANALYSIS

To track structural integrity and ensure safe and reliable systems, an effective predictive modeling based change point detection to predict the severity of civil infrastructural damage is important. In this chapter, an online prediction method for analyzing the nonlinear and nonstationary signals based on local empirical mode decomposition and the locally weighted linear predictor is developed.

## 6.1 Introduction and motivation

To avoid catastrophic incidents, a prediction based change point detection to predict the severity of civil infrastructural damage is important to assist owners/operators of ageing infrastructure with timely information. Moreover, the majority of the literature for damage identification relies on finite element modeling process and/or linear modeling [1]. According to Sohn et al. [2], for practical applications, these techniques have not been shown to be effective in detecting damage at an early stage. For online SHM applications, the delay time has to be minimized and the computational cost has to be reduced. Thus, in this study, an effective online monitoring method for nonlinear and nonstationary signals based on local empirical mode decomposition is presented.

We proposed a local implementation of the standard empirical mode decomposition using a sliding window with flexible length, and thus the sifting operation is conducted by blocks. The proposed methodology enables the Hilbert Huang transform (HHT) to be used as an online analysis technique for streaming data [3]. In addition, the Hilbert instantaneous phase [4] is used for change point detection, while the damage prediction is investigated using the energy of the most representative intrinsic mode function (IMF) within the predicted window.

## 6.2 Review of related research in Hilbert Huang Transform

The Hilbert Huang Transform (HHT) has been recognized as one of the most important adaptive data analysis technique [5]. It can be used for damage detection and system identification [3, 6]. In particular, Tua et al. [7], used the energy peaks in the Hilbert spectrum associated to crack-reflected waves to determine accurate flight times as well as to estimate the orientation of the crack. In addition, according to Yang et al. [8], the EMD can be used to extract damage spikes caused by a sudden change. They also used both EMD and Hilbert transform to determine the damage time instants and natural frequencies of the structure before and after damage.

In this section, a review of the related research in HHT is presented. It can be classified into two categories, namely, boundary processing techniques for empirical mode decomposition (Sec. 6.2.1) and interpolation for EMD (Sec. 6.2.2).

### 6.2.1 Related research in boundary processing techniques for empirical mode decomposition

In application of EMD methods, there is an issue when spline interpolation is used to obtain the mean curve of the upper and lower envelopes of the underlying signal [9]. If the endpoints are not exactly the extreme points, then the decomposed signal will be distorted and this problem is called the “boundary effect” or the “boundary distortion “. The effect of the boundary distortion problem upon the decomposed signal depends on its time scales. According to Ref. [10], for high frequency components, only the neighborhood of the endpoints will be affected. On the other hand, for low frequency components, the boundary effect will be gradually propagated to influence the inner of the signal. Moreover, the more short the signal's length is, the more serious the boundary effect will be [11]. That is, during the sifting procedure, the decomposed IMFs from a short signal will lose the physical meaning.

To eliminate the "end effects", there are two main methods, which are widely used in signal processing literature. One technique is called the extended-based boundary processing method [9, 10, 12]. And the other one is called Cosine window-based boundary processing method [11, 13].

*The extended-based boundary processing method*

The extended-based boundary processing method includes different techniques to extend the signal, for example; even and odd characteristic wave extension [10, 12], neural network based technique , and "Mirrorisation" process [14].

In using even and odd characteristic wave extension method, the underlying signal is extended by adding three periods of characteristic sinusoidal wave, which has an amplitude and period matching the last wave within the data span [15]. This method reduces the end effects. However, Zeng et al. [12] pointed out that the signal has to be periodic, and thus deciding the characteristic period is hard, especially if the dependent scale varies with the starting and ending points. Moreover, the even extension technique forces the two end points to be extrema. Also, odd extension forces the mean of upper and lower envelopes to cross zero near the end points outside of the data span.

Another technique to extend the signal based on neural network was studied by Lee et al. [16] and by Deng et al. [17]. A method using back-propagation network [18] was introduced, which achieved relatively an accurate EMD. According to Deng et al. [17], choosing the appropriate neural network varies with different data sets. That means, for each data set, proper neural network extension arithmetic is needed. Hence, this method is not efficient for online monitoring.

Because the amount of work per sliding window is increased, there will be a performance penalty.

A mirrorisation process to reduce the end effects due to extrapolation was suggested by Rilling et al. [14]. This technique is carried out by taking a mirror-copy of the extrema, and then interpolating with both the mirrored and the original extrema. This method prevented the inclusion of the “end effects” in the computed IMF and residue. On the other hand, according to Ref.[19], the mirrorisation technique did not fully overcome the sharp discontinuities due to end effects, which corrupts the calculation of the next IMF. Moreover, the mirrorisation technique does not guarantee the lining up of envelopes for subsequent blocks. More details of the mirrorisation process is provided in Ref.[14].

### *Cosine window-based boundary processing method*

Another method to eliminate the “end effects” problem was called a cosine window, which is defined to have values equal to 1 in middle of the window while both ends were reduced by a cosine function [11]. The cosine window based processing method was applied in fault diagnosis of a machine set called heavy oil catalytic cracking unit [11]. It has been shown that the end effects can be controlled in boundaries of the underlying signal and the middle components of the signal can be exactly decomposed. But for short data set, removal of the influenced ends segments will cause missing of some important information during the EMD process [17]. That is, due to finite observation lengths, the error will propagate from previous IMF to later IMF. In addition, according to Parey et al. [13], the cosine window method is suitable for a particular frequency band depending on the size of the cosine window. Table 6.1 summarizes limitations of the aforementioned boundary processing techniques.

**Table 6.1** Comparison of main boundary processing techniques

| **Boundary Processing Technique** | **Limitations** |
|---|---|
| Cosine window<br>(Deng et al., 2001) | • Not suitable for short data sets.<br>• Suitable for only a particular frequency band depending on the size of the Cosine window. |
| Mirrorisation<br>(Rilling et al., 2003) | • Does not fully overcome the sharp discontinuities, which highly corrupts the calculation of the next IMF.<br>• Does not guarantee the lining up of envelopes for subsequent blocks. |
| Characteristic wave extension<br>(Wang et al., 2010) | • The signal has to be periodic.<br>• Based on the weak assumption that the data outside of the data span must be evenly symmetrical or oddly symmetrical to those inside. |
| Neural network extension<br>(Lee et al., 2010) | • Choosing the appropriate neural network varies with different data sets.<br>• The amount of work per sliding window is increased, resulting in a performance penalty. |

From the previous comparison, the boundary processing techniques in the current literature cannot totally overcome the end effects, especially when the analyzed signal contains weak low-frequency components [19].

### 6.2.2 Related research in interpolation for EMD

The purpose of the interpolation of EMD is to show the behavior of envelopes of the underlying sensor data [9]. That is, the existence of any obvious feature in the signal is expected to be reflected by the interpolating function [20]. Regardless of what interpolation method is adapted, preserving monotonicity of the data is required. The linear piecewise interpolation is the simplest method to maintain monotonicity. On the other hand, the envelope mean of upper and lower envelopes can be too sharp and therefore the envelope mean loses its smoothness [21]. As an alternative method of interpolating, Wolberg et al. [22] applied monotonic cubic spline interpolation to minimize the second derivative discontinuity. Also, Fritsch et al. [23] suggested a monotonic piecewise cubic interpolation algorithm that guarantees continuity of the first derivative.

In standard EMD [9], upper and lower envelopes are interpolated from the extrema using piecewise interpolating polynomials called cubic splines. These are the most common choice in most implementations of the EMD [24-29], which can minimize the total curvature over all other possible splines.

A B-spline EMD algorithm is introduced and developed by Riemenschneider et al. [24], which has a comparable performance to that of the standard EMD algorithm. A B-spline interpolation is used in the B-spline EMD algorithm in such a way that except for the first IMF, all others are linear combinations of B-splines [24]. The work reported by Chen et al. [25] established recursive formula of the Hilbert transform of B-splines. They proved that the derivative of a B-spline can be written as a combination of lower-order B-splines. Thus, the Hilbert transform of B-splines of a higher order can be computed using the Hilbert transform of B-splines of a lower order. Although the effectiveness of the B-spline EMD algorithm has been demonstrated to have a better convergence performance than the standard EMD, it does not highly reduce the end effects. In fact, as the scale of the IMF mode gets larger, the influence of the end effects become larger and it propagates into the low-frequency data components [24, 25].

Although the cubic splines are considered to be the smoothest possible interpolating polynomials [26], they are not suitable for online structural health monitoring for three reasons: first, they require more computational time because the solution for the cubic splines coefficients depends on the entire set of extrema points to be interpolated. So, the obtained interpolating curve will be continuously changed after having new extrema. Second, the cubic spline uses global information to calculate the derivative of the envelopes, but for online structural health monitoring, local signal behavior is more important [27]. Third, the cubic spline mean envelope may create extra extrema by itself, so the convergence of EMD is hard to achieve [24]. To tackle these problems, the piecewise cubic Hermite interpolating polynomial (denoted by PCHIP) [28] will be used for the purpose of interpolation in online EMD in this research. It has been shown that applying the PCHIP to the envelope mean approximation guarantees continuity of the first derivative without increasing the computational complexity [29]. Moreover, it maintains the monotonicity of the underlying sensor signal [30]. Table 6.2 summarizes the aforementioned EMD interpolation techniques.

**Table 6.2** Comparison of main EMD interpolation techniques

| EMD interpolation technique | Limitations |
|---|---|
| Linear piecewise interpolation<br>(De Boor, 1978) | • The envelope mean of the upper and lower envelopes can be too sharp and therefore the envelope mean loses its smoothness. |
| Cubic spline interpolation<br>(Fritsch et al.,1980) | • The obtained interpolating curve is continuously changed after having new extrema.<br>• It uses global information to calculate the derivative of envelopes.<br>• May create extra extrema by itself, leading to difficulty in achieving convergence of EMD. |
| A B-spline interpolation<br>(Riemenschneider et al., 2005) | • Does not highly reduce the end effects.<br>• As the scale of the IMF mode gets larger, the influence of the end effects becomes larger.<br>• It propagates into the low-frequency data components. |

From the previous comparison, using the standard EMD technique can not significantly overcome the end effects, especially when the scale of the IMFs gets larger.

### 6.3 Empirical mode decomposition

Empirical mode decomposition **(**EMD) is a fundamental and a necessary step to reduce any given data into a collection of simple oscillatory mode embedded in the raw data to which the Hilbert analysis can be applied [5]. The Hilbert transform is not capable of producing full description of frequency if the data contains more than one oscillatory mode at a particular time [9]. Due to this reason, data should be decomposed into independent oscillatory mode components called intrinsic mode functions (IMFs).

*Definition of intrinsic mode functions*

According to Huang et al. [9], an intrinsic mode function (referred to as IMF) is a function which satisfies two conditions: 1) the number of extrema and the number of zero crossings must either equal or differ at most by one; and 2) the mean value of the envelope defined by the local maxima and the envelope defined by local minima is zero at any point. Each IMF represents only one oscillation mode imbedded in the data with no complex riding waves. Moreover, an IMF is not restricted to a narrow band signal, in fact it can be both amplitude and frequency modulated [9]. In summary, IMF is symmetrical with respect to the local mean and has a unique local frequency which is different from the rest of other IMFs as illustrated in Figure 6.1.

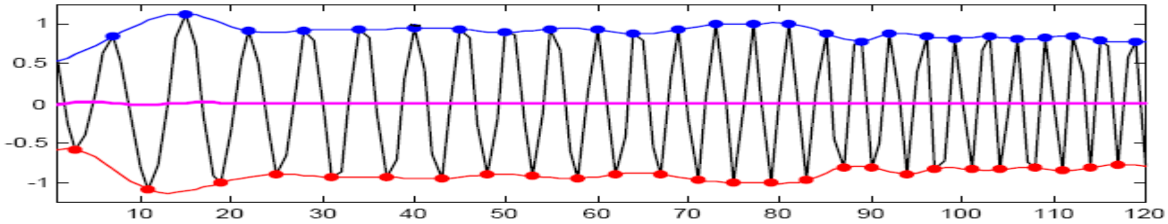

**Figure 6.1** An example of intrinsic mode function

*Sifting process and measuring procedure*

Sifting is the process of decomposition a signal into its IMF components by using EMD [31]. Figure 6.2 demonstrates the flow of EMD sifting process.

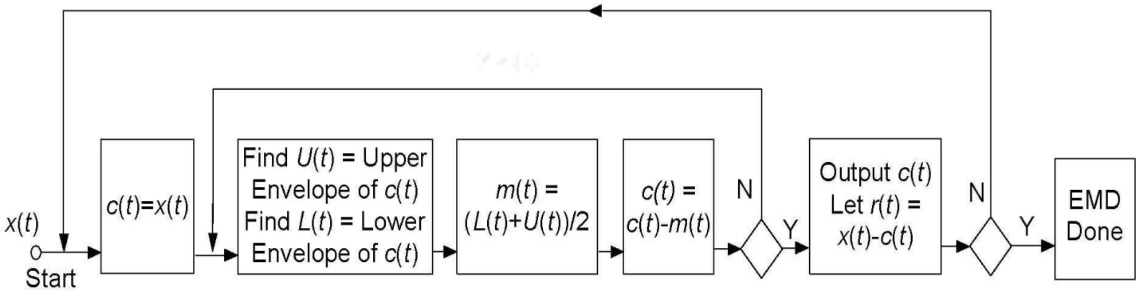

**Figure 6.2** The EMD sifting process [56]

*Stopping criteria*

IMFs need to retain meaningful physical sense in terms of amplitude and frequency modulations. The sifting process can be terminated on any of the following predetermined criteria

[9, 31]: 1) when the sum of the difference (SD) calculated between two consecutive sifted signals is smaller than a preset value; or 2) the residue becomes a monotonic function, from which no more IMF can be extracted. According to Ayenu et al. [32], a value of SD between 0.2 and 0.3 is used and the optimum value for successive sifting steps was found to be between 4 and 8.

*Practical implication and limitations of the standard EMD*

The standard EMD is an effective method in analyzing nonlinear and nonstationary signals [9, 12]. However, there are two main practical implications in using EMD for online monitoring; 1) the boundary effects, and 2) the construction of upper and lower envelopes using the *cubic splines.*

The proposed methodology based on EMD and locally weighted linear predictor for damage prediction is expected to overcome these limitations as can be shown in the following subsections.

The EMD combined with its Hilbert spectral analysis has shown promising results in damage identification [5]. In this chapter, the Hilbert phase will be used for the predicted damage point detection, while the damage severity prediction will be investigated using the energy of the selected IMF within the predicted window.

## 6.4 Hilbert spectral analysis

According to Refs. [9, 33], the Hilbert transform of a real valued function *x(t)* is defined as follows,

$$y(t) = \frac{P}{\pi}\int_{-\infty}^{+\infty}\frac{x(\tau)}{t-\tau}\,d\tau \tag{6.1}$$

where P is the Cauchy principle value. From Equation (6.3), properties of the signal *x(t)* can be locally emphasized using convolution of *x(t)* with *1/t*. Moreover, the function *x(t)* and its Hilbert transform *y(t)* form an analytic signal *Z(t)* given by,

$$z(t) = x(t) + iy(t) = a(t)e^{i\theta(t)} \tag{6.2}$$

where $a(t) = [x^2(t) + y^2(t)]^{1/2}$ represents the instantaneous amplitude of *x(t)*, and $\theta(t) = arctan\left(\frac{y(t)}{x(t)}\right)$ refers to the instantaneous phase of *x(t)*.

If the signal *x(t)* is mono-component, then the time derivative of the instantaneous phase $\theta(t)$ will be the instantaneous frequency *w(t)* given by

$$w(t) = \frac{d\theta(t)}{dt} \tag{6.3}$$

In order to compute instantaneous frequencies and amplitudes, the Hilbert transform *H(t)* is applied to each of the IMFs, which can be written as,

$$H(t) = \sum_{j=1}^{n} a_j\,(t)e^{i\int w_j(t)dt} \tag{6.4}$$

where $a_j(t)$ is the instantaneous amplitude associated with *j*-th IMF.

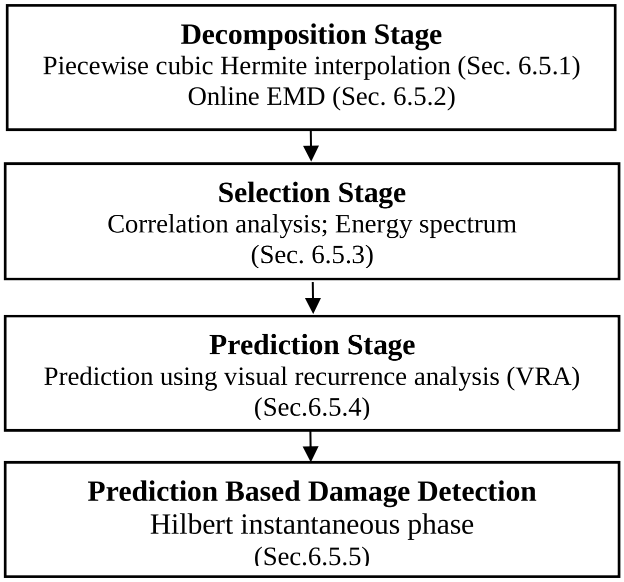

**Figure 6.3** The overall damage prediction methodology

## 6.5 The proposed methodology for online damage prediction

An effective online prediction scheme for analyzing the nonlinear and nonstationary signals based on local empirical mode decomposition has been developed in this Section. An illustration of the proposed hybrid damage prediction methodology is given in Figure 6.3.

### 6.5.1 Piecewise Cubic Hermite Interpolation

In standard EMD, upper and lower envelopes are interpolated from the exterma using a piecewise interpolating polynomials called cubic splines [34]. These are some common choices in implementations of the EMD, which can minimize the total curvature over all other possible splines. Although the cubic splines are considered to be the smoothest possible interpolating polynomial [26], they generate large errors while extrapolating [35] and the convergence of EMD is hard to achieve [24]. Thus, the cubic splines are not suitable for online structural health monitoring [27]. To tackle this problem, the piecewise cubic Hermite interpolating polynomial [28] is used in this research for the purpose of interpolation online EMD.

*Hermite interpolation theorem*

Let S be a discrete data set of distinct points defined as follows [36],

$$S = \left\{\left(x_i, f(x_i), f`(x_i)\right) : i = 0, 1, 2, \dots n\right\} \tag{6.5}$$

Then there exists a unique polynomial $H_{2n+1}(x)$ of degree 2n+1 or less that interpolates the data by matching the position of each point and the slope at each point. For *i=0, 1, 2, …n*

$$H_{2n+1}(x_i) = f(x_i) \text{ and } H`_{2n+1}(x_i) = f`(x_i) \tag{6.6}$$

$H_{2n+1}(x_i)$ is called the hermite polynomial interpolant to the data set S.

In this study, the piecewise cubic Hermite interpolation is used, where an individual cubic Hermite polynomial is fitted between each pair of points being interpolated. Also, the method of undetermined coefficients [26] is used to construct the cubic Hermite interpolation.

Using piecewise cubic Hermite interpolation for online EMD has the advantage of using local information only. That is, having new extreme to the end of the data will not change the entire spline. The whole curve remains static except the very last part as demonstrated in Figure 6.4. As can be seen from Figure 6.4, adding a new single point changes the entire extent of the curve using cubic spline. On the other hand, under the same scenario, using piecewise cubic Hermite interpolation changes only the last segment, which makes it more efficient for online SHM.

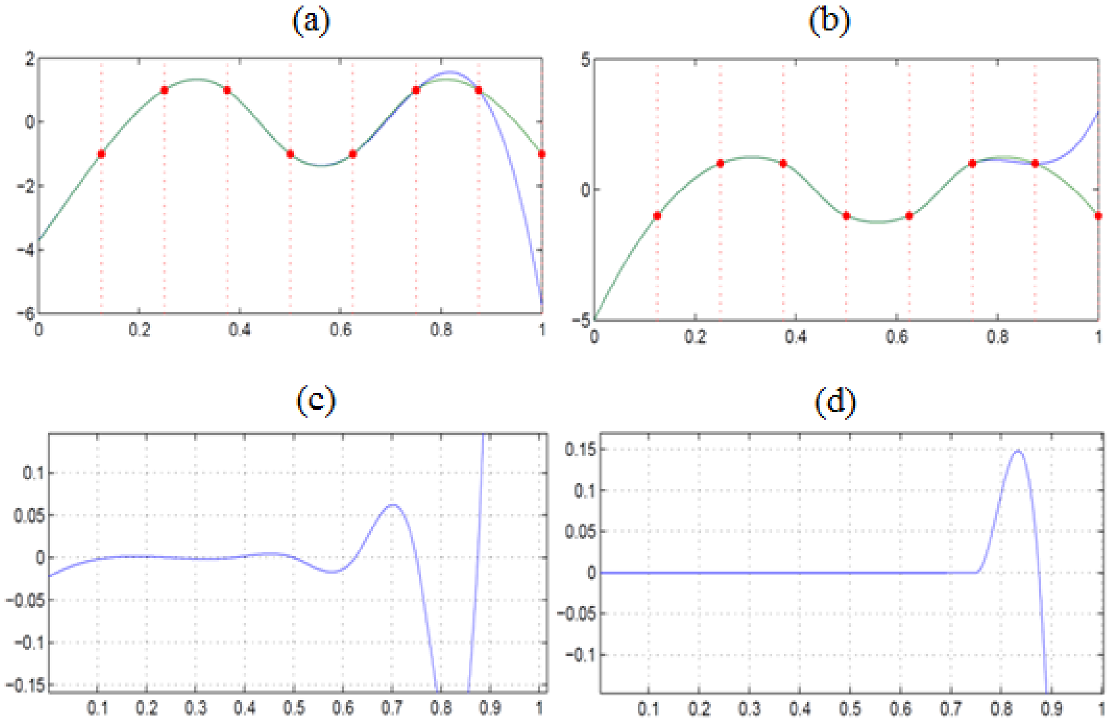

**Figure 6.4** (a) Cubic spline interpolation, (b) Hermite spline interpolation, (c) the new cubic spline after adding new extreme, (d) the new Hermite spline after adding new extreme [38]

### 6.5.2 Online empirical mode decomposition

The EMD algorithm of the entire recorded signal can have undesirable consequences, such as a high computational cost in obtaining IMFs, or obscuring physical interpretation [14]. In this section, an effective online monitoring method for the nonlinear and nonstationary signals based on local empirical mode decomposition is presented. We proposed a local implementation of the standard empirical mode decomposition using a sliding window of flexible length, and thus the sifting process will be conducted by blocks enabling the Hilbert Huang transform to be used as an effective online analysis technique.

*Adaptive overlapping sliding window approach*

Due to some limitations of the standard EMD discussed in section 6.2, a modified online EMD technique is applied to the adaptive overlapping windowed signal. The sifting process depends on interpolations between successive extrema, which required a finite number of successive extrema [14]. The adaptive overlapping sliding window method is demonstrated in Figure 6.5.

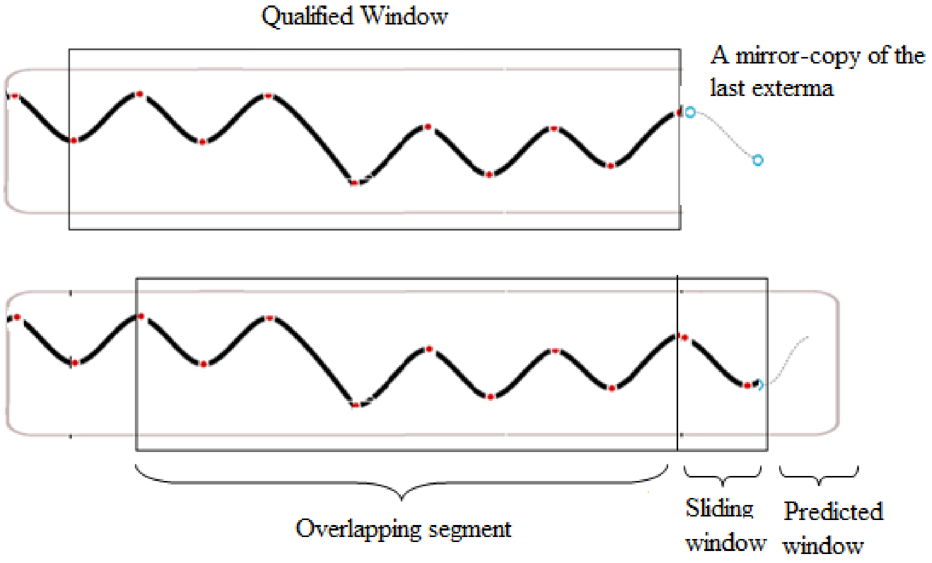

**Figure 6.5** Signal localization using overlapping windowing method

To produce meaningful IMFs, the initial window has to be chosen in such a way that it contains enough extrema (at least five minima and five maxima) [14, 31]. The rear edge of the window is placed at the first actual extrema and the front edge of the window is to be at the last extrema within the initial window. When new extrema is detected, the window moves adaptively in a way that the next window's front edge is on the new extrema, whereas the rear edge moves automatically to the next closest extrema. The window signals are extracted as long as the front and rear edges coincides with local extrema. The modified EMD based on piecewise Hermite interpolant will be applied for each windowed signal and the obtained IMFs will be statistically investigated to choose the best representative IMF to be used for prediction purpose.

To get more accurate and consistent IMFs in a reasonable time, the following considerations are taken into account in the calculating procedures of the sifting process. First, in order to avoid possible discontinuities, the same number of sifting steps is applied to all windows. It has been reported in the literature that a minimum of four iterations are sufficient to extract meaningful IMFs [14]. Second, there is always an overlapping segment of total extrema minus one, which reduces the computational cost in calculating IMFs.

The adaptive sliding window will be used until a change point has been detected, which will be used to predict the damage quantification. It should be pointed out that the initial window size is taken to be 1850 data points, so when applying the EMD on the windowed signal, it produces the same number of IMFs and it is sufficient for locally weighted predictor application. Also, the adaptive sliding window width is less than the number of zero crossings of the chosen IMF that represents the effective prediction horizon [32].

*Existence of the extrema within each new sliding window*

Based on the local extrema theorem in Calculus and Real Analysis [33], the existence of the extrema within each new sliding window is justified.

**Lemma 1:** For a streaming data, let $C$ = [a,b] be the minimum closed bounded interval of the data points in the sliding windowed signal. Also, let $f\colon [a,b] \to R$ be a continuous function, then there exist an extrema in the interior of C.

**Proof:**

We will prove the existence of the local maximum by contradiction and the existence of local minimum would be similar. Assume there is no maximum value, then the function $f(x)$ keeps increasing in its domain [a,b], that is, there exists a set of points $\{p_1, p_2, p_3, \ldots\}$ belongs to [a, b] such that $f(p_1) > 1$, $f(p_2) > 2$, $f(p_3) > 3$ and so on.

Next, split the closed bounded interval [a, b] into two equally sized sub-intervals and refer to the left half as $[a_1,b_1]$, while the right half refer to as $[a_2, b_2]$. Notice that there must be infinitely many $p_n$'s in the left half as well as in the right half. Pick any arbitrarily one from the $[a_1, b_1]$ and $[a_2, b_2]$ and call it $c_1$ and $c_2$, respectively.

Continue partition each new interval into two equally sized sub-intervals, the result will be a sequence of points $c_1$, $c_2$, $c_3$, …such that each point is one of the original $p_n$'s and as $n$ gets larger, the sub-interval from which $c_n$'s are chosen are getting smaller and smaller. That is the sequence converges to some point in [a, b]. Let $\lim_{n\to\infty} c_n = c$, then

$$\begin{aligned} f\,(c) &= f(\lim_{n\to\infty} c_n) \\ &= \lim_{n\to\infty} f\,(c_n) \\ &= \lim_{n\to\infty} f\,(p_n) \end{aligned} \tag{6.7}$$

Notice that $\lim_{n\to\infty} f\,(p_n)$ does not exist because the set of points { $p_1$, $p_2$, $p_{3}$,..} in [a, b] were chosen in such a way that $f(c_n)$ increased to infinitely. Then *f(c)* does not exist as well, which contracts the assumption that *f* is defined on the entire closed bounded interval [a, b]. Thus, there exist an extrema in the interior of C. Q.E.D

*Extrema's detection within each new sliding window*

The standard EMD algorithm use first derivative test to identify the extema. Basically, the first derivative test determines whether an interior point is an exterma by checking not only the value of the first derivative at the given point, but also the value of the derivative close to the point. According to the first derivative test [34], if $x_0$ is a critical point for a continuous function $f$, ( $f'(x_0) = 0$ ) and there is a positive number $\varepsilon$ such that:

1) $f'(x) > 0$ for all $x \in (x_0 - \varepsilon\,, x_0)$ and $f'(x) < 0$ for all $x \in (\,x_0\,, x_0 + \varepsilon)$, then $x_0$ is a local maximum point for *f*.

2) $f'(x) < 0$ for all $x \in (x_0 - \varepsilon, x_0)$ and $f'(x) > 0$ for all $x \in (x_0, x_0 + \varepsilon)$, then $x_0$ is a local minimum point for *f*

3) $f'(x)$ doesn't change sign on $(x_0 - \varepsilon, x_0) \cup (x_0, x_0 + \varepsilon)$, then $x_0$ is not a point of exterma for *f*

In most situations, the first derivative test successfully identify whether a given critical point is a local maximum or local minimum. However, there are some cases where it fails to work, that is, the continuous function could have a critical point at $x_0$ while the derivative does not have a constant sign close to $x_0$ [34].

As demonstrated previously, the first-derivative test is sufficient but not necessary to identify the extrema points. Also, to use the first derivative test for online SHM, we have to wait for the next point to decide whether the current point is a local extrema or not. Moreover, the first derivative test requires conducting two local sign computations over intervals, rather than at points.

For online SHM applications, the delay time has to be minimized and the computational cost has to be reduced. Thus, a more efficient technique called the second-derivative test based upon the concavity of the curve in the neighborhood of a critical point will be used to identify local extrema.

*Second-derivative test for extrema detection*

For a streaming data, let *C* = [a, b] be the minimum closed bounded interval of the data points in the sliding windowed signal. Also, let $f: [a, b] \rightarrow R$ be a continuous function and $x_0$ is a critical point in the interior of the domain of *f* , and *f* is twice differentiable at $x_0$. Then,

1) If $f''(x_0) > 0$, then $x_0$ is a point of local minimum.

2) If $f''(x_0) < 0$, then $x_0$ is a point of local maximum.

3) If $f''(x_0) = 0$, then the second derivative test fails and the first derivative test can be applied.

*Justifying the adaptive sliding window width*

The width of the sliding window is very important for good feature extraction and for an efficient prediction results. If the sliding window is too large, then a delay in processing the incoming data is expected and a delay may be introduced into the output. On the other hand, the EMD with too small sliding window may not be sensitive to the existence of structural defects. Therefore, an adaptive sliding window is developed depending on location of extrema. When a new extremum appears, the window moves adaptively in such a way that the next window's front edge is on the new extremum, whereas the rear edge moves automatically to the next closest extremum.

For prediction purpose, it is desirable to have a sliding window with width less than the number of the predicted points. Moreover, the stability of the locally weighted predictive model depends mainly on the bandwidth, which determines the size of the local neighborhood. According to Ref. [35], the bandwidth can be estimated by the number of points around the extrema within the sliding window and a reasonable value is equal to half of the number of data points in the half width of the specified extrema.

In this study, the adaptive sliding window width is considered to be less than the number of zero crossings of the chosen IMF that represent the effective prediction horizon [32].

### 6.5.3 Selection of intrinsic mode functions

EMD provides a number of IMFs and for the purpose of online structural health prediction, it is so important to select the most appropriate and representative one. In this study, statistical correlation analysis between the original signal and each IMFs, [36] as well as the normalized energy of each IMF [37] will be used to identify the best appropriate IMF. In fact, the final selection criterion has at least two IMFs with a highest normalized energy.

*Correlation analysis*

According to Ref. [36], statistical correlation methods such as Pearson Product Moment Correlation Coefficient (PPMC) and Kendall Rank Correlation (KRC) are demonstrated to be efficient methods to determine the most representative IMF from the set of all extracted ones. The correlation analysis starts with calculating Pearson Product Moment Correlation Coefficient (PPMC) and Kendall Rank Correlation Coefficient (KRC) between the original windowed signal and all extracted IMFs. The IMFs which have higher positive correlation coefficients both for PPMCC and KRCC are used a good candidate to be used for damage prediction stage. This ensures that the IMF change is consistent with the original signal change [36].

*Energy spectrum*

The Hilbert energy spectrum, is defined as,

$$E = \sum_f \sum_t |H_e(t,f)| = \sum_f \sum_t |a(t)^2| \tag{6.8}$$

where $H_e(t,f)$ represents the energy density spectrum and $a(t)$ is the instantaneous amplitude. In this study, the selected IMF is preferred to have a higher energy spectrum.

*Energy index of the selected IMF for damage severity prediction*

In this study, the online empirical mode decomposition works as a noise reduction technique, which along with optimal embedding parameters leads to a better predictability of the selected IMF. Specifically, the damage severity prediction will be investigated using the energy of the selected IMF within the predicted window.

For the purpose of predicting the severity of the damage of the underlying system, the proposed approach adopts a relative energy change index (RECI). It based on the percentage change between the values of the energy of the predicted IMF computed for undamaged state and the new value of the energy of the predicted IMF computed for the damage state. The proposed relative energy change index of the energy of the selected IMF is determined by,

$$\mathrm{REDI} = \left|\frac{E_{Average\ healthy} - E_{Average\ damage}}{E_{Average\ healthy}}\right| \times 100 \qquad (6.9)$$

As the value of REDI increases, the severity of damage increases. Thus, it has the capability to classify the different levels of damage as will be demonstrated in case study 3 (Sec. 6.6.3).

### 6.5.4 Prediction using visual recurrence analysis

Recurrence analysis (RA) is a graphical method developed to locate hidden recurring patterns, nonstationary and structural changes [38]. RA provides different local models for non-parametric time series prediction. Local models are used to predict future values by fitting a low order polynomial that maps a specific nearest neighbors onto their next values.

The general methodology of using the Visual Recurrence Analysis (VRA) technique for prediction purpose is as follows: For one step prediction, determine the last well known state of the underlying dynamic system. Then, search the time series to locate *k* similar states that have occurred in the past. That is, if the underlying sensor signal was generated by some deterministic map, then that map can be recovered from the data by examining its behaviors in the neighborhood of the last known state of the system. After that, the approximation of the deterministic map is used to predict the next step. In VRA, the prediction model can be constructed from range of classes (locally constant, kernel regression, nearest neighbor, locally linear, locally weighted linear and radial basis models). Among all different local models, the best model for the purpose of damage prediction in this research study turned out to be the locally weighted linear predictor (LWLP), which will be used in this study. More detailed information about the Recurrence Analysis and the locally weighted linear predictor can be found in Refs [39] and [40].

*The locally weighted linear predictor*

Locally weighted linear predictor was applied into the domain of robot learning by Atkeson [25]. Then Dietterich et al. [26] used the (LWLP) in the domain of memory-based learning techniques. Among all possible linear local models within the visual recurrence analysis, The justification for choosing the locally weighted liner predictor among other local models within the visual recurrence analysis came from their suitability for online learning [27]. Another advantage of this method is due to its fast incremental learning and avoidance of negative interference between old and new training sensor measurements. Moreover, the locally weighted predictor is the best asymptotic minimax linear smoother and it has a high asymptotic efficiency [28]. The locally weighted liner predictor fits a surface to nearby points by either weighting the training criterion or by directly weighting the data using a distance weighted regression. To construct the locally weighted linear model to generate predictions, certain parameters need to be chosen as will be discussed below.

*Distance function*

There are different methods to define and use a distance function [29]. The first one is global distance functions that use the same distance function at all parts of the input space. A uniform metric approach is used to set the distance function parameters on each query by an optimization process [30]. The last method is the point-based local distance functions (referred to as a variable metric), in which each stored data point has a unique distance function and corresponding parameters values [30].

*Smoothing parameters*

A smoothing parameter or bandwidth parameter defines the scale (how much the inputs are stretched or squashed) over which generalization is performed. According to Scoot [41], there are different approaches to apply this parameter: first, fixed bandwidth selection, in which data with constant size and shape are used [31], second, select the nearest neighbor bandwidth, in which the data volume increases and decreases in size according to the density of nearby data, finally, determine the point-based local bandwidth, in which each stored data point has associated with it a specific bandwidth.

*Weighted functions*

The weighting function (referred to as a kernel function) is used to assign the contribution of each neighbor to the prediction process [31]. According to Ref. [27], the maximum value of the kernel function should be at zero distance and it decays smoothly as the distance increases. Also, the kernel function should always be non-negative to avoid increasing training error. It is pointed out that, kernels with a fixed finite radius increases the possibility of not having enough or any points within the non-zero area [27]. There are different kernel functions, such as the Gaussian kernel, exponential kernel, quadratic kernel, uniform kernel, and inverse kernel [27].

In this study, the variable metric approach will be used with the Euclidean distance, in which a distance along a particular dimension can be selected by minimizing the cross validation error [32]. Regarding the bandwidth function, the variable local bandwidth will be applied in this study due to the following reasons: it adapts to the data distribution, different levels of noise, and changes in the curvature of the function. Since there is no clear evidence in the literature that the choice of the weighting function is crucial in prediction results [31], the selection of the best kernel function was decided after trying different kernel functions, and turned to be the Gaussian function.

### 6.5.5 Hilbert instantaneous phase for the predicted damage point detection

The Hilbert instantaneous phase is a unique feature which describes the traveling structural wave propagation [42]. It has been mathematically proved the dependency of the Hilbert instantaneous phase on the structural parameters such as mass, damping and stiffness [43]. Thus, it is an effective and sensitive feature to be used for damage prediction. Moreover, According to Zemmour [4], the slope change in the Hilbert phase occurs at the time where the travelling wave meets the structure’s damage. As soon as the wave passes the structural damage, the slope of the damaged phase behaves as the undamaged slope [43, 44].

The instantaneous Hilbert phase is defined for the real-valued time domain signal *x(t)* and hence defined by,

$$\theta(t) = arctan\left(\frac{H[x(t)]}{x(t)}\right) \tag{6.10}$$

where $H[x(t)]$ is the Hilbert transform. Using empirical mode decomposition, the signal *x(t)* is decomposed into different IMFs, which admit a well behaved Hilbert transform [9]. Thus, the instantaneous phase can be written as,

$$\theta_i(t) = arctan\left(\frac{H[c_i(t)]}{c_i(t)}\right) \tag{6.11}$$

where $c_i(t)$ represents different IMFs. Since IMFs are symmetrically local with respect to the mean zero level, the instantaneous unwrapped phase is also local and increases linearly over time. It should also be pointed out that the unwrapped phase function is no longer restricted to an interval of length *( 2π )* and it increases monotonically.

In this study, the instantaneous phase in Equation (6.11) of each IMF is used as a monitoring statistics of statistical control charts for change point detection. In fact, the control charts in the multiple chosen IMFs can be constructed independently due to the property of the EMD, i.e., the spaces of IMFs are nearly orthogonal to each other. Thus, univariate control charts are applied for each individual IMFs, instead of multivariate control charts.

### 6.6 Case studies

In this section, three case studies are presented to illustrate the effectiveness of the proposed damage prediction methodology. 1) In the first case study, a synthetic test signal example is used to demonstrate the efficiency of the proposed boundary effect processing method over other methods; 2) Simulation data generated by different ARMA models was used in the second case study to test the sensitivity of the proposed method to different process changes; 3) In the third case study, the numerically simulated datasets of the American Society of Civil Engineering (ASCE ) benchmark structure [45] are used to test the prediction accuracy of the proposed hybrid Hilbert energy spectrum-locally weighted prediction scheme for online SHM.

### 6.6.1 Case study 1: the performance of the proposed boundary effect processing method

To demonstrate the performance of the proposed boundary effect processing method in terms of computational time and accuracy, a synthetic test signal example is used, which is adapted from Ref. [46] with different values of parameters. The modified synthetic test signal is written as,

$$x(t) = \sum_{i=1}^{k} e^{-0.1(t-t_i)^2} . \ sin(2\pi . f_i \ . \ (t-t_i) + \theta_i) \tag{6.12}$$

where, the amplitude of all transient components equals 1, $k$ being the number of transient components, the initial phase is zero and other parameters of the synthetic test signal are shown in Table 6.3. Also, the signal and its spectrum are shown in Figure 6.6. Figure 6.7 gives the signal's IMFs produced by the EMD and the respective FFT spectrums of the IMFs. Moreover, Figure 6.8 shows the Hilbert spectrum for each IMF.

**Table 6.3** Parameters for constructing the synthetic test signal [46]

| **Parameter** | **Transient component** | | | | | | | |
|---|---|---|---|---|---|---|---|---|
| | 1 | 2 | 3 | 4 | 5 | 6 | 7 | 8 |
| $t_{i\ (ms)}$ | 10 | 20 | 30 | 40 | 10 | 20 | 30 | 40 |
| $f_{i\ (Hz)}$ | 1200 | 1200 | 1300 | 1300 | 600 | 600 | 500 | 500 |

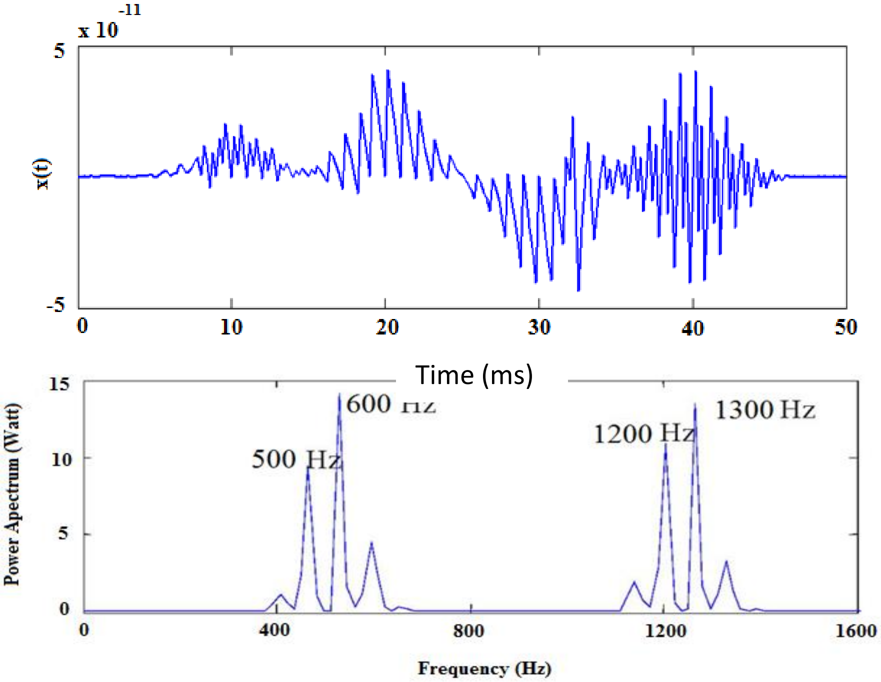

**Figure 6.6** The synthetic test signal (up) along with its spectrum (down)

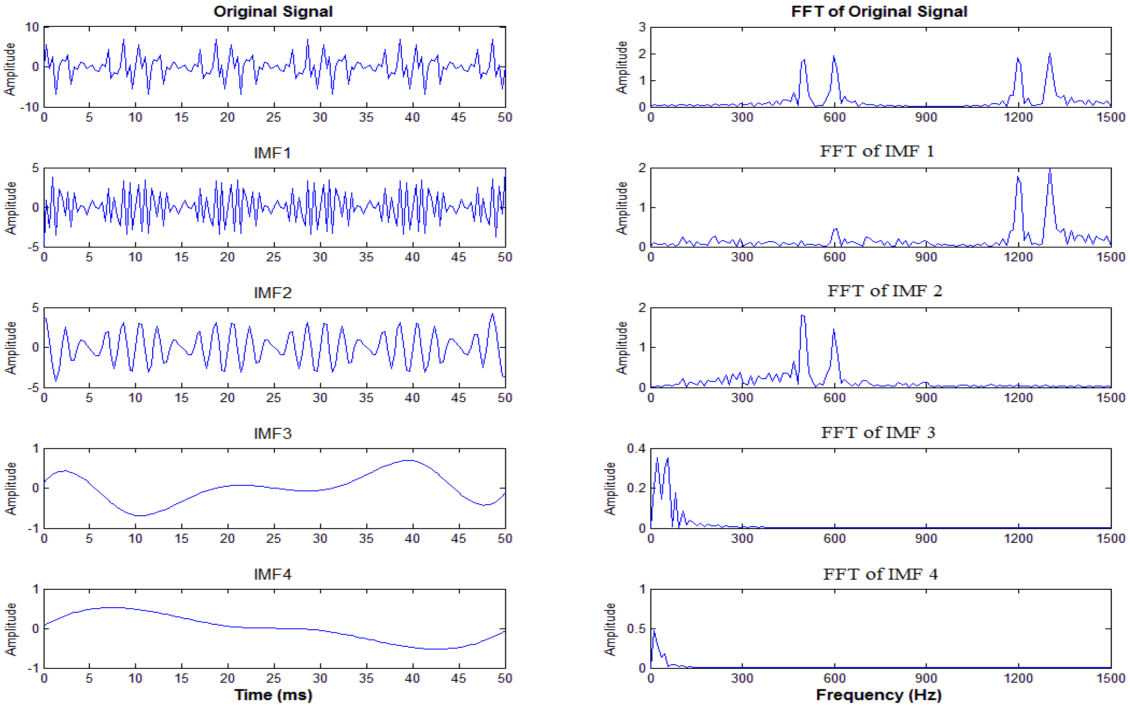

**Figure 6.7** The synthetic signal, its IMFs, and their FFTs, respectively

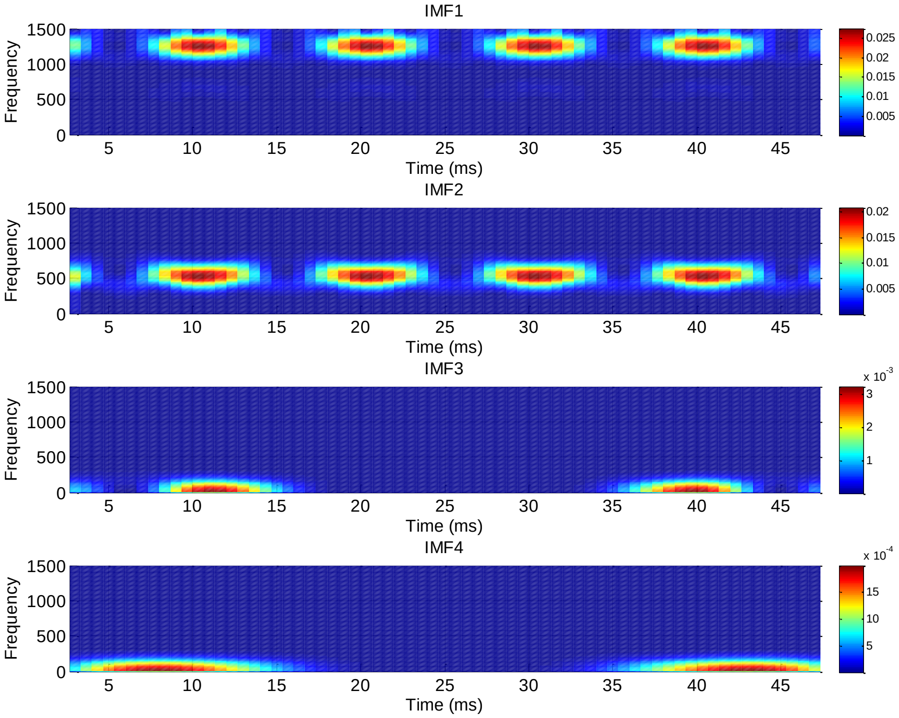

**Figure 6.8** Hilbert spectrums for each IMF of the synthetic signal

The given synthetic test signal is decomposed using EMD with the two well-known boundary process techniques, which were introduced in section 6.2.1, namely: “Extension-based boundary processing method” and “Cosine window-based boundary processing method”. Then, the CPU time for the EMD using all three methods was compared and the results are shown in Figure 6.9.

To test the accuracy of the EMD using the proposed boundary method, two evaluating criteria are used. The first criterion includes the mean absolute error of the residue for all three boundary distortion processing methods of EMD as shown in Table 6.4. The second one is the statistical Kurtosis indicator, which is the fourth moment of the spectral amplitude difference from the mean level (see Table 6.5).

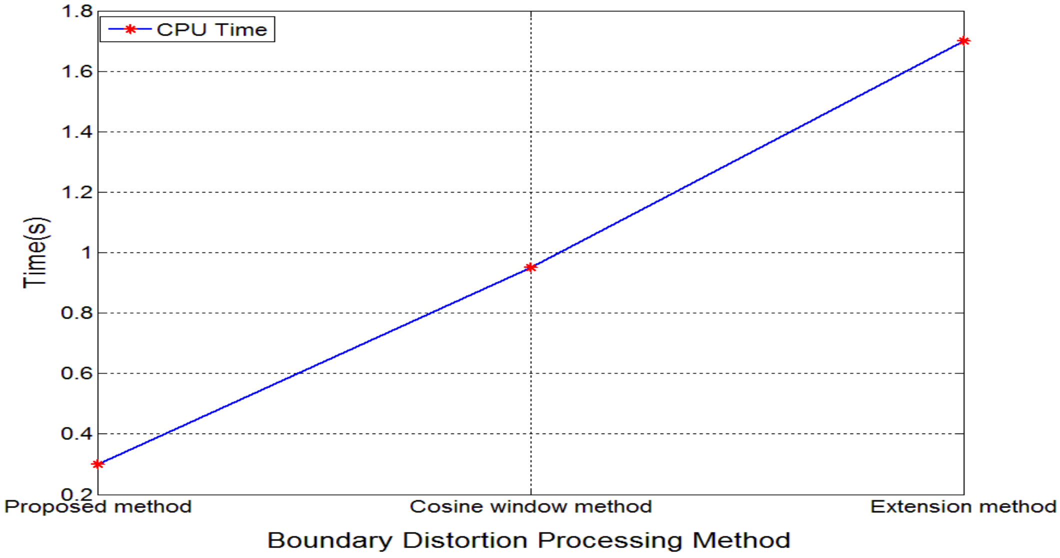

**Figure 6.9** Comparison of CPU time between different boundary distortion processing methods of EMD

**Table 6.4** Mean absolute error of the synthetic test signal with three methods

| **Boundary process Method** | **Mean absolute error (MAE)** |
|---|---|
| Extension method | 0.0031 |
| Cosine window method | 0.0046 |
| Proposed method | 0.00009 |

From Table 6.4, the proposed boundary process method has achieved the minimum mean absolute error over the other two methods. Therefore, the boundary distortion of the decomposed signal can be reduced using the proposed adaptive sliding window-based boundary processing method.

According to Anand et al. [13], the value of the kurtosis of each of the IMFs is a good indicator of the effect of the boundary distortion. As the boundary effect increases, the value of the kurtosis increases accordingly. As shown in Table 6.5, the proposed method has the smallest kurtosis values. Thus, it has achieved a more accurate decomposition of IMFs over other boundary processing methods.

**Table 6.5:** Kurtosis of intrinsic mode functions for the three methods

| **Intrinsic mode function** | **Kurtosis** | | |
|---|---|---|---|
| | Extension method | Cosine window method | Proposed method |
| IMF1 | 2.6708 | 3.1839 | 1.0054 |
| IMF2 | 2.7446 | 3.2006 | 1.0472 |
| IMF3 | 2.4883 | 2.9641 | 1.0581 |
| IMF4 | 2.2650 | 2.6742 | 1.0039 |

According to the results of the correlation analysis and the normalized energy of each IMF, shown in Table 6.6, the first and the second IMFs have the highest normalized energy. According to Ref. [9], the first IMF should be eliminated due to the fact that it contains most of the signal's noise, but since the synthetic signal is created free of noise, then, the first and second IMF are used to illustrate the effectiveness proposed boundary process method.

**Table 6. 6** The calculated normalized energy for each selected IMF of the synthetic signal

| **IMF** | **Pearson correlation coefficient** | **Kendall correlation coefficient** | **Normalized energy** |
|---|---|---|---|
| **1** | 0.451 | 0.302 | 0.551 |
| **2** | 0.597 | 0.378 | 0.456 |
| **3** | 0.012 | 0.102 | 0.016 |
| **4** | 0.160 | 0.061 | 0.013 |

It has been reported by Qi et al. [11] that for a nonstationary practical signal, the combination of the extension method with the cosine window method provides more satisfied results with respect to end effects. So, the end effects of a signal are further investigated for the suggested combined method (cosine window method and extension method) and the proposed boundary process method.

The first IMF of the synthetic test signal are further analyzed using Hilbert spectrum and has been plotted in Figure 6.10 and Figure 6.11, where the spectra are obtained using the combined extended-cosine window method and the proposed adaptive sliding window-based boundary processing method, respectively. Comparing Figure 6.10 with Figure 6.11, the proposed method has achieved better performance against the boundary effects, which usually distort the useful information within the underlying process. That is, the energy spectrum calculated from the instantaneous frequency is more preserved when using the proposed method, making the prediction of the damage severity more accurate.

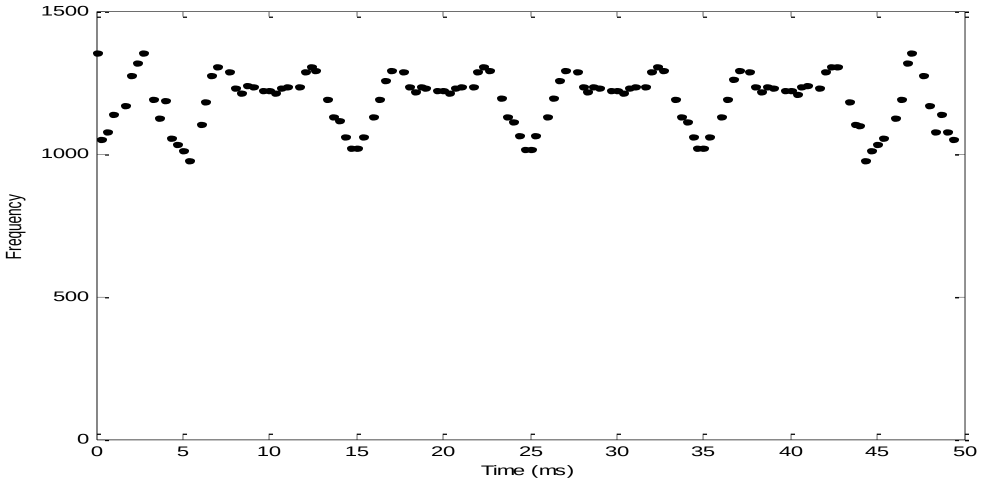

**Figure 6.10** Hilbert spectrum for the first IMF using the combined extended-cosine window method

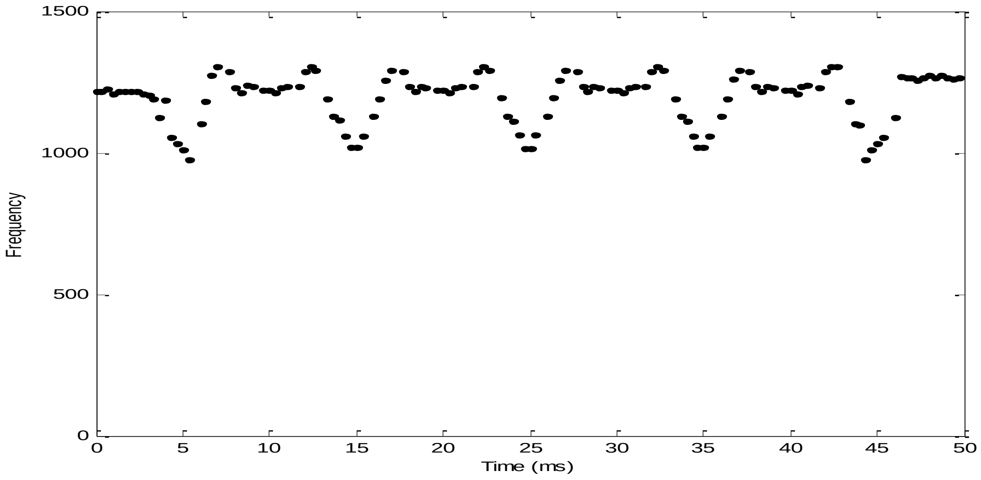

**Figure 6.11** Hilbert spectrum for the first IMF using the proposed boundary processing method

### 6.6.2 Case study 2: detecting process changes using the proposed method

This case study demonstrates the effectiveness of the proposed instantaneous Hilbert phase in detecting the process changes, which are simulated using time series ARMA models. In this case study, based on the results of the correlation analysis of each IMF along with the normalized energy, the third and the fourth intrinsic mode functions were chosen as the best representative of the original signal for the purpose of further analysis. The performance of the proposed method is compared with the multi-scale monitoring scheme using wavelet decomposition reported by [41], which is able to detect the changes caused by not only mean shifts as the existing wavelet-based statistical process control methods [47-49], but also the variance change of the dynamic processes.

According to Guo et al. [41], the auto-correlated measurement data $y_t$, are generally modeled as

$$y_t = x_t + e_t$$

$$x_t = \phi_1 x_{t-1} + \ \dots \phi_n x_{t-n} - \theta_1 a_{t-1} - \cdots \theta_m a_{t-m} + a_t$$

where, $a_t$ is the process noise, which is assumed to be independent of sensor noise $e_t$ as shown in the block diagram in Figure 6.12.

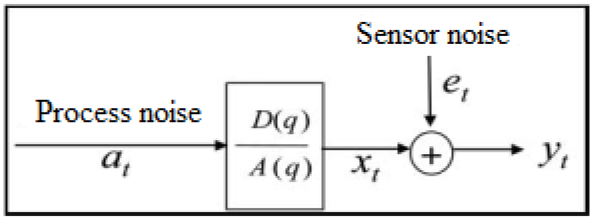

**Figure 6.12** The block diagram of the process structures [41]

Under the normal process condition, $H_0\colon y_t \sim N(0, \sigma_a^2 + \sigma_e^2)$, where $\sigma_a^2$ is monitored to reflect the change of the process variance. For comparison purposes, we used the three fault tests [41], namely:

4) Mean shift of process noise: $H_1^1: a_t \sim N(\mu_a,\ \sigma_a^2)$

5) Variance change of process noise: $H_1^2: a_t \sim N(0, \delta_a^2\ \sigma_a^2)$

6) Variance change of measurement errors: $H_1^3: e_t \sim N(0, \delta_e^2\ \sigma_e^2)$

To illustrate the effectiveness of the proposed method for detecting the occurrence of process faults (mean shift and variance change of the process noise) and variance change of measurement errors, a higher order auto-correlated processes that have strong dynamic characteristics represented by ARMA (2, 1) is used (see Table 6.7). Each model is stable with *i.i.d.* Gaussian process noise and all their characteristic roots are within the unit circle [50].

**Table 6.7** ARMA (2, 1) models with different parameters [41]

| **Model** | **Parameters** | |
|---|---|---|
| | $A(q)$ | $D(q)$ |
| Model 1 | $1 - 0.99\, q^{-1} + 0.49\ \ q^{-2}$ | $1 - 0.7q^{-1}$ |
| Model 2 | $1 - 0.1\, q^{-1} + 0.8\ \ q^{-2}$ | $1 - 0.7q^{-1}$ |
| Model 3 | $1 - 0.6\, q^{-1} + 0.4\ \ q^{-2}$ | $1 - 0.7q^{-1}$ |

*Fault one* (*mean shift of process noise*)

For measuring the performance of the proposed change point detection method based on Hilbert instantaneous phase (denoted as HIPH-CPD), the mean delay time ($\tau$), which is the time between a change point and its detection, was investigated for detecting mean shift of process noise for each model listed in Table 6.7 using the third and fourth IMFs . For the purpose of comparison, two different control charts are used: the standard EWMA chart that directly monitors original signals (denoted by S-EWMA) and a wavelet-based EWMA chart using the optimal monitoring level of Haar wavelet coefficients (referred to as W-EWMA) [41]. More detailed information of multi-scale monitoring of auto-correlated processes using Haar wavelet analysis can be found in Ref. [41].

As an equivalent measure for performance, the out-of-control average run length ($\text{ARL}_1$), which is the number of observations needed until a change is detected was used in both S-EWMA and W-EWMA. The control limits of EWMA charts are set up to make the in-control average run length ($\text{ARL}_0$) approximately equal to 370 [41, 51]. The weighted factor (λ=0.2) is used as a reference for performance evaluation throughout this case study. To illustrate the effectiveness of the proposed method for detecting the mean shift of the process noise (fault one), it was assumed that, when the process is under control ($H_0$), the process noise follows the distribution of $N(0, 1)$. Assume under fault condition one ($H_1^1: a_t \sim N(\mu_a,\ \sigma_a^2)$) that the process noise changed to three different normal distributions: $N(0.5, 1)$, $N(1, 1)$ and $N(1.5, 1)$, respectively, at time step equal to 1901 (31 minutes and 41 seconds). For each model listed in Table 6.7, the($\tau$) and ($\text{ARL}_1$) were investigated for HIPH-CPD (both the third and fourth IMFs) and S-EWMA, W-EWMA, respectively. Each simulation is repeated 5000 times to ensure the accuracy of the $\tau$ and $\text{ARL}_1$. The performance of HIPH-CPD (the third IMF), W-EWMA and S-EWMA in detecting mean shift of process noise was tested and shown in Figure 6.13.

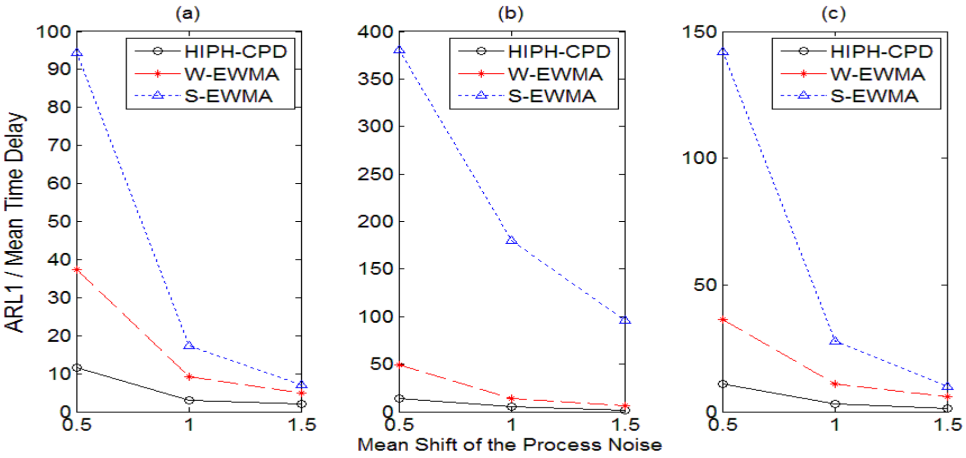

**Figure 6.13** $\text{ARL}_1$ / $\tau$ comparison of the proposed method, W-EWMA and S-EWMA for detecting mean shift of the process noise for the three models mentioned in Table 6.7. (a) Data generated by model 1. (b) Data generated by model 2. (c) Data generated by model 3

The proposed change-point detection method based on Hilbert instantaneous phase (HIPH-CPD) demonstrates a better detection performance than S-EWMA and W-EWMA control charts. In fact, the comparison indicates that the proposed scheme is more sensitive to the process noise mean shift than both W-EWMA and S-EWMA control charts.

*Fault two* (*variance change of process noise*)

For detection variance change of the process noise, the mean delay time ($\tau$) of the proposed change-point detection method based on Hilbert instantaneous phase (denoted as HIPH-CPD), was investigated for each model listed in Table 6.7. For the purpose of comparison, two different control charts are used; a wavelet based CUSUM chart, referred to as W-CUSUM; and a standard CUSUM chart, denoted as S-CUSUM. The control limits of CUSUM charts are designed to make the in-control average run length ($ARL_0$) approximately equal to 370, in which the process noise follows the normal distribution with (0, 1) and λ=0.2 [41, 51]. Also, it is assumed that under fault condition two ($H_1^2: a_t \sim N(0, \delta_a^2\ \sigma_a^2)$) the process noise changed to two different normal distributions: $N(0,\ 2^2)$ and $N(0,\ 3^2)$, respectively, at time step equal to 1901 (31 minutes and 41 seconds). For each model listed in Table 6.7, ($\tau$) and ($ARL_1$) were investigated for HIPH-CPD (both the third and fourth IMFs) and W-CUSUM, S-CUSUM, respectively. Each simulation has been replicated 5000 times to ensure the accuracy of the $\tau$ and $ARL_1$. Following the same procedure as in Ref. [41], the performance of HIPH-CPD, W-CUSUM and S-CUSUM in detecting the variance change of the process noise was tested and shown in Figure 6.13. under the assumption that the mean of the process noise is in-control.

As can be seen from Figure 6.14, the proposed HIPH-CPD (the third IMF) method for detecting the variance change of the process noise has slightly better detection power than both CD-CUSUM and W-CUSUM.

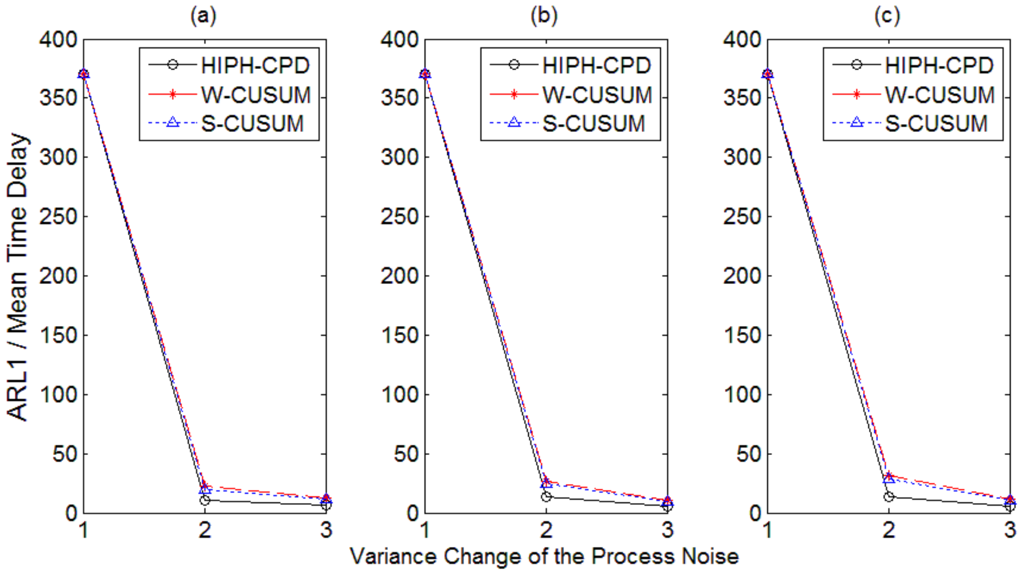

**Figure 6.14** ARL$_1$ / $\tau$ comparison of the proposed method, W-CUSUM and S-CUSUM in detecting variance change of the process noise with $N(0,1)$ for the three models mentioned in Table 6.7. (a) Data generated by model 1. (b) Data generated by model 2. (c) Data generated by model 3

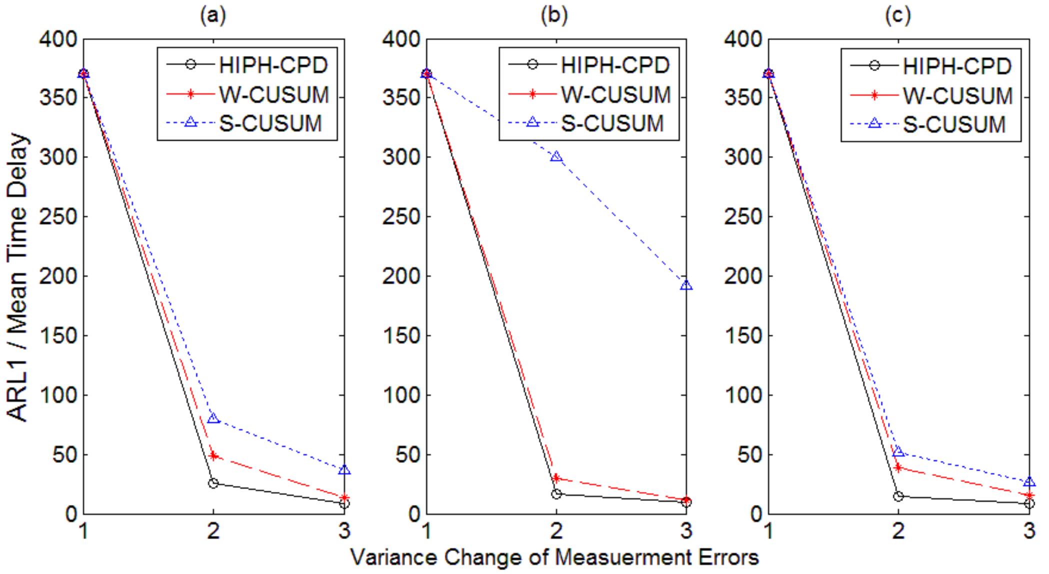

**Figure 6.15** ARL$_1$ / $\tau$ comparison of the proposed method, W-CUSUM and S-CUSUM in detecting variance change of measurement errors for the three models mentioned in Table 6.7. (a) Data generated by model 1. (b) Data generated by model 2. (c) Data generated by model 3

*Fault three* (*variance change of measurement errors*)

Following the work by Guo et al. [41], the performance of HIPH-CPD (both the third and fourth IMFs), W-CUSUM and S-CUSUM in detecting variance change of measurement errors was tested and shown in Figure 6.15.

It can be seen that the proposed HIPH-CPD (the third IMF) method takes shorter detection delay than the W-EWMA, and it shows a better detection power in detecting variance change of measurement errors than the standard CUSUM.

The simulation results in this case study indicate that the proposed HIPH-CPD method outperforms both wavelet and standard EWMA and CUSUM control charts in detecting the process changes.

### 6.6.3 Case study 3: structure damage prediction using Hilbert instantaneous phase

To validate the proposed method in predicting the severity of different damage patterns at relatively high levels of noise, the proposed method is applied to a benchmark structure, which was designed by the American Society of Civil Engineers (ASCE) for the applicatoin of SHM [45]. The results of applying the proposed method to the benchmark structure were compared with Morlet wavelet based damage feature, which is widely used in SHM due to its high sensitivity to very small damages [52]. The benchmark structure from which simulation data was taken consists of a 4-story and 2-bay by 2-bay steel frame structure as shown in Figure 6.16 [45].

As illustrated in Figure 6.15, a bracing system placed along the diagonal was fixed for each bay. To emulate a real structure a concrete slab was built at each floor, and the removal of this bracing system is designed to simulate damage to the structure. For the experiment wind ambient excitation, two types of forced excitation sources were applied, namely, impact hammer test and electrodynamics shaker. A more detailed description of the benchmark structure problem can be found in Ref. [45]. A simulation program for the response data of the ASCE benchmark structure is available at Ref. [53]. It is a MATLAB program based on 12- degree of freedom (DOF) shear-building finite element model [45]. One undamaged pattern and six damage patterns generated from this benchmark model were used and summarized in Table 6.8.

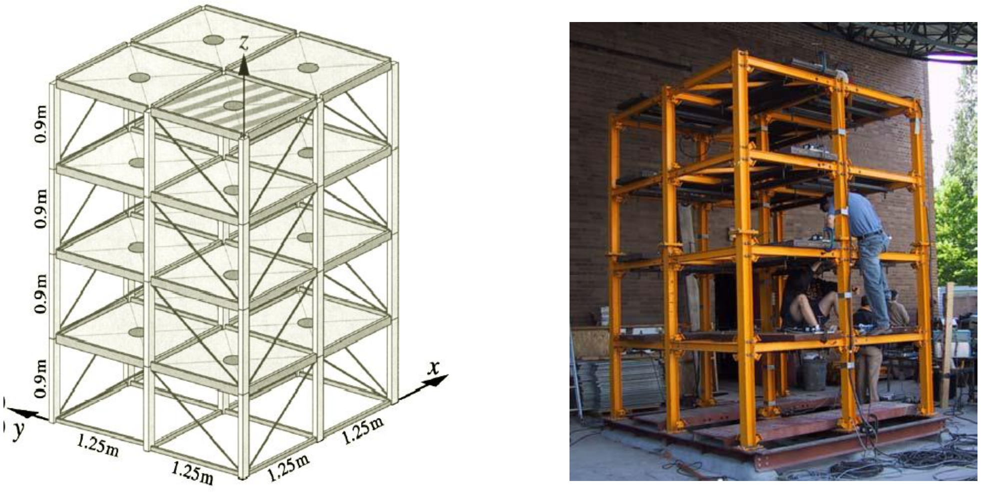

**Figure 6.16** Benchmark structure: (a) diagram of the analytical model and (b) steel-frame structure [45]

**Table 6.8** Six damage patterns generated from the ASCE benchmark structure

| Damage pattern | Damage description |
|---|---|
| $D_0$: Damage pattern zero | No damage |
| $D_1$: Damage pattern one | Remove all braces in 1st floor. |
| $D_2$: Damage pattern two | Remove all braces in 1st and 3rd floor. |
| $D_3$: Damage pattern three | Remove a brace near sensor location 2 at 1st floor |
| $D_4$: Damage pattern four | Damage pattern 3 & remove a brace near sensor 9 at 3rd floor. |
| $D_5$: Damage pattern five | Damage pattern 4 & loosen floor beam near sensor 3 at 1st floor. |
| $D_6$: Damage pattern six | Remove 2/3 stiffness of a brace near sensor 2 at the 1st floor. |

*Decomposition stage*

To demonstrate the capability of the Hilbert instantaneous phase for structure damage prediction, a series of signals are constructed by combining the undamaged state of the ASCE benchmark structure and the damaged state. The reconstructed signal has information of the time when the damage occurs with different damage patterns. For the purpose of testing the prediction accuracy of the proposed method, a very slight damage of the structure which is represented with pattern three. The streaming data in this case study is acceleration data with a sampling rate of 1 Hz and contains a very slight damage at 32 minutes and 10 seconds.

The initial windowed signal length was chosen to be 1850 data points with a sliding window of 20 data points to satisfy a minimum value of $R^2$ of approximately 0.6. The proposed prediction scheme is applied to the reconstructed steaming signal, which is decomposed using the proposed modified EMD into eleven IMFs. The first five IMFs are retained and all other IMFs are added to the residue, which is in agreement with results reported in Ref. [54] (see Figure 6.17).

*Selection stage*

To decide which IMFs are best representative of the original initial windowed signal, the statistical correlation coefficients and the energy of all the selected IMFs are calculated as the squared sum of all the instantaneous amplitude and normalized to the total energy of whole signal (see Table 6.9).

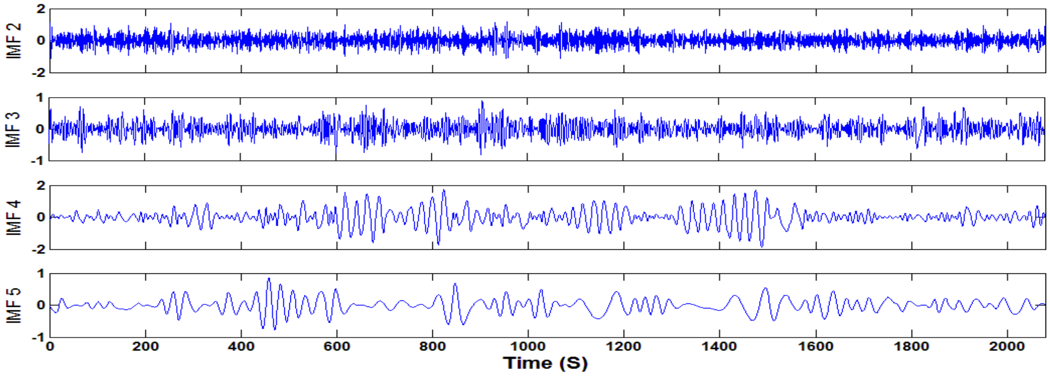

**Figure 6.17** The selected IMFs of the simulated signal representing damage pattern number three

According to the results of the correlation analysis of each selected IMF along with the normalized energy, the second and the fourth intrinsic mode functions were chosen as the best representative of the original windowed signal for the purpose of further prediction analysis. The proposed selection criterion eliminates the first IMF, which contains most of the signal’s noise [9].

**Table 6. 9** The calculated statistical correlation coefficients and normalized energy for each selected IMF

| IMF | Pearson correlation coefficient | Kendall correlation coefficient | Normalized energy |
|---|---|---|---|
| **1** | 0.073 | -0.005 | 0.32 |
| **2** | 0.357 | 0.238 | 0.29 |
| **3** | 0.126 | 0.113 | 0.06 |
| **4** | 0.620 | 0.486 | 0.27 |
| **5** | 0.092 | 0.076 | 0.04 |

*Prediction stage*

The second and the fourth IMFs time series of the initial windowed signal will be used as an input for the locally weighted predictor with the following parameters: Gaussian Kernel and Euclidean distance. The bandwidth that controls the size of the neighborhood in which the nearest neighbors are sought has found to be 15. Moreover, the prediction horizon is chosen to be 20, which is still less than the number of zero crossings of the chosen IMF that represent the effective prediction horizon [32].

*Validation the accuracy and stability of the proposed predictor*

To test its performance on the most representative IMFs, the proposed locally weighted linear predictor is compared with different prediction techniques such as exponential smoothing, stepwise autoregressive and ARIMA. Specifically, the prediction accuracy has been tested using the Mean Absolute Percent Error (MAPE) and $R^2$ [55], whereas, Variance of Absolute Percentage Error (VAPE) is used to test the prediction stability [56]. The results of the comparison are summarized in Table 6. 10.

The results from the comparison in Table 6.10 reveal that the proposed method has achieved the highest $R^2$ and less MAPLE and VAPE, thus it outperforms the other three models in terms of prediction accuracy and stability.

**Table 6.10** Prediction comparison for the first windowed signal over twenty forecasting steps ahead

| **Model** | **MAPE (%)** | $R^2$ | **VAPE (%)** |
|---|---|---|---|
| Exponential Smoothing | 9.29 | 0.218 | 0.81 |
| Stepwise Autoregressive | 8.47 | 0.473 | 0.63 |
| ARIMA | 11.13 | 0.115 | 1.12 |
| Proposed Method | 6.91 | 0.56 | 0.47 |

*Hilbert instantaneous phase for damage prediction*

After validating the accuracy and stability of the locally weighted linear predictor, we keep calculating the Hilbert instantaneous phase, which extends linearly over time for the most representative IMFs (both the second and the fourth IMFs) until a slope change in the Hilbert phase is detected outside the upper and lower threshold. It should be pointed out that the threshold is chosen experimentally to be 4% of the original slope of the Hilbert phase. As discussed in section 6.3, the slope change in the Hilbert phase occurs at the time where the travelling wave meets the structure’s damage. As soon as the wave passes the structural damage, the slope of the damaged phase behaves as the undamaged slope. Thus, the Hilbert phase for the second and fourth IMFs will be simultaneously predicted. In this case study; there is an early change in the Hilbert phase outside the threshold band for the *fourth* IMF in the fifth sliding window at time step equal to 1933 as demonstrated in Figure 6.18 and a more zoomed one in Figure 6.19.

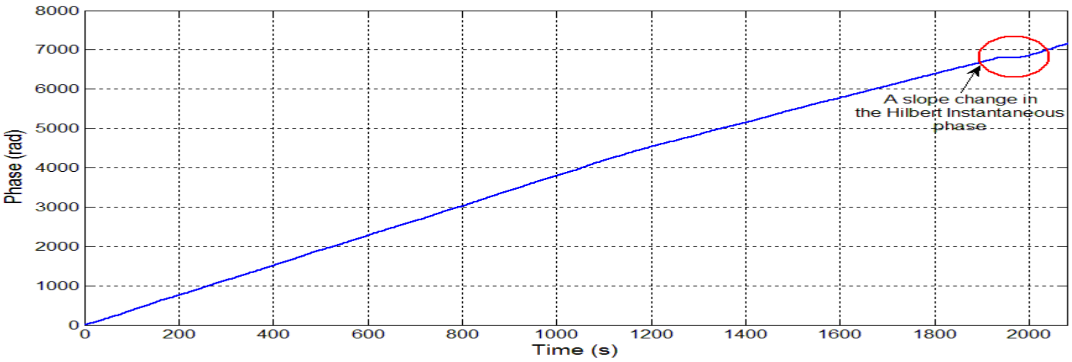

**Figure 6.18** Hilbert instantaneous phase for the fourth IMF including the predicted damage point

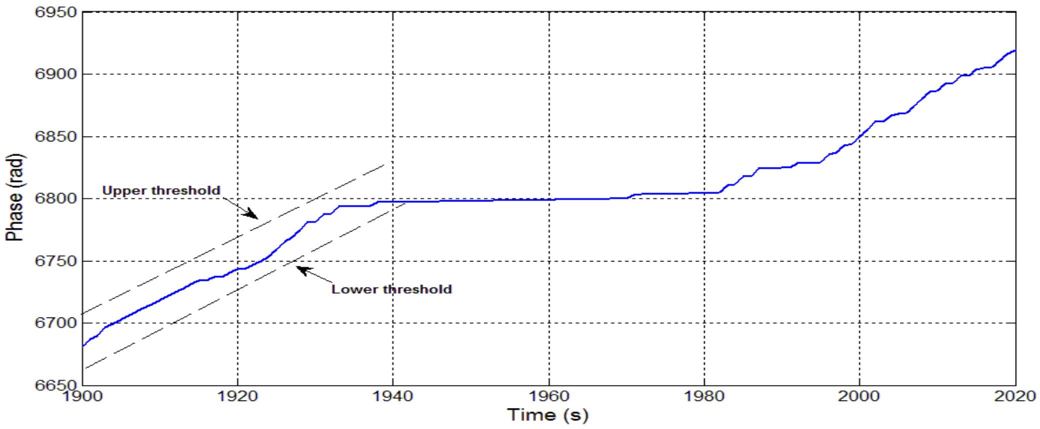

**Figure 6.19** A zooming window of Hilbert instantaneous phase for the fourth IMF

From Figure 6.18, it is clear that the predicted change point is occurred at time step equal to 1933, which means that the damage is predicted to occur after 3 seconds delay. Each simulation has been replicated 30 times to ensure the accuracy of the predicted time delay.

*Performance evaluation using average run length and mean delay of damage detection*

The performance evaluation of the proposed damage detection method is demonstrated using mean time delay and compared with wavelet analysis at different levels of noise as shown in Table 6.11 and Table 6.12.

**Table 6.11** Comparison results between the proposed method and Morlet wavelet for the data with low level noise (NSR of 5%) for all six different damage patterns

| **Operating condition** | **Mean delay (MWC)** | **Mean delay (the proposed method)** |
|---|---|---|
| Very slight damaged<br>Patterns 6 and 3 | P 6: $\bar{\tau}$= 16.21<br>P 3: $\bar{\tau}$= 3.35 | P 6: $\bar{\tau}$= 13.72<br>P 3: $\bar{\tau}$= 3.01 |
| Medium locally damaged<br>Patterns 4 and 5 | P 4: $\bar{\tau}$= 1.88<br>P 5: $\bar{\tau}$= 1.85 | P 4: $\bar{\tau}$= 1.04<br>P 5: $\bar{\tau}$= 1.03 |
| Severe damaged<br>Patterns 1 and 2 | P 1: $\bar{\tau}$= 1.29<br>P 2: $\bar{\tau}$= 1.27 | P 1: $\bar{\tau}$= 1.06<br>P 2: $\bar{\tau}$= 1.02 |

**Table 6.12** Comparison results between the proposed method and Morlet wavelet for the data with high level noise (NSR of 20%) for all six different damage patterns

| **Operating condition** | **Mean delay (MWC)** | **Mean delay (the proposed method)** |
|---|---|---|
| Very slight damaged<br>Patterns 6 and 3 | P 6: $\bar{\tau}$= 168.81<br>P 3: $\bar{\tau}$= 143.74 | P 6: $\bar{\tau}$= 42.1<br>P 3: $\bar{\tau}$= 27.62 |
| Medium locally damaged<br>Patterns 4 and 5 | P 4: $\bar{\tau}$= 22.51<br>P 5: $\bar{\tau}$= 14.98 | P 4: $\bar{\tau}$= 6.3<br>P 5: $\bar{\tau}$= 6.7 |
| Severe damaged<br>Patterns 1 and 2 | P 1: $\bar{\tau}$= 3.11<br>P 2: $\bar{\tau}$= 3.19 | P 1: $\bar{\tau}$= 2.07<br>P 2: $\bar{\tau}$= 2.05 |

The comparison indicates clearly that the proposed damage detection method do outperform the WEWMA control charts. In other words, it captures the damage earlier than the Morlet wavelet based damage feature, especially with a very slight damage and high level of noise.

*Energy index of the selected IMF for damage severity prediction*

To predict the damage severity of the benchmark structure, the proposed quantitative relative energy index (REDI) presented in section 6.5.3 is compared with the percent loss in stiffness of the 12-DOF models as shown in Table 6.13. The comparison indicates that the proposed prediction method captures the loss in stiffness of the structure, and thus effectively differentiates the normal condition with different levels of damage.

**Table 6.13** Comparison between the proposed relative energy damage index and percent loss in stiffness of 12 degree of freedom shear-building models

| **Damage patterns** | **1** | **2** | **3** | **4** | **5** | **6** |
|---|---|---|---|---|---|---|
| REDI (Representative IMF) | 20.32% | 34.60% | 2.93% | 5.37% | 5.19% | 0.71% |
| Percent loss in stiffness [76] | 30% | 60% | 5.6% | 10.2% | 11.3% | 2.3% |

In this case study, the existence of damage of the underlying dynamic system is accurately detected using the slope change of the Hilbert instantaneous phase of the most sensitive IMF within all candidates, after trying them all simultaneously. The severity of structural damage is predicted using the energy of the predicted part of the selected IMF.

## 6.7 Summary

In this study, an efficient methodology for prediction based change point detection has been developed for online structural health monitoring (SHM). Within each adaptive sliding window, the proposed method performs the sifting process in the EMD using piecewise Hermit interpolation. The EMD based online prediction applies the locally weighted linear predictor and consists of two steps: 1) change point detection using Hilbert instantaneous phase; 2) and damage severity prediction using the energy index of the most representative IMF. The case studies indicate that: 1) the proposed boundary distortion processing method for EMD has achieved a significant reduction in the boundary effects; 2) moreover, the damage existence of the underlying dynamic system is accurately detected with a minimum time delay using the slope change of the Hilbert instantaneous phase; and 3) it is also demonstrated that the proposed relative energy damage index (REDI) based on the energy changes of the selected IMF has the capability to effectively predict different levels of damage.

# REFERENCE

1. Sohn, H., et al., *A review of structural health monitoring literature: 1996-2001*. 2004: Los Alamos National Laboratory Los Alamos,, New Mexico.

2. Sohn, H., et al., *Structural health monitoring using statistical pattern recognition techniques.* Journal of dynamic systems, measurement, and control, 2001. **123**: p. 706.

3. Vincent, H., S. Hu, and Z. Hou. *Damage detection using empirical mode decomposition method and a comparison with wavelet analysis*. 1999.

4. Zemmour, A.I., *The Hilbert-Huang transform for damage detection in plate structures*, in *aerospace engineering*. 2006, University Of Maryland: New York.

5. Huang, N.E., et al., *The empirical mode decomposition and the Hilbert spectrum for nonlinear and nonstationary time series analysis.* Proceedings of the Royal Society of London. Series A: Mathematical, Physical and Engineering Sciences, 1998. **454**(1971): p. 903-995.

6. Yang, J.N., et al., *System identification of linear structures based on Hilbert–Huang spectral analysis. Part 1: Normal modes.* Earthquake engineering & structural dynamics, 2003. **32**(9): p. 1443-1467.

7. Tua, P., S. Quek, and Q. Wang, *Detection of cracks in plates using piezo-actuated Lamb waves.* Smart Materials and Structures, 2004. **13**(4): p. 643.

8. Yang, J.N., et al., *Hilbert-Huang based approach for structural damage detection.* Journal of engineering mechanics, 2003. **130**(1): p. 85-95.

9. Huang, N.E., et al., *The empirical mode decomposition and the Hilbert spectrum for nonlinear and nonstationary time series analysis.* Proceedings of the Royal Society of London. Series A: Mathematical, Physical and Engineering Sciences, 1998. **454**(1971): p. 903-995.

10. Wang, J., X.F. Zhong, and X.Y. Peng. *Deal with boundary effect of EMD method based on improved Characteristic Wave Extending*. 2010: IEEE.

11. Qi, K., Z. He, and Y. Zi, *Cosine window-based boundary processing method for EMD and its application in rubbing fault diagnosis.* Mechanical Systems and Signal Processing, 2007. **21**(7): p. 2750-2760.

12. Zeng, K. and M.X. He. *A simple boundary process technique for empirical mode decomposition*. 2004: IEEE.

13. Parey, A. and R.B. Pachori, *Variable cosine windowing of intrinsic mode functions: Application to gear fault diagnosis.* Measurement, 2011.

14. Rilling, G., P. Flandrin, and P. Gonçalvés. *On empirical mode decomposition and its algorithms*. 2003.

15. Huang, N.E., *Empirical mode decomposition apparatus, method and article of manufacture for analyzing biological signals and performing curve fitting*. 2004, Google Patents.

16. Lee, C.Y. and Y. Lee, *BPNN Based Processing for End Effects of HHT.* World Academy of Science, Engineering and Technology, 2010. **72**.

17. Deng, Y., et al., *Boundary-processing-technique in EMD method and Hilbert transform.* Chinese Science Bulletin, 2001. **46**(11): p. 954-960.

18. Rumelhart, D.E., G.E. Hintont, and R.J. Williams, *Learning representations by back-propagating errors*. Nature, 1986. **323**(6088): p. 533-536.

19. Zhong, C. and Z. Shixiong, *Analysis on end effects of EMD method.* Journal of Data Acquisition and Processing, 2003. **18**(1): p. 114-118.

20. Butland, J., *A method of interpolating reasonable-shaped curves through any data.* Proc. Computer Graphics, 1980. **80**: p. 409-422.

21. De Boor, C., *A practical guide to splines*. 1978.

22. Wolberg, G. and I. Alfy, *An energy-minimization framework for monotonic cubic spline interpolation.* Journal of Computational and Applied Mathematics, 2002. **143**(2): p. 145-188.

23. Fritsch, F.N. and R.E. Carlson, *Monotone piecewise cubic interpolation.* SIAM Journal on Numerical Analysis, 1980. **17**(2): p. 238-246.

24. Riemenschneider, S., et al., *B-spline based empirical mode decomposition.* Hilbert–Huang Transform and its Applications (Interdisciplinary Mathematical Sciences), 2005. **5**: p. 27-56.

25. Chen, Q., et al., *A B-spline approach for empirical mode decompositions.* Advances in Computational Mathematics, 2006. **24**(1): p. 171-195.

26. Knott, G.D., *Interpolating cubic splines*. Vol. 18. 2000: Birkhauser.

27. Meeson, R.N., *HHT sifting and adaptive filtering*. 2003, DTIC Document.

28. Kincaid, D.R. and E.W. Cheney, *Numerical analysis: mathematics of scientific computing*. Vol. 2. 2002: Amer Mathematical Society.

29. Wang, Y., *Improvements of approximation of the local mean in the process of empirical mode decomposition*. 2006, University of Alberta.

30. Wang, Y., et al., *Improvement of local mean approximation in empirical mode decomposition for gear fault detection.* Eksploatacja i Niezawodność–Maintenance and Reliability, 2010. **2**: p. 59-66.

31. Chang, N.F., et al. *On-line empirical mode decomposition biomedical microprocessor for Hilbert Huang transform*. in *Biomedical Circuits and Systems Conference (BioCAS), 2011 IEEE*. 2011: IEEE.

32. Shi, C. and Q. Luo, *Hilbert-Huang transform and wavelet analysis of time history signal.* Acta Seismologica Sinica, 2003. **16**(4): p. 422-429.

33. Ayenu-Prah, A. and N. Attoh-Okine, *Comparative study of Hilbert–Huang transform, Fourier transform and wavelet transform in pavement profile analysis.* Vehicle System Dynamics, 2009. **47**(4): p. 437-456.

34. Guangshu, H., *Digital signal processing—theory, algorithm and realization (the second edition)*. 2003, Beijing: Tsinghua University Press.

35. Huang, N.E. and Z. Wu, *A review on Hilbert-Huang transform: Method and its applications to geophysical studies.* Reviews of Geophysics, 2008. **46**(2): p. 1-23.

36. Rato, R., M. Ortigueira, and A. Batista, *On the HHT, its problems, and some solutions.* Mechanical Systems and Signal Processing, 2008. **22**(6): p. 1374-1394.

37. Cheney, E.W. and D.R. Kincaid, *Numerical mathematics and computing*. 2007: Brooks/Cole Pub Co.

38. Mode, R. E. *School of Engineering and Phisical Science*. 2010, James cook university .

39. Sa-ngasoongsong, A. and S.T.S. Bukkapatnam, *Willingness-to-pay Prediction Based on Empirical Mode Decomposition.*

40. Ewing, G.M., *Calculus of variations with applications*. 1985: Dover publications.

41. Bliss, G.A., *Calculus of variations.* Bull. Amer. Math. Soc. 31 (1925), 551-554. DOI: 10.1090/S0002-9904-1925-04110-5 PII: S, 1925. **2**(9904): p. 04110-5.

42. O'Haver, T. *An Introduction to Signal Processing with Applications in Chemical Analysis*. 2012 September 10, 2012 [cited 2012; Available from: http://terpconnect.umd.edu/~toh/spectrum/TOC.html.

43. Wei, Y. and M.C. Chen, *Forecasting the short-term metro passenger flow with empirical mode decomposition and neural networks.* Transportation Research Part C: Emerging Technologies, 2012. **21**(1): p. 148-162.

44. Haskell, N., *Total energy and energy spectral density of elastic wave radiation from propagating faults: part II. A statistical source model*. Vol. 30. 1990: American Geophysical Union.

45. Eckmann, J.P., S.O. Kamphorst, and D. Ruelle, *Recurrence plots of dynamical systems.* EPL (Europhysics Letters), 1987. **4**: p. 973.

46. Webber Jr, C.L. and J.P. Zbilut, *Recurrence quantification analysis of nonlinear dynamical systems.* Tutorials in contemporary nonlinear methods for the behavioral sciences, 2005: p. 26-94.

47. Ahmed, N.K., et al., *An empirical comparison of machine learning models for time series forecasting.* Econometric Reviews, 2010. **29**(5-6): p. 594-621.

48. Guo, H., K. Paynabar, and J. Jin, *Multiscale monitoring of autocorrelated processes using wavelets analysis.* IIE Transactions, 2012. **44**(4): p. 312-326.

49. Pines, D. and L. Salvino, *Structural health monitoring using empirical mode decomposition and the Hilbert phase.* Journal of sound and vibration, 2006. **294**(1): p. 97-124.

50. Salvino, L. and D. Pines. *Structural damage detection using empirical mode decomposition and HHT*. 2002.

51. Jha, R., et al. *Experimental evaluation of instantaneous phase-based index for structural health monitoring*. 2006: International Society for Optics and Photonics.

52. Johnson, e., et al., *Phase I IASC-ASCE structural health monitoring benchmark problem using simulated data.* Journal of Engineering Mechanics, 2004. **130**(1): p. 3-15.

53. Yan, R. and R.X. Gao, *Hilbert–Huang transform-based vibration signal analysis for machine health monitoring.* Instrumentation and measurement, IEEE Transactions on, 2006. **55**(6): p. 2320-2329.

54. Chicken, E., J.J. Pignatiello Jr, and J.R. Simpson, *Statistical process monitoring of nonlinear profiles using wavelets.* Journal of Quality Technology, 2009. **41**(2): p. 198-212.

55. Jeong, M.K., J.C. Lu, and N. Wang, *Wavelet-based SPC procedure for complicated functional data.* International Journal of Production Research, 2006. **44**(4): p. 729-744.

56. Jin, J. and J. Shi, *Automatic feature extraction of waveform signals for in-process diagnostic performance improvement.* Journal of Intelligent Manufacturing, 2001. **12**(3): p. 257-268.

57. Pandit, S.M. and S.M. Wu, *Time series and system analysis with applications*. 1990, New York: RE Krieger Pub. Co.

58. Montgomery, D.C. and R. Gerth, *Introduction to statistical quality control.* IIE Transactions, 1998. **30**(6): p. 571.

59. Nair, K.K. and A.S. Kiremidjian, *A damage detection algorithm using the Morlet wavelet transform.* ASCE Journal of engineering mechanics, in review., 2009.

60. Task-group. *ASCE benchmark structure*. ASCE-SHM 2004 [cited 2012 May, 20th ]; Available from: http://wusceel.cive.wustl.edu/asce.shm/). .

61. Peng, Z., P.W. Tse, and F. Chu, *A comparison study of improved Hilbert–Huang transform and wavelet transform: application to fault diagnosis for rolling bearing.* Mechanical Systems and Signal Processing, 2005. **19**(5): p. 974-988.

62. Zhang, Y. and Z. Ye, *Short-term traffic flow forecasting using fuzzy logic system methods.* Journal of Intelligent Transportation Systems, 2008. **12**(3): p. 102-112.

63. Balestrassi, P., et al., *Design of experiments on neural network's training for nonlinear time series forecasting.* Neurocomputing, 2009. **72**(4): p. 1160-1178.

# CHAPTER VII

# CONCLUSIONS AND FUTURE WORK

This dissertation is focused on nonlinear and nonstationary dynamic modeling and analysis for online Structural Health Monitoring towards the diagnostic and prognostic applications. Three related research tasks for the online Structural Health Monitoring are studied, namely, sensor placement optimization for SHM; damage detection for SHM, and damage prediction. The major conclusions are presented, followed with future work recommendations.

## 7.1 Conclusions

A partial differential equation (PDE) model is formulated and solved to predict the horizontal dynamic response of the structure when subjected to horizontal forced excitations. The proposed PDE model has been validated with experimental results using correlation analysis with percentage error (< 10%). This method expands the displacement functions to form a stochastic random field of the building vibration. Based on this PDE formulation and Fisher information matrix, an optimal sensor placement method for damage detection in multistory buildings is presented. The proposed method minimizes the uncertainty in parameter estimation in the differential equations modeling; enable the extracted modals to be more robust to operational and environmental noise. Moreover, this sensor placement optimization method can reduce not only the number of sensors, but also the delay of damage detection.

A novel quasi-recursive correlation dimension (QRCD) analysis is also developed for online detection of structural damages. The QRCD algorithm can significantly alleviate the complexity of computation for correlation dimension to approximate O(N), making the online monitoring of nonlinear/nonstationary processes using correlation dimension much more applicable and efficient. The numerical results indicate the superiority of the proposed method over the G-P standard correlation dimension algorithm by significantly reducing the computational complexity in terms of CPU time by at least 60% (for different levels of damage). Moreover, results show a shorter average run length ($ARL_1$) than Morlet wavelet coefficients, indicating a better detection performance for the proposed QRCD in capturing various process changes and different levels of damage.

In order to track structural integrity and ensure safe and reliable systems, an advanced prediction modeling for structural damage is developed based on modified Empirical Mode Decomposition (EMD). The proposed damage prediction methodology overcomes the boundary effects of the sifting process, making the online monitoring and prediction of the underlying process much more accurate. The proposed SHM prediction scheme consists of two steps: change point detection using Hilbert instantaneous phase prediction and damage severity estimation using the energy index of the most representative intrinsic mode function (IMF). Case studies results yield significant prediction accuracy improvement (> 30%) over other commonly used prediction techniques. In addition, it is also demonstrated that the proposed relative energy damage index (REDI) based on the energy changes of the selected IMF has the capability to effectively differentiate different levels of damage.

## 7.2 Future works

Aiming at developing an integrated approach to Structural Health Monitoring and prognosis framework, some improvements and future work directions are suggested as follows.

First, in the present study, horizontal dynamic response of the multistory buildings when subjected to horizontal forced excitations is studied using partial differential equation modeling. An improvement would be to integrate the vertical dynamic response with the current PDE model subjected to both forced and ambient excitations, which will improve the accuracy for the real world applications.

Second, the online damage detection method using quasi-recursive correlation dimension algorithm showed very promising results for the numerically simulated datasets of the American Society of Civil Engineers' (ASCE) benchmark structure. However, this applicability of the proposed method should be verified when applied to real structures.

Third, the damage detection schemes developed in this dissertation efficiently detect and quantify the structural damage. However, they did not provide a way to infer the location of the damage. Thus, another important component of the future work is to investigate the damage localization. This would give a more comprehensive practical structural health assessment.

Finally, in this dissertation, a data driven Empirical Mode Decomposition technique is developed for damage prognosis using locally weighted linear predictor. It is expected to obtain more robust and accurate results if we fuse results from different prediction techniques.

# APPENDICES

## Appendix A

In this appendix, the mathematical derivation of the equivalent ordinary differential equation system (ODES) to the partial differential Equation (4.2) is presented in Appendix A1. Then, the analytical solution of the proposed ordinary differential system (Equation (4.21) is shown in Appendix A2. The eigenvalue parameter calculation, corresponding to the mode of vibration is shown in Appendix A3. Finally, the formulation of the Jacobian matrix of the acceleration is shown in Appendix A4.

### A1 Equivalent ordinary differential equation system

Recall the partial differential equation (Equation (4.2)) that describes the overall lateral affine deformation of the benchmark structure when subjected to horizontal roof excitation,

$$\frac{\rho(z)}{EI_1}\left(\frac{\partial^2 u(x,y,z,t)}{\partial t^2}+c(z)\frac{\partial u(x,y,z,t)}{\partial t}\right)+\frac{1}{H^4}\frac{\partial^2}{\partial z^2}\left(S_1(z)\frac{\partial^2 u(x,y,z,t)}{\partial z^2}\right)-\frac{\alpha_0^2}{H^4}\frac{\partial}{\partial z}\left(S_2(z)\frac{\partial u(x,y,z,t)}{\partial z}\right)=$$
$$-\frac{\rho(z)}{EI_1}\frac{\partial^2}{\partial t^2}f_e(t) \tag{A1.1}$$

where $\rho(z)$; is the mass per unit length in the underlying model; $u(x,y,z,t)$ represents the lateral displacement at height *z* at time *t* and spatial domain *(x,y);* $c(z)$ is the damping coefficient per unit length; $EI_1$ is the flexural rigidity of the flexural beam at the base of the structure; $H$ is the total height of the multistory building;; $z \in \{0.9,1.8,2,7,3.6\}$ $and\ x = y \in [0,2.5]$ represent the height and the symmetric dimensions of the benchmark structure's four floors, respectively; $f_e(t)$ is the forced excitation function.

For the case of undammed free vibration, Equation (A1.1) becomes,

$$\frac{\rho(z)}{EI_1}\frac{\partial^2 u(x,y,z,t)}{\partial t^2} + \frac{1}{H^4}\frac{\partial^2}{\partial z^2}\left(S_1(z)\frac{\partial^2 u(x,y,z,t)}{\partial z^2}\right) - \frac{\alpha_0^2}{H^4}\frac{\partial}{\partial z}\left(S_2(z)\frac{\partial u(x,y,z,t)}{\partial z}\right) = 0 \tag{A1.2}$$

Using the method of separation of variables in the lateral displacement equation given by,

$$u_i(x,y,z,t) = \mathit{\Gamma}_i \phi_i(x,y,z) D_i(t) \tag{A1.3}$$

Then, the first and second derivative of Equation (A1.3) with respect to *z* and *t* are as follows,

$$\frac{\partial}{\partial t} u_i(x,y,z,t) = \mathit{\Gamma}_i \phi_i(x,y,z) \frac{\partial}{\partial t} D_i(t) \tag{A1.4}$$

$$\frac{\partial^2}{\partial t^2} u_i(x,y,z,t) = \mathit{\Gamma}_i \phi_i(x,y,z) \frac{\partial^2}{\partial t^2} D_i(t) \tag{A1.5}$$

$$\frac{\partial}{\partial z} u_i(x,y,z,t) = \mathit{\Gamma}_i D_i(t) \frac{\partial}{\partial z} \phi_i(x,y,z) \tag{A1.6}$$

$$\frac{\partial^2}{\partial z^2} u_i(x,y,z,t) = \mathit{\Gamma}_i D_i(t) \frac{\partial^2}{\partial z^2} \phi_i(x,y,z) \tag{A1.7}$$

Substituting Equations (A1.4- A1.7) into Equation (A1.2), we get

$$\begin{gathered}\frac{\rho(z)}{EI_1}\mathit{\Gamma}_i \phi_i(x,y,z)\frac{\partial^2}{\partial t^2} D_i(t) + \frac{1}{H^4}\frac{\partial^2}{\partial z^2}\left(S_1(z)\mathit{\Gamma}_i D_i(t)\frac{\partial^2}{\partial z^2}\phi_i(x,y,z)\right) - \\ \frac{\alpha_0^2}{H^4}\frac{\partial}{\partial z}\left(S_2(z)\mathit{\Gamma}_i D_i(t)\frac{\partial}{\partial z}\phi_i(x,y,z)\right) = 0\end{gathered} \tag{A1.8}$$

Dividing Equation (A1.8) by $\mathit{\Gamma}_i \phi_i(x,y,z) D_i(t)$, gives the following equation,

$$\frac{\rho(z)}{EI_1}\frac{1}{D_i(t)}\frac{\partial^2}{\partial t^2} D_i(t) = -\frac{1}{H^4}\frac{\partial^2}{\phi_i(x,y,z)\partial z^2}\left(S_1(z)\frac{\partial^2}{\partial z^2}\phi_i(x,y,z)\right) + \frac{\alpha_0^2}{H^4}\frac{\partial}{\phi_i(x,y,z)\partial z}\left(S_2(z)\frac{\partial}{\partial z}\phi_i(x,y,z)\right) \tag{A1.9}$$

And,

$$\frac{1}{D_i(t)}\frac{\partial^2}{\partial t^2} D_i(t) = \frac{EI_1}{H^4\rho(z)}\left[-\frac{\partial^2}{\phi_i(x,y,z)\partial z^2}\left(S_1(z)\frac{\partial^2}{\partial z^2}\phi_i(x,y,z)\right) + \frac{\alpha_0^2}{\phi_i(x,y,z)}\frac{\partial}{\partial z}\left(S_2(z)\frac{\partial}{\partial z}\phi_i(x,y,z)\right)\right] \tag{A1.10}$$

Assume Equation (A1.10) equals $-\omega_i^2$, then from first and last ratios, we have

$$\frac{1}{D_i(t)}\frac{\partial^2}{\partial t^2}D_i(t) = -\omega_i^2$$

which gives the following equation,

$$\frac{d^2 D_i(t)}{dt^2} + \omega_i^2 D_i(t) = 0$$

From second and last ratios, we get the following Equation,

$$-\frac{\partial^2}{\phi_i(x,y,z)\partial z^2}\left(S_1(z)\frac{\partial^2}{\partial z^2}\phi_i(x,y,z)\right) + \frac{\alpha_0^2}{\phi_i(x,y,z)}\frac{\partial}{\partial z}\left(S_2(z)\frac{\partial}{\partial z}\phi_i(x,y,z)\right) = -\omega_i^2\ \frac{EI_1}{H^4\rho(z)} \tag{A1.11}$$

Multiplying Equation (A1.11) by $-\phi_i(x,y,z)$ to get the required Equation

$$\frac{\partial^2}{\partial z^2}\left(S_1(z)\frac{\partial^2}{\partial z^2}\phi_i(x,y,z)\right) - \alpha_0^2\frac{\partial}{\partial z}\left(S_2(z)\frac{\partial}{\partial z}\phi_i(x,y,z)\right) - \omega_i^2\ \frac{H^4\rho(z)}{EI_1}\phi_i(x,y,z) = 0$$

## A2 Analytical solution of the ordinary differential system

In what follows, we show that the mode shape in Equation (4.17) is the closed form solution of the simplified ordinary differential equation given by,

$$\frac{d^4\phi_i(z)}{dz^4} - \beta^4\phi_i(z) = 0 \tag{A2.1}$$

where, $\beta^4 = \frac{\rho(z)\omega_i^2}{EI}$, Equation (A2.1) is a 4th order homogeneous ordinary differential equation with constant coefficients. Thus, we seek a solution as $\phi_i(z) = e^{rz}$. The characteristic equation for the above equation is given by,

$$r^4 - {\beta_i}^4 = 0$$

$$\left(r^2 - {\beta_i}^2\right)\left(r^2 + {\beta_i}^2\right) = 0$$

Accordingly, $r = \pm\beta_i$ , $r = \pm\beta_i \mathrm{i}$ and the general solution is

$$\phi_i(z) = C_1 e^{\beta_i z} + C_2 e^{-\beta_i z} + C_3 e^{i\beta_i z} + C_4 e^{-\mathrm{i}\beta_i z} \tag{A2.2}$$

Recall that $\cos z = \frac{e^{iz}+e^{-iz}}{2}$, $\sin z = \frac{e^{iz}-e^{-iz}}{2i}$, $\cosh z = \frac{e^{z}+e^{-z}}{2}$ and $\sinh z = \frac{e^{z}-e^{-z}}{2}$ , then Equation (A2.2) can be written as,

$$\phi_i(z) = C_1 \sin(\beta_i z) + C_2 \cos(\beta_i z) + C_3 \sin\mathrm{h}(\beta_i z) + C_4 \cosh(\beta_i z) \tag{A2.3}$$

We need to obtain the values of the constants using the initial conditions (Equation (4.14)). To do this, we first apply $\phi_i(z)$=0 at z=0, which implies that $C_4 = -C_2$, then applying $\frac{d\phi_i(z)}{dz} = 0$ to the equation (A2.3) gives $C_3 = -C_1$

Recall that,

$$\frac{d^2\phi_i(z)}{dz^2} = -C_1 \beta_i^{\,2} \sin(\beta_i z) - C_2 \beta_i^{\,2} \cos(\beta_i z) + C_3 \beta_i^{\,2} \sin\mathrm{h}(\beta_i z) + C_4 \beta_i^{\,2} \cosh(\beta_i z)$$

$$\frac{d^3\phi_i(z)}{dz^3} = -C_1 \beta_i^{\,3} \cos(\beta_i z) + C_2 \beta_i^{\,3} \sin(\beta_i z) + C_3 \beta_i^{\,3} \cos\mathrm{h}(\beta_i z) + C_4 \beta_i^{\,3} \sinh(\beta_i z)$$

Then, applying the boundary conditions (Equation (4.15)), we have

$$EI\left(-C_1 \beta_i^{\,2} \sin(\beta_i z) - C_2 \beta_i^{\,2} \cos(\beta_i z) + C_3 \beta_i^{\,2} \sin\mathrm{h}(\beta_i z) + C_4 \beta_i^{\,2} \cosh(\beta_i z)\right) = 0 \tag{A2.4}$$

And,

$$EI\left(-C_1 \beta_i^{\,3} \cos(\beta_i z) + C_2 \beta_i^{\,3} \sin(\beta_i z) + C_3 \beta_i^{\,3} \cos\mathrm{h}(\beta_i z) + C_4 \beta_i^{\,3} \sinh(\beta_i z))\right) = 0 \tag{A2.5}$$

Since $C_4 = -C_2$ and $C_3 = -C_1$ and z=3.6, then Equation (A2.4) becomes,

$$C_1\left(\sin(3.6\beta_i) + \sin\mathrm{h}(3.6\beta_i)\right) + C_2\left(\cos(3.6\beta_i) + \cos\mathrm{h}(3.6\beta_i)\right) = 0 \tag{A2.6}$$

And Equation (A2.5) gives,

$$C_1\left(\cos(3.6\beta_i) + \cos\mathrm{h}(3.6\beta_i)\right) + C_2\left(-\sin(3.6\beta_i) + \sin\mathrm{h}(3.6\beta_i)\right) = 0 \tag{A2.7}$$

Now, substitute Equation (A2.6) into Equation (A2.2) gives,

$$\phi_i(z) = -\mathrm{C}_2 \frac{\cosh(3.6\beta_i)+\cos(3.6\beta_i)}{\sinh(3.6\beta_i)+\sin(3.6\beta_i)} \left(\sin(\beta_i z) - \sinh(\beta_i z)\right) + \mathrm{C}_2\left(\cos(\beta_i z) - \cosh(\beta_i z)\right)$$

$$= -\mathrm{C}_2 \left[\left(\cosh(\beta_i z) - \cos(\beta_i z)\right) - \frac{\cosh(3.6\beta_i)+\cos(3.6\beta_i)}{\sinh(3.6\beta_i)+\sin(3.6\beta_i)} \left(\sinh(\beta_i z) - \sin(\beta_i z)\right)\right]$$

From Appendix A3, the system has infinitely many solutions, so taking $\mathrm{C}_2$ to be -1, gives the required equation,

$$\phi_i(z) = \left(\cosh(\beta_i z) - \cos(\beta_i z)\right) - \frac{\cosh(3.6\beta_i)+\cos(3.6\beta_i)}{\sinh(3.6\beta_i)+\sin(3.6\beta_i)} \left(\sinh(\beta_i z) - \sin(\beta_i z)\right)$$

## A3 Calculating the eigenvalue parameters using the characteristic equation

Recall Equation (A2.6) and Equation (A2.7) from Appendix A2

$$C_1\left(\sin(3.6\beta_i) + \sin h(3.6\beta_i)\right) + C_2\left(\cos(3.6\beta_i) + \cos h(3.6\beta_i)\right) = 0 \qquad \text{(A3.1)}$$

$$C_1\left(\cos(3.6\beta_i) + \cos h(3.6\beta_i)\right) + C_2\left(-\sin(3.6\beta_i) + \sin h(3.6\beta_i)\right) = 0 \qquad \text{(A3.2)}$$

Equation (A3.1) and Equation (A3.2) can be written in a matrix form as

$$\begin{bmatrix} \sin(3.6\beta_i) + \sin h(3.6\beta_i) & \cos(3.6\beta_i) + \cos h(3.6\beta_i) \\ \cos(3.6\beta_i) + \cos h(3.6\beta_i) & -\sin(3.6\beta_i) + \sin h(3.6\beta_i) \end{bmatrix} \begin{bmatrix} C_1 \\ C_2 \end{bmatrix} = \begin{bmatrix} 0 \\ 0 \end{bmatrix}$$

For the non-trivial solution, the determinate of the coefficient matrix must be zero as follows

$$\begin{vmatrix} \sin(3.6\beta_i) + \sin h(3.6\beta_i) & \cos(3.6\beta_i) + \cos h(3.6\beta_i) \\ \cos(3.6\beta_i) + \cos h(3.6\beta_i) & -\sin(3.6\beta_i) + \sin h(3.6\beta_i) \end{vmatrix} = 0$$

That is,

$$\sin^2(3.6\beta_i) + \sin(3.6\beta_i)\sin h(3.6\beta_i) - \sin(3.6\beta_i)\sin h(3.6\beta_i) + \sin h^2(3.6\beta_i) - \cos^2(3.6\beta_i) \\ - \cos(3.6\beta_i) + \cos h(3.6\beta_i) - \cos(3.6\beta_i) + \cos h(3.6\beta_i) - \cosh^2(3.6\beta_i)$$

This leads to the following equation,

$$1 + \cos(3.6\beta_i)\cos h(3.6\beta_i) = 0$$

where, $\beta_i \cong 0.5208$, 1.3039 and 2.1819, are the numerical solutions for *i*= 1, 2, 3 respectively.

## A4 Formulation of the Jacobian matrix of the Acceleration

Recall Equation (4.7) and Equation (4.8),

$$u(z,t) = \sum_{i=1}^{3} u_i(z,t) = \sum_{i=1}^{3} \Gamma_i\, \phi_i(z) D_i(t)_x \tag{A4.1}$$

$$v(z,t) = \sum_{i=1}^{3} v_i(z,t) = \sum_{i=1}^{3} \Gamma_i\, \phi_i(z) D_i(t)_y \tag{A4.2}$$

where, $\Gamma_i = \frac{\int_0^1 \phi_i(z)dz}{\int_0^1 \phi_i^2(z)dz}$, Moreover, recall the displacement functions (Equation (4.10) and Equation (4.11)),

$$u(x,y,z) = u_0(z) + xu_1(z) + x^2 u_2(z) \tag{A4.3}$$

$$v(x,y,z) = v_0(z) + yv_1(z) + y^2 v_2(z) \tag{A4.4}$$

where, $u_0(z) = \sum_{i=1}^{3} \Gamma_i\, \phi_i(z) D_i(t)_x$ ; $u_1(z)$ and $u_2(z)$ are the first and second derivative of $u_0(z)$, respectively. And, $v_0(z) = \sum_{i=1}^{3} \Gamma_i\, \phi_i(z) D_i(t)_y$; $v_1(z)$ and $v_2(z)$ are the first and second derivative of $v_0(z)$, respectively.

The Jacobian matrix of the multistory structure vibration is the first derivative of the acceleration with respect to each sensor location. Then, first we need to find the acceleration in *x*-direction as well as in *y*-direction.

Substituting Equation (A4.1) into Equation (A4.3) leads to the following equation,

$$u(x,y,z) = \sum_{i=1}^{3} \Gamma_i\, \phi_i(z) D_i(t)_x + x \sum_{i=1}^{3} D_i(t)_x \left[ \frac{\int_0^1 \phi_i(z)dz}{\int_0^1 \phi_i^2(z)dz} \frac{d\phi_i(z)}{dz} + 1 \right] + x^2 \sum_{i=1}^{3} D_i(t)_x \left[ \frac{\int_0^1 \phi_i(z)dz}{\int_0^1 \phi_i^2(z)dz} \frac{d^2\phi_i(z)}{dz^2} + \frac{d\phi_i(z)}{dz} \frac{1}{\phi_i(z)} \right] \tag{A4.5}$$

$$= \sum_{i=1}^{3} D_i(t)_x \left[ \Gamma_i \phi_i(z) + x(\Gamma_i \phi_i(z) + 1) + x^2 \left( \Gamma_i \frac{d^2\phi_i(z)}{dz^2} + \frac{d\phi_i(z)}{dz} \frac{1}{\phi_i(z)} \right) \right] \tag{A4.6}$$

Now taking the first and second derivative of Equation (A4.6) gives,

$$\dot{u}(x,y,z,t) = \sum_{i=1}^{3} \dot{D}_i(t)_x \left[ \Gamma_i \phi_i(z) + x(\Gamma_i \phi_i(z) + 1) + x^2 \left( \Gamma_i \frac{d^2\phi_i(z)}{dz^2} + \frac{d\phi_i(z)}{dz} \frac{1}{\phi_i(z)} \right) \right] \tag{A4.7}$$

$$\ddot{u}(x,y,z,t) = \sum_{i=1}^{3} \ddot{D}_i(t)_x \left[ \Gamma_i \phi_i(z) + x(\Gamma_i \phi_i(z) + 1) + x^2 \left( \Gamma_i \frac{d^2\phi_i(z)}{dz^2} + \frac{d\phi_i(z)}{dz} \frac{1}{\phi_i(z)} \right) \right] \tag{A4.8}$$

Similarly, the acceleration in y-direction is given by,

$$\ddot{v}(x,y,z,t) = \sum_{i=1}^{3} \ddot{D}_{\imath}(t)_y \left[\Gamma_i\phi_i(z) + y(\Gamma_i\phi_i(z) + 1) + y^2 \left(\Gamma_i \frac{d^2\phi_i(z)}{dz^2} + \frac{d\phi_i(z)}{dz}\,\frac{1}{\phi_i(z)}\right)\right] \quad \text{(A4.9)}$$

Since the Jacobian matrix of the multistory structure vibration is the first derivative of the acceleration with respect to each sensor location, then, the first derivative of Equation (A4.8) with respect to *x* is given below,

$$\frac{\partial\ddot{u}(x,y,z,t)}{\partial x} = \sum_{i=1}^{3} \ddot{D}_{\imath}(t)_x \left[1 + \Gamma_i\phi_i(z) + 2x\left(\Gamma_i \frac{d^2\phi_i(z)}{dz^2} + \frac{d\phi_i(z)}{dz}\,\frac{1}{\phi_i(z)}\right)\right] \quad \text{(A4.10)}$$

Similarly, the first derivative of Equation (A4.9) with respect to y is shown below,

$$\frac{\partial\ddot{v}(x,y,z,t)}{\partial y} = \sum_{i=1}^{3} \ddot{D}_{\imath}(t)_y \left[1 + \Gamma_i\phi_i(z) + 2y\left(\Gamma_i \frac{d^2\phi_i(z)}{dz^2} + \frac{d\phi_i(z)}{dz}\,\frac{1}{\phi_i(z)}\right)\right] \quad \text{(A4.11)}$$

Next, the Jacobian matrix of the benchmark structure is formulated as follows,

$$J = \begin{pmatrix} \left[\frac{\partial\ddot{u}(x,y,z,t)}{\partial x}\right]_{1st\ floor} & \left[\frac{\partial\ddot{v}(x,y,z,t)}{\partial y}\right]_{1st\ floor} \\ \left[\frac{\partial\ddot{u}(x,y,z,t)}{\partial x}\right]_{2nd\ floor} & \left[\frac{\partial\ddot{v}(x,y,z,t)}{\partial y}\right]_{2nd\ floor} \\ \left[\frac{\partial\ddot{u}(x,y,z,t)}{\partial x}\right]_{3rd\ floor} & \left[\frac{\partial\ddot{v}(x,y,z,t)}{\partial y}\right]_{3rd\ floor} \\ \left[\frac{\partial\ddot{u}(x,y,z,t)}{\partial x}\right]_{4th\ floor} & \left[\frac{\partial\ddot{v}(x,y,z,t)}{\partial y}\right]_{4th\ floor} \end{pmatrix} \quad \text{(A4.8)}$$

where, $\phi_i(z) = \left(\cosh(\beta_i z) - \cos(\beta_i z)\right) - \frac{\cosh(3.6\beta_i)+\cos(3.6\beta_i)}{\sinh(3.6\beta_i)+\sin(3.6\beta_i)}\left(\sinh(\beta_i z) - \sin(\beta_i z)\right)$ (A4.9)

Recall Equation (4.22) and its numerical solutions,

$$1 + \cos(3.6\beta_i)\cosh(3.6\beta_i) = 0 \quad \text{(A4.7)}$$

where, $\beta_i \cong 0.521$, 1.304 and 2.182, are the numerical solutions for *i*= 1, 2, 3 respectively; $x = y \epsilon [0, 2.5]$ and $z \in \{0.9, 1.8, 2.7, 3.6\}$.

so,

$$\phi_1(z) = (-\sinh(0.521z) - \sin(0.521z)) - \frac{\cosh(1.875)+\cos(1.875)}{\sinh(1.875)+\sin(1.875)}(\cosh(0.521z) - \cos(0.521z))$$

$$\phi_2(z) = (-\sinh(1.304z) - \sin(1.304z)) - \frac{\cosh(4.694)+\cos((4.694))}{\sinh((4.694))+\sin((4.694))}(\cosh(1.304z) - \cos(1.304z))$$

$$\phi_3(z) = (-\sinh(2.182z) - \sin(2.182z)) - \frac{\cosh(7.855)+\cos((7.855))}{\sinh((7.855))+\sin((7.855))}(\cosh(2.182z) - \cos(2.182z))$$

## Appendix B

Some of MATLAB simulation codes utilized in this dissertation are given in Appendix B1. In addition, a description of the Matlab functions and R functions are summarized in Appendix B2 and Appendix B3, respectively.

### B1 MATLAB simulation codes

### Online Empirical Mode Decomposition （B1.1-B1.4）

The Matlab codes developed for online empirical mode decomposition are based on previous work of (Li, 2010), which may be obtained from http://www.penwatch.net/

### B1.1 Online EMD

```
classdef EMD
% EMD: Online empirical mode decomposition object.
% data_source = Buffer()
% emd = EMD ( data_source );
% forever:
%     data_source.Update (  get some new data );
%     emd.Update()
%     (calculated IMFs.)
% end loop

properties (GetAccess = public, SetAccess = private)
Data_Source = 0;
IMFs;
config;
end

methods.
% 'NumIMFs', 4 - extract exactly K IMFs.
% 'NewIMFTolerance', epsilon - set the threshold the last residue must
exceed to justify calculation of an additional IMF.
% force all IMF calculations to use exactly 10 sifting iterations.

function this = EMD ( data_source, config )
this.Data_Source = data_source;
% Establish array of IMF handles.
```

```
this.IMFs = IMF();

if (~exist('config','var') )
this.config = EMD_Default_Config();
else
this.config = [ config; containers.Map() ];
end

for n = 1:this.config('EMD:NUMBER_OF_IMFS')
if ( n == 1 ) h = this.Data_Source;
else h = this.IMFs(n-1);    end
this.IMFs(n) = IMF(h,n);
end
end

function condition = Update(this)
for n = 1:numel(this.IMFs)
this.IMFs(n).Update();
end
condition = 0;
end

% To extract part of one IMF.
data = Sliding_IMF ( this, IMF_number, n_start, n_end );
% To retrieve all IMF data in a cell array

function data = Get_Entire_Set_of_IMFs (this)
num_IMFs = numel(this.IMFs);
data = cell(num_IMFs,1);
for n = 1:num_IMFs
imf = this.IMFs(n);
if (imf.Latest == 0);
data{n} = []; % No data in that IMF yet.
else
data{n} = imf.GetMode(imf.Earliest,imf.Latest);
end
end
end

% To extract a sliding of an IMF's residue.
data = Sliding_Residue ( this, IMF_number, n_start, n_end );
Assess_New_IMF_P ( this );
end
end
```

### B1.2 Sliding Window

```
function data = Sliding_IMF (this, IMF_number, n_start, n_end)
imf = this.IMFs(IMF_number);
assert(IMF_number <= numel(this.IMFs),
, IMF_number, n_start, n_end);
assert( n_start >= imf.n_earliest, 'LwsEMD:OutOfBounds',...
['You requested data that has been pushed out of history.\n' ...
'details: IMF #%i, n_start = %i, n_end = %i\n'], IMF_number, n_start,
n_end);
assert( n_end <= imf.n_latest,
```

```
, IMF_number, n_start, n_end);
data = imf.GetMode(n_start, n_end);
end
```

### B1.3 Intrinsic Mode Functions

```
function t = IMF(data_source, IMF_number)
if ( nargin == 0 )
return
end

% Sanity checks and data source must be IMF or Buffer object
assert ( isa(data_source,'Buffer') || isa(data_source,'IMF'));

% Initialize properties.
t.source_max_v = [];
t.source_max_t = [];
t.source_min_v = [];
t.source_min_t = [];
t.data_source = data_source;
t.source_last_seen = 1;
t.n_earliest = 0;
t.n_latest = 0;

if (~exist('IMF_number'))
t.mode_num = 0;
else
t.mode_num = IMF_number;
end

if (~exist('config','var'));
t.config = EMD_Default_Config();
else
assert ( isa(copy,'containers.Map'));
t.config = [ config; containers.Map ];
end

assert( exist('extr.m') == 2);
end
%% Update function.
function Update(this)
UpdateExtrema(this);
Sift_Window(this);
this.source_last_seen = this.data_source.Latest;
end

function data_sliding = GetMode (this, n_start, n_end )
assert( this.Earliest <= n_start );
assert( this.Latest >= n_end );

array_index_start = n_start-this.n_earliest+1;
array_index_end = array_index_start + (n_end - n_start);
data_sliding = this.mode( array_index_start : array_index_end );
end
```

```
function data_sliding = GetResidue (this, n_start, n_end )
assert( this.Earliest <= n_start );
assert( this.Latest >= n_end );

array_index_start = n_start-this.Earliest+1;
array_index_end = array_index_start + (n_end - n_start);
data_sliding = this.residue( array_index_start : array_index_end );
end

function n = Earliest(this)
n = this.n_earliest; end
function n = Latest(this)
n = this.n_latest; end
function n = ModeNum(this)
n = this.mode_num; end
end
```

### B1.4 Hermite Spline

```
function v = hermite_spline(x,y,u)
% PCHIPTX stands for piecewise cubic Hermite interpolation.
%  v = hermite_spline (x,y,u) finds the Hermite piecewise cubic
%  interpolant P(x), with P(x(j)) = y(j), and returns v(k) = P(u(k)).
% The cool thing about Hermite interpolation is that it only uses local
% information to calculate the splines, which means that the splines
you've
% already calculated **don't change** when you add new data. (Except
for
% directly adjacent to the new data.)\

assert ( numel(x) == numel(y), 'Input vectors x and y must be same
length!');

h = diff(x);
delta = diff(y)./h;

if ( numel(x) == 0 )
error('Hermite_Spline(): warning - asked to interpolate zero points.
Meaningless!.');
return;
end
if ( numel(x) == 1 )
warning('Hermite_spline(): warning - interpolating one point?! Fitting
straight line.');
v = zeros(size(u)) + y(1)
return;
end

if ( numel(x) == 2 )
warning ('Hermite_spline(): Warning - interpolating between two points.
Fitting a linear model.');
v = interp1(x,y,u,'linear');
return;
end
```

```
assert( numel(x) > 2 );
d = pchipslopes(h,delta);

% Piecewise polynomial coefficients
n = length(x);
c = (3*delta - 2*d(1:n-1) - d(2:n))./h;
b = (d(1:n-1) - 2*delta + d(2:n))./h.^2;

% Find subinterval indices k so that x(k) <= u < x(k+1)
k = ones(size(u));
for j = 2:n-1
k(x(j) <= u) = j;
end

% Evaluate interpolant
s = u - x(k);
v = y(k) + s.*(d(k) + s.*(c(k) + s.*b(k)));

function d = pchipslopes(h,delta)
% PCHIPSLOPES  Slopes for shape-preserving Hermite cubic
% pchipslopes(h,delta) computes d(k) = P'(x(k)).

% Slopes at interior points
% delta = diff(y)./diff(x).
% d(k) = 0 if delta(k-1) and delta(k) have opposites
%          signs or either is zero.
% d(k) = weighted harmonic mean of delta(k-1) and delta(k) if they have
        the same sign.

n = length(h)+1;
d = zeros(size(h));

k = 2:n-1;
d(k) = ( delta(k-1) .* h(k) + delta(k) .* h(k-1) ) ./ ( h(k) + h(k-1)
);

% Slopes at endpoints
d(1) = pchipend(h(1),h(2),delta(1),delta(2));
d(n) = pchipend(h(n-1),h(n-2),delta(n-1),delta(n-2));
end

function d = pchipend(h1,h2,del1,del2)
%  Noncentered, shape-preserving, three-point formula.
d = ((2*h1+h2)*del1 - h1*del2)/(h1+h2);
if sign(d) ~= sign(del1)
d = 0;
elseif (sign(del1)~=sign(del2))&(abs(d)>abs(3*del1))
d = 3*del1;
end
```

### B1.5 Hilbert Huang transform

```
function imf= plot_hht(x,Ts)
% Plot the HHT.
% plot_hht(x,Ts)
% The array x is the input signal and Ts is the sampling period.
% Func : emd

% Obtain HHT.
imf = emd(x);
for k = 1:length(imf)
b(k) = sum(imf{k}.*imf{k});
th   = angle(hilbert(imf{k}));
d{k} = diff(th)/Ts/(2*pi);
end
[u,v] = sort(-b);
b     = 1-b/max(b);

% Time-frequency plots.
N = length(x);
c = linspace(0,(N-2)*Ts,N-1);
for k = v(1:2)
figure, plot(c,d{k});
end

% Set IMF plots.
M = length(imf);
N = length(x);
c = linspace(0,(N-1)*Ts,N);
for k1 = 0:4:M-1
figure
for k2 = 1:min(4,M-k1), subplot(4,1,k2), plot(c,imf{k1+k2});
set(gca,'FontSize',8,'XLim',[0 c(end)]); end
xlabel('Time');
end

figure
plot(c,imf{1}.^2)
```

### B1.6 Energy for each IMF

```
% Finding energy for each IMF
%input; Ts: sampling time, x1: undamge data, x2:damage data,
emd(x):imfs,
%{number of imf}, hi:hilbert transform, a: amplitude, E: energy
quantity
Ts=0.001;
x=load('x2.txt');
x1=x(1:40000);
x1=emd(x1);

x1=x1{5};
h1=hilbert(x1);
a1=(x1.^2+h1.^2).^0.5;
plot(abs(a1),'r')
E15=sum(abs(a1.^2))
```

### B1.7 Peaks for EMD

```
function imf = emd(x)
% Empiricial Mode Decomposition
% imf = emd(x)
% Func : findpeaks

x   = transpose(x(:));
imf = [];
while ~ismonotonic(x)
x1 = x;
sd = Inf;
while (sd > 0.1) | ~isimf(x1)
s1 = getspline(x1);
s2 = -getspline(-x1);
x2 = x1-(s1+s2)/2;

sd = sum((x1-x2).^2)/sum(x1.^2);
x1 = x2;
end

imf{end+1} = x1;
x          = x-x1;
end
imf{end+1} = x;

% FUNCTIONS
function u = ismonotonic(x)

u1 = length(findpeaks(x))*length(findpeaks(-x));
if u1 > 0, u = 0;
else,      u = 1; end

function u = isimf(x)

N  = length(x);
u1 = sum(x(1:N-1).*x(2:N) < 0);
u2 = length(findpeaks(x))+length(findpeaks(-x));
if abs(u1-u2) > 1, u = 0;
else,              u = 1; end

function s = getspline(x)

N = length(x);
p = findpeaks(x);
s = spline([0 p N+1],[0 x(p) 0],1:N);
```

### B1.8 Quasi-recursive Correlation Dimension

```
% The following function calculates the squared Euclidean distance
between embedding dimensions in a recursive way. (x: given signal; emb:
embedding dimension; tau: time delay)

function [cor_matrix_cell timearr]=cor_intit(x,emb,tau)
```

```
total_time=0;
tic
[cor_matrix]=cor_init(x,tau);
t=toc;
total_time=total_time+t;
timearr=total_time;
fprintf('Embedding Dimension %d done in %.2f seconds\n',2,t);
cor_matrix_cell=cell(emb-1,1);
cor_matrix_cell{1}=cor_matrix;
c=1;

for m=3:emb
tic
I=length(x)-(m-1)*tau-1;
J=length(x)-(m-1)*tau;
cor_matrix_new=zeros(I,J);
for i=1:I
for j=i+1:J
cor_matrix_new(i,j)=cor_matrix_cell{c}(i+tau,j+tau)+(x(i+tau)-
x(j+tau)).^2;
end
end

c=c+1;
cor_matrix_cell{c}=cor_matrix_new;
t=toc;
total_time=total_time+t;
timearr=[timearr total_time];
fprintf('Embedding Dimension %d done in %.2f seconds\n',m,t);
end
fprintf('Total time is %.2f seconds\n',total_time);
```

### B1.9 Overlapping Segmentation

```
%This function computes the squared Euclidean distance within each
embedding dimension using overlapping windowing method

function dist_cell=sliding_distanc(data,len,ov)
data=rand(100,1);%Raw time series
len=6;%size of the window
ov=4;%Overlapping segmentations

difference_ov=len-ov;%Sliding window
w=1+floor((length(data)-len)/difference_ov);
dist_cell=cell(w,1);

d_old=zeros(len-1,len);
xx=data(1:len);
for i=1:len-1
for j=i:len
d_old(i,j)=(xx(i)-xx(j)).^2;
end
end

dist_cell{1}=d_old;
```

```
for k=2:w
xx=data(difference_ov*(k-1)+1:difference_ov*(k-1)+len);
d_new=zeros(len-1,len);
d_new(1:ov-1,1:ov)=d_old(1+difference_ov:end,1+difference_ov:end);
for j=ov+1:len
for i=1:j-1
d_new(i,j)=(xx(i)-xx(j)).^2;
end
end
dist_cell{k}= d_new;
d_old=d_new;
end
```

### B1.10 Jacobian matrix

```
% The Jacobian matrix of the multistory structure vibration is the
first derivative of the acceleration with respect to each sensor
location

% height of the 1st, 2nd, 3rd and 4th floors, respectively
z=[.9 1.8 2.7 3.6]';

% Flexural rigidity in x and y directions for all four floors
EI=[1.99e4 1.9e4 1.88e4 1.96e4; 9.76e4 9.7e4 9.73e4 9.69e4];
% Circular frequency for each floor
W2=[11.79 32.01 48.03 60.15; 9.41 25.54 38.66 48.02];
% mass per unit length
ro=11;
gamma = [1.55 -.82 .5]';
lambda= [0.263 1 0.529]';
beta=[0.521 1.304 2.182]';
alpha=1.5;
EI0=0.04;
H=3.6;

om2=EI0*lambda.^2.*(lambda.^2+alpha^2)./ro/H.^4; % anguler frequency
Dl=-om2.*(cos(om2)+sin(om2));%relative accelration
% the closed form of the mode shape and its first and second
derivatives
count=1;
for i=1:4
phi(:,i)=(cosh(beta.*z(i))-cos(beta.*z(i)))-
(cosh(3.6*beta)+cos(3.6*beta)).*(sinh(beta.*z(i))-
sin(beta.*z(i)))./(sinh(3.6*beta)+sin(3.6*beta));
end

for i=1:4
phi1(:,i)=(beta.*sinh(beta.*z(i))+beta.*sin(beta.*z(i)))-
(cosh(3.6*beta)+cos(3.6*beta)).*(beta.*cosh(beta.*z(i))-
beta.*cos(beta.*z(i)))./(sinh(3.6*beta)+sin(3.6*beta));
end

for i=1:4
```

```
phi2(:,i)=(beta.^2.*cosh(beta.*z(i))+beta.^2.*cos(beta.*z(i)))-
(cosh(3.6*beta)+cos(3.6*beta)).*(beta.^2.*sinh(beta.*z(i))+beta.^2.*sin
(beta.*z(i)))./(sinh(3.6*beta)+sin(3.6*beta));
end

% Generate x and y arrays for two dimensional Cartesian space
[XX YY] = meshgrid(0:0.1:2.5,0:0.1:2.5);
x=XX(:);
y=YY(:);
jac=zeros(8,length(x));

% calculation of the Jacobian matrix
for i=1:length(x)
jac(1,i)=sum(Dl.*(1+gamma.*phi(:,1)+2*x(i)*(gamma.*phi2(:,1)+phi1(:,1).
/phi(:,1))));
jac(2,i)=sum(Dl.*(1+gamma.*phi(:,2)+2*x(i)*(gamma.*phi2(:,2)+phi1(:,2).
/phi(:,2))));
jac(3,i)=sum(Dl.*(1+gamma.*phi(:,3)+2*x(i)*(gamma.*phi2(:,3)+phi1(:,3).
/phi(:,3))));
jac(4,i)=sum(Dl.*(1+gamma.*phi(:,4)+2*x(i)*(gamma.*phi2(:,4)+phi1(:,4).
/phi(:,4))));
jac(5,i)=0.18*sum(Dl.*(1+gamma.*phi(:,1)+2*y(i)*(gamma.*phi2(:,1)+phi1(
:,1)./phi(:,1))));
jac(6,i)=0.18*sum(Dl.*(1+gamma.*phi(:,2)+2*y(i)*(gamma.*phi2(:,2)+phi1(
:,2)./phi(:,2))));
jac(7,i)=0.18*sum(Dl.*(1+gamma.*phi(:,3)+2*y(i)*(gamma.*phi2(:,3)+phi1(
:,3)./phi(:,3))));
jac(8,i)=0.18*sum(Dl.*(1+gamma.*phi(:,4)+2*y(i)*(gamma.*phi2(:,4)+phi1(
:,4)./phi(:,4))));
end

save jacobian.txt jac -ascii
```

### B1.11 Objective function

```
%The so called Figure of Merit (FOM) is considered as an objective
function
function FOM=obj_fun(jac,init_perm)
l=length(init_perm);
fisher=jac(:,init_perm)'*jac(:,init_perm); % The Fisher information
matrix
[U,S,V] = svd(fisher);                    % The Singular Value
Decomposition

% Generate x and y arrays for two dimensional Cartesian space
[XX YY] = meshgrid(0:0.1:2.5,0:0.1:2.5);
y=XX(:);
z=YY(:);
d=0;

% impose constraint on the distance between any two sensor locations in
each floor
for i=1:2:8
d=d+norm([y(init_perm(i)) z(init_perm(i))]-[y(init_perm(i+1))
z(init_perm(i+1))]);
end
```

```
% FOM as a combination of the condition number, trace and determinant
of the Fisher information matrix
FOM=-cond(S)+trace(S)+det(S)+1e18;
```

### B1.12 Simulated Annealing Algorithm

```
%loading the Jacobian matrix, which is the first-order derivative of
the representative ordinary differential equation with respect to each
sensor location

jac=load('jacobian.txt');
T=200;                            %initial temperature
alpha=0.98;                       %cooling rate
max_iter=1000;                    %maximum number of iteration
number_of_nodes=8;

% a random initial placement, calculate the initial score, perturb the
placement between nodes and calculate the change in score due to the
move made
dist_arr=zeros(max_iter,1);
perm_rand=randperm(length(jac));
init_perm=perm_rand(1:number_of_nodes);
left_perm=perm_rand(number_of_nodes+1:end);
init_FOM=obj_fun(jac,init_perm);
old_perm=init_perm;
old_FOM=init_FOM;
new_perm=init_perm;

% Update the temperature value by lowering the temperature and perturb
the placement between nodes
for i=1:max_iter
u=ceil(number_of_nodes*rand);
v=ceil((length(jac)-number_of_nodes)*rand);
new_perm=old_perm;
temp = old_perm(u);
new_perm(u)=left_perm(v);
new_FOM=obj_fun(jac,new_perm);

% Depending on the change in score, accept or reject the move. The prob
of acceptance depending on the current “temperature”.
if new_FOM>old_FOM
old_perm=new_perm;
old_FOM=new_FOM;
left_perm(v)=temp;
else
p=exp((new_FOM-old_FOM)/T);
if p>0.5
old_perm=new_perm;
old_FOM=new_FOM;
left_perm(v)=temp;
end
end
T=alpha*T;
dist_arr(i)=old_FOM;
end
```

```
% plot(dist_arr)
fprintf('Sensor Configuration Nodes\n');
fprintf('%d\t',old_perm)
fprintf('\n');

% Generate x and y arrays for two dimensional Cartesian space
[XX YY] = meshgrid(0:0.1:2.5,0:0.1:2.5);
y=XX(:);
z=YY(:);
cc=1;
figure

%output display
for i=1:4
subplot(2,2,i)
title([num2str(i) '. floor'])
xlim([-0.5 3]);ylim([-0.5 3]);
hold on
for j=1:length(XX);
plot(XX(:,j),YY(:,j))
plot(XX(j,:),YY(j,:))
end
plot(y(old_perm(cc)),z(old_perm(cc)),'.r','MarkerSize',18);
cc=cc+1;
plot(y(old_perm(cc)),z(old_perm(cc)),'.r','MarkerSize',18);
cc=cc+1;
end

fprintf('Sensor Coordinates\n');
fprintf('x-coordinate y-coordinate\n')
fprintf('------------ ------------\n')
fprintf('\t%.2f\t\t %.2f\n',[y(old_perm) z(old_perm)])
fprintf('\n');

fprintf('FOM is %3.2e\n',old_FOM);
coordinates= [y(old_perm) z(old_perm)];
```

## B2 Description of Matlab functions

The Matlab functions, which are described below, can be downloaded from the link

http://eeganalysis.web.auth.gr/

### B2.1 Correlation Sum

#### Description

This function calculates the Correlation Sum for a given time series. The parameter 'theiler' excludes temporally close points from the inter-distance computations.

#### Usage

```
function corsumT = CorrelationSum(xV,rV,tauV,mV,theiler)
```

**Input**

```
 - xV      : Vector of the scalar time series
 - rV      : A vector of the radius (assuming first that 'xV' is
             standardized in [0,1]).
 - tauV    : A vector of the delay times.
 - mV      : A vector of the embedding dimension.
 - theiler : the Theiler window to exclude time correlated points in
             the search for neighboring points. Default=0.
```

**Output**

```
corsumT    : A matrix of size 'nr' x 'ntau' x 'nm', where 'nr' is the
            number of given radius, 'ntau' is the number of given
            delays and 'nm' is the number of given embedding
            dimensions. The components of the matrix are the
            correlation sum values.
```

### B2.2 Correlation Dimension

**Description**

This function computes the Correlation Dimension on a given time series.

**Usage**

```
function nuT = CorrelationDimension(xV,tauV,mV,theiler,sV,resol)
```

**Input**

```
 -  xV     : Vector of the scalar time series
 - tauV    : A vector of the delay times.
 - mV      : A vector of the embedding dimension.
 - theiler : the Theiler window to exclude time correlated points in
             the search for neighboring points. Default=0.
 - sV      : A vector of values of upper/lower ratio of scaling window
            (e=r2/r1 where r2-r1 is the length of the scaling window).
 - resol   : The number of radius for which the correlation sum is
             computed.
```

**Output**

```
- nuT      : A matrix of size 'ntau' x 'nm' x 'ne', where 'ntau' is the
             number of given delays, 'nm' is the number of given
             embedding dimensions and 'ne' is the number of scaling
             ratio of radii. The components of the matrix are the
             correlation dimension values.
```

### B2.3 False Nearest Neighbors

**Description**

This function computes the percentage of false nearest neighbors for a range of delays and embedding dimensions.

**Usage**

```
function fnnM = FalseNearestNeighbors(xV,tauV,mV,escape,theiler)
```

**Input**

```
-  xV       : Vector of the scalar time series
-  tauV     : A vector of the delay times.
-  mV       : A vector of the embedding dimension.
-  escape   : A factor of escaping from the neighborhood. Default=10.
-  theiler  : the Theiler window to exclude time correlated points
```

**Output**

```
-  fnnM     : A matrix of size 'ntau' x 'nm', where 'ntau' is the
              number of given delays and 'nm' is the number of given
              embedding dimensions, containing the percentage of false
              nearest neighbors.
```

### B2.4 Mutual Information

**Description**

This function computes the mutual information lag of the first local minimum of mutual information using a sliding window of length 2*nsam+1.

**Usage**

```
function minmuttau = findminMutInf(,nsam)
```

**Input**

```
-    miV      : minimum of mutual  information
-    nsam     : a sliding window of length 2*nsam+1
```

**Output**

```
-  Minmuttau  : the lag tau of the first local minimum of mutual
                Information
```

### B2.5 Piecewise Cubic Hermite Interpolating Polynomial

**Description**

This function computes the piecewise cubic interpolation within vectors x and y

**Usage**

```
function v = pchip(x,y)
```

**Input**

```
-  x      : a vector that specifies the points at which the data is
            given
-  y      : a given data
```

**Output**

```
 -  v       : piecewise cubic interpolation within vectors x and y
```

### B3 Description of R functions

The R functions, which are described in this appendix, can be downloaded from the "EMD" package, version 1.2.0 and website at http://cran.r project.org/web/packages/EMD/index.html.

#### B3.1 Empirical Mode Decomposition

**Description**

This function calculates the empirical mode decomposition

**Usage**

```
   emd(xt, tt=NULL, tol=sd(xt)*0.1^2, max.sift=20, stoprule="type1",
boundary="periodic", sm="none", max.imf=10, plot.imf=FALSE,
interm=NULL)
```

**Input**

```
 -  xt         : signal observed at time tt
 -  tt         : time index
 -  tol        : tolerance for stopping rule of sifting.
 -  max.sift   : the maximum number of sifting.
 -  stoprule   : stopping rule of sifting.
 -  Boundary   : specifies boundary condition from "none", "wave",
                "symmetric", "periodic" or "evenodd".
 -  sm         : specifies whether envelop is constructed by
                 interpolation, spline smoothing, kernel smoothing,
                 or local polynomial smoothing
 -  max.imf    : the maximum number of IMF's
 -  interm     : specifies vector of periods to be excluded from the
                 IMF's to cope with mode mixing.
```

**Output**

```
 -  imf        : Intrinsic Mode Functions
 -  residue    : residue signal after extracting IMF's from observations
                 xt
 -  nimf       : the number of IMF's
```

#### B3.2 Prediction by EMD

**Description**

This function calculates prediction values and confidence limits using EMD

**Usage**

```
   emd.pred(varpred, trendpred, ci = 0.95, figure = TRUE)
```

### Input

- varpred   : prediction result of IMF’s by VAR model.
- trendpred : prediction result of residue by polynomial regression model.
- ci        : confidence interval level

### Output

- fcst      : prediction values
- lower     : lower limits of prediction
- upper     : upper limits of prediction
-

## B3.3 Intrinsic Mode Function

### Description

This function extracts intrinsic mode functions from a given signal

### Usage

```
   extractimf(residue, tt=NULL, tol=sd(residue)*0.1^2, max.sift=20,
stoprule="type1", boundary="periodic", sm="none", spar=NULL,
alpha=NULL, check=FALSE)
```

### Input

- residue   : signal observed at time tt
- tt        : time index
- tol       : tolerance for stopping rule of sifting.
- max.sift  : the maximum number of sifting.
- stoprule  : stopping rule of sifting.
- Boundary  : specifies boundary condition from “none", “wave", “symmetric", “periodic" or “evenodd".
- sm        : specifies whether envelop is constructed by interpolation, spline smoothing, kernel smoothing, or local polynomial smoothing
- spar      : specifies user-supplied smoothing parameter of spline smoothing, kernel smoothing, or local polynomial smoothing.
- alpha     : deprecated.
- check     : specifies whether the sifting process is displayed.
- weight    : deprecated

.

### Output

- imf       : Intrinsic Mode Functions
- residue   : residue signal after extracting IMF’s from residue
- niter     : the number of iteration to obtain the IMF’s

## B3.4 Local Extrema and zero-crossing

### Description

This function calculates extrema and zero-crossing

### Usage

```
extrema(y, ndata = length(y), ndatam1 = ndata - 1)
```

### Input

- `y` : input signal.
- `ndata` : the number of observation.
- `ndatam1` : the number of observation -1

### Output

- `minindex` : matrix of time index at which local minima are attained. Each row specifies a starting and ending time index of a local minimum
- `maxindex` : matrix of time index at which local maxima are attained. Each row specifies a starting and ending time index of a local maximum.
- `nextreme` : the number of extrema
- `cross` : matrix of time index of zero-crossings. Each row specifies a starting and ending time index of zero-crossings.
- `ncross` : the number of zero-crossings

## B3.5 Hibert Transform and Instantaneous frequency

### Description

This function calculates the amplitude and instantaneous frequency using Hilbert transform

### Usage

```
hilbertspec(xt, tt=NULL, central=FALSE)
```

### Input

- `xt` : matrix of multiple signals. Each column represents a signal.
- `tt` : observation index or time index
- `central` : If central=TRUE, use central difference method to calculate the instantaneous frequency

### Output

- `amplitude` : matrix of amplitudes for multiple signals xt
- `instantfreq` : matrix of instantaneous frequencies for multiple signals xt
- `energy` : cumulative energy of multiple signals

# VITA

Mahmoud Zeidan Mistarihi

Candidate for the Degree of

Doctor of Philosophy

Dissertation: **SENSOR-BASED NONLINEAR AND NONSTATIONARY DYNAIMC ANALYSIS OF ONLINE STRUCTURAL HEALTH MONITORING**

Major Field: Industrial Engineering and Management

Biographical:

Education:
Received Bachelor of Science degree in Mathematics from Mutah University in Al-Karak, Jordan, in June 1995; received Master of Science degree with a pure Topology major in Mathematic at Mutah University in Al-Karak, Jordan, in June 2003; completed Doctor of Philosophy degree with a major in Industrial Engineering and Management at Oklahoma State University in December, 2013.

Experience:
Employed by Oklahoma State University, Department of Mathematics as a teaching assistant, from August 2008 to May 2009 and at School of Industrial Engineering and Management as a graduate research assistant and teaching assistant, from August 2010 to May 2013. Worked for the Oklahoma State University as Assistant Resident Director from 2012-2013.

Professional Memberships:
- Institute for Industrial Engineering (IIE)
- American Society of Quality (ASQ)